Reaction Volumes of Photoinitiated Reactions, and Their Use As Probes of Reactive Intermediates

by

Kevin William Davies

BS, University of Pittsburgh, 2002

Submitted to the Graduate Faculty of

Arts and Sciences in partial fulfillment

of the requirements for the degree of

Doctor of Philosophy

University of Pittsburgh

2008

UNIVERSITY OF PITTSBURGH

Faculty of Arts and Sciences

This dissertation was presented

by

Kevin William Davies

It was defended on

August 22nd, 2008

and approved by

Geoffrey Hutchison, Assistant Professor, Department of Chemistry

Peter E. Siska, Professor, Department of Chemistry

Mitchell E. Johnson, Associate Professor, Department of Chemistry and Biochemistry, Duquesne University

Dissertation Advisor: Joseph J. Grabowski, Associate Professor, Department of Chemistry

Copyright © by Kevin W. Davies

2008

Reaction Volumes of Photoinitiated Reactions, and Their Use As Probes of Reactive Intermediates

Kevin William Davies, PhD

University of Pittsburgh, 2008

Photoacoustic calorimetry is a sensitive method for measuring the enthalpies, kinetics, and changes in volumes for reactions that generate transient intermediates through photoexcitation.

This work focuses on building a better understanding of ΔV_{rxn}, to ascertain the importance of accounting for ΔV_{rxn} when measuring enthalpies of reaction via photoacoustic methods. ΔV_{rxn} for three metal carbonyls has been measured. The results presented herein show that to obtain high-quality thermochemical information from photoacoustic measurements, it is necessary to account for the contribution of ΔV_{rxn}. Neither the magnitude nor the sign of this contribution may be predicted without either the direct measurement of ΔV_{rxn} or (as an outcome of the research described in this dissertation) computationally. Failure to account for this contribution may results in errors in the measured ΔH_{rxn} by as much as 79% [*e.g.* $(CH_3OC)Mn(CO)_5$ in octane].

This dissertation also lays the groundwork for the use of ΔV_{rxn} to distinguish between possible structures of short-lived intermediates though a combination of photoacoustic measurements and computational chemistry. A protocol is described that will allow molecular dynamics simulations to be used to determine the solvated volume of a molecule, and to combine several of these measurements to allow the volume change accompanying a reaction to be determined computationally. Simulations conducted via this protocol are in good agreement

with our experimental results. These simulations will allow experimental results to provide a new window into the nature of short-lived intermediates, and the mechanistic of their reactions. Several unsuccessful molecular dynamics simulations are also described in order to identify cases where simulations may not provide accurate data and how these issues may be addressed.

TABLE OF CONTENTS

PREFACE ..... **XIV**

1.0 INTRODUCTION **1**

1.1 GENERAL BACKGROUND ON PHOTOACOUSTIC CALORIMETRY .. **1**

1.2 GOALS AND SCOPE **3**

2.0 THEORY AND INSTRUMENTATION **5**

2.1 THE THEORY OF PHOTOACOUSTIC CALORIMETRY **5**

2.1.1 The Fundamental Photoacoustic Equation **5**

2.1.2 Separating the Enthalpic and Volumetric Contributions to the Photoacoustic Signal **10**

2.2 THE PHOTOACOUSTIC CALORIMETER **13**

2.2.1 Light Source **15**

2.2.2 Light Path **15**

2.2.3 Signal Collection **18**

2.3 ACTINOMETRIC MEASUREMENTS **20**

2.3.1 Experimental Setup **20**

2.3.2 Photoacoustic Actinometry Data Analysis **22**

3.0 CHARACTERIZATION OF THE REACTION ENTHALPY AND VOLUME FOR THE PREPARATION OF A REACTIVE INTERMEDIATE FROM CYMANTRENE 24

3.1 ABSTRACT 24

3.2 INTRODUCTION 25

3.3 EXPERIMENTAL 29

3.3.1 General 29

3.3.2 Photoacoustic Calorimetry 29

3.3.3 Quantum Yield Determination 32

3.4 THEORY 34

3.5 RESULTS AND DISCUSSION 37

3.5.1 Quantum Yield 37

3.5.2 Photoacoustic Calorimetry 38

3.6 ACKNOWLEDGMENTS 43

4.0 A PHOTOACOUSTIC CALORIMETRY STUDY OF CHROMIUM HEXACARBONYL: COMPARISON OF THE TWO METHODS OF PHOTOACOUSTICALLY DETERMINING THE REACTION VOLUME 44

4.1 ABSTRACT 44

4.2 INTRODUCTION 45

4.3 EXPERIMENTAL 48

4.4 RESULTS 52

4.5 DISCUSSION 56

4.5.1 Quantum Yield 56

4.5.2 Photoacoustic Calorimetry 58

4.5.3 Comparison of Linear Alkane and High-pressure PAC 60

4.5.4 The Cr-alkane Agostic Bond 62

4.6 CONCLUSION 63

5.0 THE PHOTOACOUSTIC MEASUREMENT OF THE INTERMEDIATE OF THE MIGRATORY INSERTION REACTION 64

5.1 INTRODUCTION 64

5.2 EXPERIMENTAL 67

5.2.1 Synthesis of $(CH_3OC)Mn(CO)_5$ 67

5.2.2 Photoacoustic Calorimetry 70

5.3 RESULTS 70

5.4 DISCUSSION 74

5.4.1 The Reaction Enthalpy 74

5.4.2 The Volume Change of the Reaction 76

5.4.3 Identifying the Structure of the Intermediate from the Volume Change of the Reaction 77

5.5 CONCLUSION 78

6.0 PREDICTION OF THE VOLUME OF REACTION FOR ORGANIC MOLECULES VIA MOLECULAR DYNAMICS SIMULATIONS 80

6.1 INTRODUCTION 80

6.2 EXPERIMENTAL 82

6.2.1 Overview of Molecular Dynamics Simulations 82

6.2.2 Initial Structures and Charge Assignment 83

6.2.3 Molecular Dynamics Simulations 84

6.3 RESULTS AND DISCUSSION 88

6.3.1 Initial Simulations 88

6.3.2 MD Production Simulations 92

6.4 CONCLUSION 96

APPENDIX A 97

APPENDIX B 119

APPENDIX C 138

APPENDIX D 142

BIBLIOGRAPHY 150

LIST OF TABLES

Table 3-1 Solvent Parameters and f_h^{obs} for $CpMn(CO)_3$ at 25°C 40

Table 4-1 Solvent Parameters and f_h^{obs} for $Cr(CO)_6$ at 25°C 55

Table 4-2 Comparison of PAC measurements of ΔH_{rxn} and ΔV_{rxn} at both ambient and high-pressures. The value measured by Farrell and Burkey has been estimated from their published plots.[77] 61

Table 4-3 Examples of Agostic Interactions 62

Table 5-1 Solvent Parameters and f_h^{obs} for $(CH_3OC)Mn(CO)_5$ at 25°C 73

Table 5-2 Magnitude of errors caused by failing to account for ΔV_{rxn} when measuring ΔH_{rxn} ... 77

Table 6-1 Results for the initial molecular dynamics simulations of azobenzene/water 89

Table 6-2 Results for the initial molecular dynamics simulations of DPCP/water 89

Table 6-3 Summary of MD Production Runs 92

LIST OF FIGURES

Figure 2-1 General Jablonski diagram for possible outcomes of the photoexcitation of an analyte. Thermal relaxations are highlighted by red (curvy) arrows. 6

Figure 2-2 An example of PAC signals. Inset: PAC signals plotted according to Equation 2-3, allowing accurate determination of κ and f_h 9

Figure 2-3 Representative plot showing the determination of f_h (slope) and ΔV_{chem} (intercept) from f_h^{obs} measured in various linear alkanes, using Equation 2-7 12

Figure 2-4 Layout of the photoacoustic calorimeter used in this work 14

Figure 2-5 The photoacoustic cell and photoacoustic transducer (drawings not to scale) 17

Figure 2-6 Modified photoacoustic calorimeter for actinometric measurements. 21

Figure 3-1 Jablonski diagram for the photoprocesses relevant to the PAC measurement of $CpMn(CO)_3$. As the lifetime of $CpMn(CO)_2$ (alkane) is on the order of seconds in the absence of nucleophiles,[38] its decay pathways are too slow to impact the PAC measurement [39] 27

Figure 3-2 Averaged waves (30 shots) from a typical PAC experiment at a single laser energy. Inset: PAC signals for $CpMn(CO)_3$ and two standards plotted according to Equation 3-3 31

Figure 3-3 Plot of $f_h^{obs} h\nu X_s$ versus X_s (Equation 3-6) for the photoinitiated reaction of $CpMn(CO)_3$ in linear alkanes 36

Figure 4-1 Jablonski diagram for the photoprocesses relevant to the PAC measurement of $Cr(CO)_6$. 48

Figure 4-2 PAC signals for two $Cr(CO)_6$ measurements and two standards plotted according to Eq. 4-2. Shown are two waves from standards, two from $Cr(CO)_6$, and one from pure solvent. The small negative spike observed at 3 μs corresponds to the firing of the laser. Data before this point serves as the baseline for wave integration. Integration limits used are shown by dashed lines. Inset: Averaged waves (50 laser shots) from a typical PAC experiment at a single laser energy (E_p). 54

Figure 4-3 Plot of 1 / (1 - Φ_{diss}) versus $1/\eta$ [88, 89] for $Cr(CO)_6$ (♦) [87, 90] and di-*tert*-butyl peroxide (■) [94, 95]. Inset: Viscosities and quantum yields of $Cr(CO)_6$. 57

Figure 4-4 Plot of $[(1-f_h^{obs})h\nu X_s]/\Phi_{diss}$ versus X_s (Equation 4-8) for the photoinduced reaction of $Cr(CO)_6$ in linear alkanes. 59

Figure 5-1 Mass spectrum of $(CH_3OC)Mn(CO)_5$ 69

Figure 5-2 Averaged waves (30 shots) from a typical $(CH_3OC)Mn(CO)_5$ experiment at a single energy. Inset: PAC signals for $(CH_3OC)Mn(CO)_5$ and two standards plotted according to Equation 2-5 72

Figure 5-3 f_h^{obs} data for $(CH_3OC)Mn(CO)_5$, $CpMn(CO)_3$, $Cr(CO)_6$, and standards in linear alkanes, plotted according to Equation 2-7. The data points for $Cr(CO)_6$ have been corrected to account for the differences in Φ_{diss}. 75

Figure 6-1 Typical plots of *s* from Equation 6-6, used to determine the number of samples between statistically uncorrelated points. In this example, the left plot predicts that 35 samples could be taken between uncorrelated points, while the plot on the right predicts 43; in this example, 40 samples (i.e. 4.0 ns) was chosen as our simulation sampling time. 87

Figure 6-2 Volume vs. time plot for the azobenzene MD production run. The overlaid horizontal lines represent the average volume. Inset: detail view of part of the time coordinate. 93

Figure 6-3 Volume vs. time plot for the DPCP MD production run. The overlaid horizontal lines represent the average volume. Inset: detail view of part of the time coordinate..... 94

PREFACE

Science is fun, but the accompanying lifestyle can be demanding. I have been blessed with an excellent scientific and personal support network during my Ph.D. work, and am excited to have an opportunity to thank them here.

My advisor, Dr. Joseph J. Grabowski, has given me many opportunities to grow both inside the laboratory and beyond it. Dr. Grabowski's research group has been wonderful mix of friends and colleagues to me; in particular I would like to acknowledge Drs. Christopher Taormina and Mark Morris for always taking the time to let me bounce half-formed ideas off of them. All of these people have improved my science in immeasurable ways.

There are so many people I would like to thank in the Chemistry Department that my dissertation risks becoming a volume set; I will settle for a radically truncated list, and hope my unnamed friends will show the same tolerance as they have in the past. I would like to express my gratitude to Drs. Paul Rasmussen (currently at the Petroleum Institute in Abu Dhabi), Ken Jordan, Richard Christie, Adrian Michael, George Bandik, as well as Erikah Englund, Zeeshan Ahmed, Katherine Stone, Sruti Bhaumik, and Jessica Sarver.

Outside of the Chemistry department, I would like to thank Dr. Jen Cartier and Wendy Sink (Univ. of Pitt. School of Ed.) and everyone else who participated in our NSF GK-12 fellowship.

All of these people have helped me develop my research, hone my teaching, or polish my thinking, as well as being a joy to work alongside. However, there are a few people who have done all this and far, far more: my family. I would like to thank my parents, Katherine and William Davies, for raising me to persevere and think about how the world works; and to my brothers, Jason and Joseph Davies, for their constant support. My final acknowledgement has been reserved for my wife, Gabriela Molina. Each day that I have worked on this dissertation, I have tried to list the ways she has helped me and every time I have failed. Instead, let me say simply that she inspires me to do more and be better in every area of my life.

LIST OF SYMBOLS

A	absorbance
C_p	molar heat capacity of the solvent
$E_{absorbed}$	energy absorbed by a solution
E_{exc}	excitation energy
E_p	laser pulse energy
f_h	fraction of absorbed energy converted to heat
h	Planck's constant
ΔH_{rxn}	enthalpy of reaction
MW	molecular weight (used here in reference to the solvent)
n_b	the number of output measurements from a molecular dynamics simulation in a specified block of time
Q	heat deposited to the solvent
S_{obs}	observed signal
S_{therma}	portion of the photoacoustic signal attributable to heat deposition
S_{volume}	portion of the photoacoustic signal attributable to the difference between the solvated volumes of the reactants and products
$\overline{V}_b$	average volume in a block of data from a molecular dynamics simulation

ΔV_{chem}	volume change associated with the chemical reaction (not normalized by the quantum yield)
$\overline{V}_{run}$	average volume for an entire molecular dynamics simulation
ΔV_{rxn}	volume change associated with the chemical reaction (normalized by the quantum yield)
α	thermal expansion coefficient of the solvent
X_s	solvent expansivity; $= \alpha\, MW / C_p\, \rho$
$\Phi_{process}$	quantum yield for a given process; the fraction of molecules relax along a particular pathway
κ	experimental coefficient, accounts for various aspects of signal detection and experimental conditions (*e.g.* solvent expansivity, cell geometry, cell-to-transducer coupling)
κ'	instrumental response constant; identical to κ except that X_s has been factored out
ν	photon frequency
ρ	density (used here in reference to the solvent)
σ^2	variance
τ	lifetime of an excited state with respect to a particular process; the same excited state may have a different lifetime if a relaxation process is 'turned on or off'
τ_b	the temporal length of a specified block of data from a molecular dynamics simulation
τ_{run}	the total modeled time in a molecular dynamics simulation

1.0 INTRODUCTION

1.1 GENERAL BACKGROUND ON PHOTOACOUSTIC CALORIMETRY

During the last three decades, photoacoustic calorimetry (PAC, also known as laser-induced optoacoustic calorimetry, LIOAC) has become a useful tool for the study of photoinitiated reactions. In PAC, an analyte solution is irradiated with a pulsed monochromatic light source. An analyte molecule absorbs a photon and is photoexcited. This excited state may then partition the absorbed energy among various pathways, such as photofragmentation, internal conversion, fluorescence, phosphorescence, and intersystem crossings. Each of these pathways will result in some (or all) of the energy being deposited to the surrounding solvent molecules as heat. This local temperature change in turn results in a local volume expansion, which propagates through the solvent as an acoustic wave. This acoustic wave is detected by a piezoelectric transducer and recorded for further analysis, which can allow the simultaneous determination of both the energetics and kinetics of the reaction.

The lifetime of the excited state dictates how (and if) a process may be measured photoacoustically. Processes resulting in heat release with lifetimes slower than 10^{-5} seconds cannot be detected by our transducer ('too-slow' domain). All processes with lifetimes less than 10 ns cannot be resolved from each other by our detector, and appear as a single photoacoustic waveform ('too-fast' domain). Processes with lifetimes between 10^{-8} and 10^{-5} seconds give

photoacoustic waveforms which are phase-shifted to later times (time-resolved domain). If all processes fall either in the 'too-fast' or 'too-slow' time domains, no further kinetic information my be derived from the photoacoustic wave, and a simplified data analysis method is available (called time-independent PAC) to determine the reaction enthalpy. If one or more processes fall within the time-resolved domain, these simultaneous contributions to the photoacoustic wave can be disentangled, recovering the enthalpies and kinetics of each process in this window.

Generally, PAC requires knowledge of the balanced reaction for each process in order to allow assignment of measured enthalpies. In particular, knowledge of the quantum yield for each heat-deposition pathway is necessary to fully interpret the raw PAC data. These quantum yields must be of high quality to ensure the best analysis of the photoacoustic data; most of the error in the determined enthalpies, reaction volumes, and bond-dissociation energies derive from the quantum yield rather than the PAC results.[1]

PAC has been used to determine the reaction enthalpies of photoinduced processes,[2-8] the heats of formation of reactive intermediates,[9-11] quantum yields,[12] and the kinetics and lifetimes of transient intermediates [13-16] (citations are representative, not exhaustive).

In many PAC studies that are performed in organic solvents, the entire photoacoustic signal has been assigned to the thermal relaxation of the photoexcited species, based on the assumption that the volume change would be miniscule. This assumption is undoubtedly accurate for systems which do not undergo any net photochemistry, but could be erroneous for molecules that undergo photofragmentation. That is, the assumption often employed may be in error when there is a difference between the partial molar volume of the reactants and products ($\Delta V_{rxn} \neq 0$), and this difference is a significant fraction of the observed volume expansion. To date, few examples of the ΔV_{rxn}'s contribution to photoacoustic signals have been documented

for systems in organic solvents. For aqueous systems, where the solvent expansivity is often a factor of ten or more smaller than for organic solvents, consideration of non-thermal contributions to the photoacoustic signal typically are treated explicitly.[11, 17-20] To separate the contribution of the volumetric and enthalpic changes to the photoacoustic signal, solvent expansivity can be varied by changing the temperature (if the solvent has a significant expansivity dependence on temperature as is the case for water),[11] pressure,[21] or using a homologous series of solvents that do not measurably affect the energetics of the system.[22] This last method, which utilizes linear alkanes as its solvent series (in which relative solvation effects are constant, but for which the solvent expansivity varies)[23] is considerably easier to conduct experimentally than the high-pressure approach.[21]

PAC is a particularly useful technique for analyzing reactive intermediates, as it yields energetic data for any heat releasing pathway along a reaction coordinate (provided it meets the detector's kinetic requirements); analysis of transient intermediates is often a challenge for spectroscopic techniques due in part to the low concentrations of the transient. Compared to transient absorption techniques, PAC requires a low photon flux (μJ instead of mJ), minimizing the likelihood of multiphoton events and photobleaching, and may routinely detect the low typically low concentration of the transient intermediates.

1.2 GOALS AND SCOPE

This dissertation includes an examination of $CpMn(CO)_3$ (Cp = cyclopentadiene), $Cr(CO)_6$, and $(CH_3OC)Mn(CO)_5$. These metal carbonyls were chosen due to their utility in understanding the role of coordinatively unsaturated metal complex intermediates, and due to their well-

characterized photochemistry. Additionally, $Cr(CO)_6$ has previously been studied by high-pressure PAC, allowing direct comparison of these two techniques.

To date, though the physical significance of ΔV_{rxn} has been well-understood, is has been treated merely as a correction to the measurement of reaction enthalpies, rather than used in an analytic fashion. It is hoped that by gaining a better knowledge of ΔV_{rxn} for a variety of systems we will be able to use this term to distinguish between possible structures for an otherwise indeterminate reactive intermediate. One example of such an ambiguous structure is the transient intermediate in the much-studied migratory insertion reaction $Mn(CO)_5CH_3 \rightarrow Mn(CO)_5(COCH_3)$. The synthesis and photoacoustic analysis of $(CH_3OC)Mn(CO)_5$ is presented here, as are molecular dynamics experiments which will lay the framework for analyzing the intermediate of this migratory insertion reaction.

Though the thermochemistry and kinetics of a reaction can provide insight into the reaction mechanism, understanding the relationship between structures (and how they change) and physical and chemical properties often provides far deeper insights. To this end, molecular dynamics simulations have been developed that, when accompanied by experimental results, will provide a window into how the molecule's structure is related to the volume of solvent that it excludes. This will provide structural insight into molecules in a much shorter time window than previously possible.

2.0 THEORY AND INSTRUMENTATION

This chapter serves as a general introduction as to how a photoacoustic signal is generated, collected, and interpreted. Subsequent chapters include more specific information about the particular experimental conditions used, as well as the specific forms of the equations used to interpret those photoacoustic data.

2.1 THE THEORY OF PHOTOACOUSTIC CALORIMETRY

2.1.1 The Fundamental Photoacoustic Equation

When a molecule absorbs light, some portion of the absorbed photon energy will be deposited to the surrounding molecules as heat. A general Jablonski diagram showing possible outcomes of photoexcitation is shown in Figure 2-1. In this figure, a photon with a given excitation energy (E_{exc}) is absorbed by an analyte molecule. Thermal relaxations to the lowest vibrational state of each electronic level (red curvy lines) result in a heat deposition to the surrounding solvent molecules. The quantum yield of each possible process (internal conversion to the ground state, fluorescence, intersystem crossing/phosphorescence, intersystem crossing/energy transfer or chemical reaction, and photodissociation) indicates the fraction of excited molecules that will relax along that pathway.

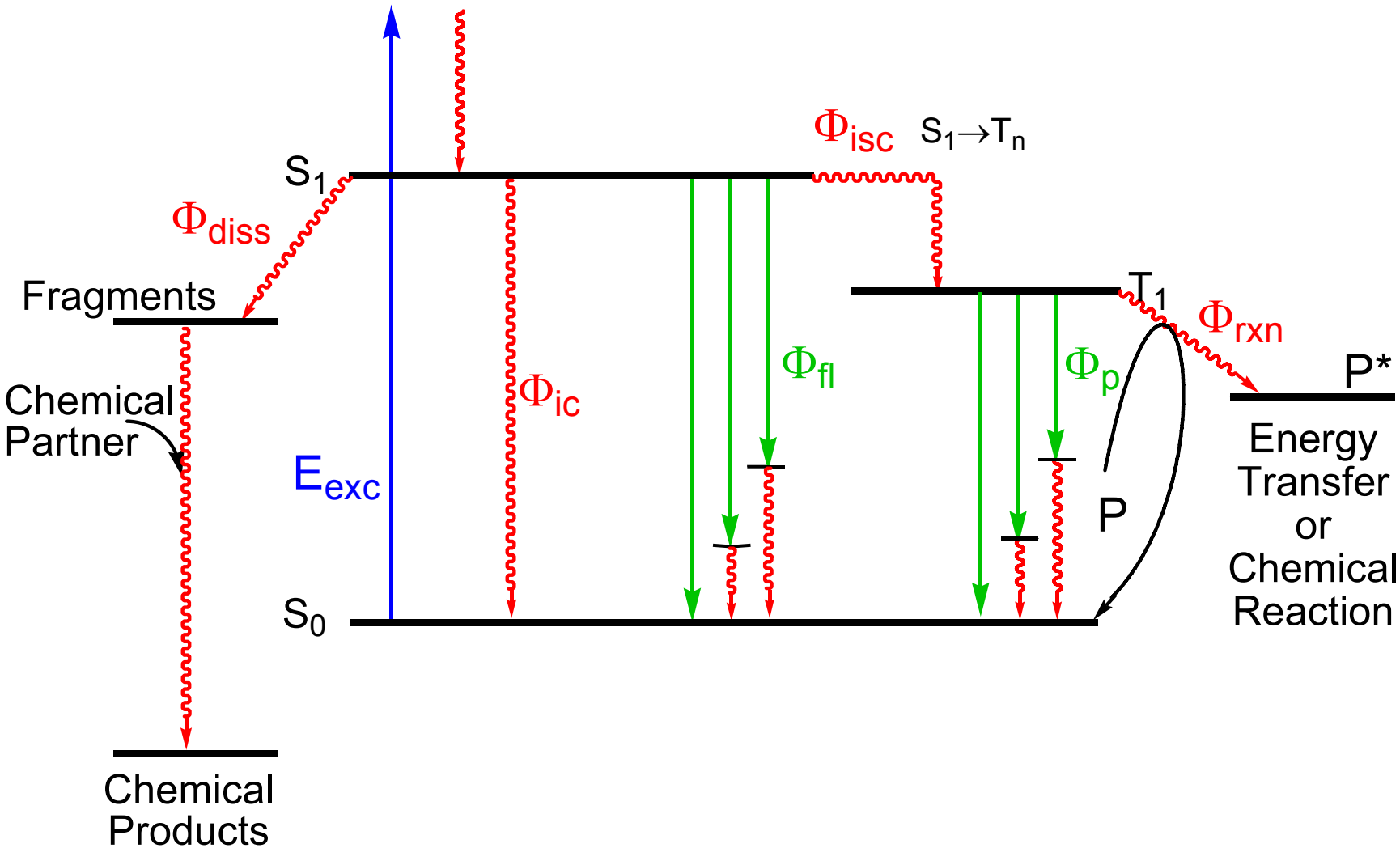

Figure 2-1 General Jablonski diagram for possible outcomes of the photoexcitation of an analyte. Thermal relaxations are highlighted by red (curvy) arrows.

Heat depositions to the surroundings will result in a local volume expansion, which will propagate as a pressure (i.e. sound) wave. To a first approximation, this may be treated as the only process yielding a photoacoustic signal. For this case, a photoacoustic equation can be built up by considering each process involved in sequence. The analyte is photoexcited by absorbing

$$E_{absorbed} = E_p(1 - 10^{-A}) \tag{2-1}$$

some fraction ($1 - 10^{-A}$) of a light pulse of a particular energy (E_p), as described in Equation 2-1. This energy is partitioned through the possible photochemical processes, and some fraction of

$$Q = f_h E_{absorbed} = f_h E_p (1 - 10^{-A}) \tag{2-2}$$

this energy (f_h) is deposited to the solvent as heat (Q) as in Equation 2-2. The acoustic wave then propagates through the solvent at the speed of sound in that medium; the solvent affects the intensity of the acoustic wave based upon its expansivity (for solvents with lower expansivities, the acoustic intensity is dampened). It is then measured with some efficiency by the transducer; these experimental effects (and others) are accounted for by an experimentally determined

$$S_{obs} = \kappa Q = \kappa f_h E_p (1 - 10^{-A}) \tag{2-3}$$

constant (κ). Inclusion of κ in Equation 2-2 results in Equation 2-3, which relates the intensity of the photoacoustic signal observed (S_{obs}) to the amount of heat deposited to the solvent, and is typically referred to as the fundamental photoacoustic equation.

In a PAC experiment, the photoacoustic wave is measured in order to determine f_h. First, a photoacoustic standard is measured; for this standard, f_h is known (typically $f_h = 1.00$). By measuring the sample absorbance on a UV-vis spectrophotometer, it is straightforward to determine κ for that experiment. This measurement of κ allows f_h to be determined for an analyte so long as no experimental factors have changed (*e.g.* transducer/cell acoustic coupling,

cell/laser alignment) during the acquisition of the data; care is taken during the course of the experiment to ensure no part of the instrument is inadvertently moved. To improve the determination of κ and f_h, the incident energy (E_p) is varied, and the slope of the data plotted according to Equation 2-3 is used (rather than a single measurement); an example of this plot is shown in Figure 2-2. The sharp negative peak at 2 μs is a noise peak caused by the firing of the laser; the signal before this time serves as a baseline measurement. The positive portion of the photoacoustic signal has been truncated to maximize the resolution of the negative portion. A portion of this negative signal excursion is integrated to yield S_{obs}. This signal measurement is repeated for various incident laser energies (typically 7) for each analyte or standard. A single experiment typically measured at least two different standards, and measured the analyte twice. The slopes of the standards were averaged, providing κ, and the slopes of the analytes were averaged to yield $f_h\kappa$; combining these measurements provided f_h for a single experiment.

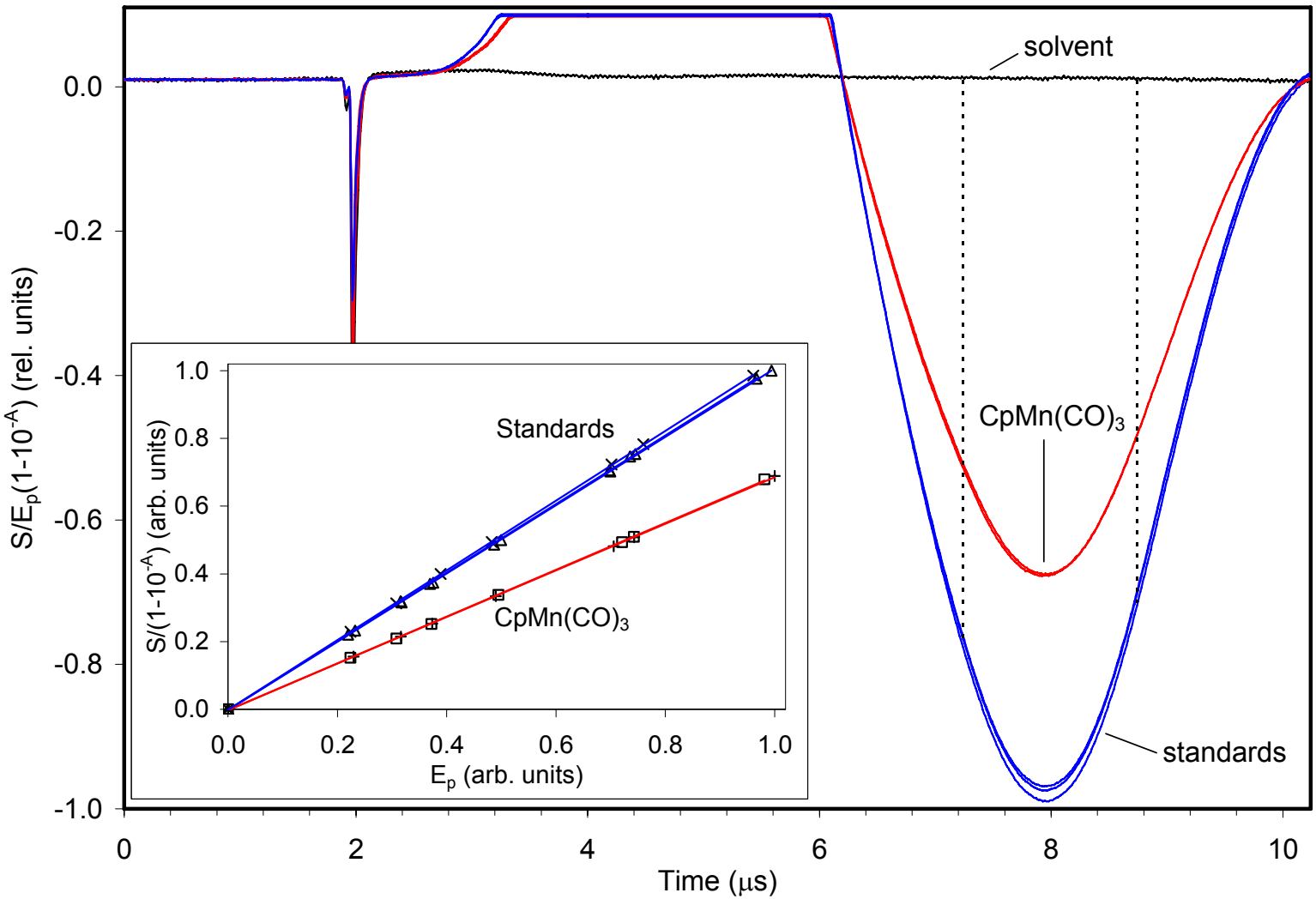

Figure 2-2 An example of PAC signals. Inset: PAC signals plotted according to Equation 2-3, allowing accurate determination of κ and f_h

2.1.2 Separating the Enthalpic and Volumetric Contributions to the Photoacoustic Signal

Equation 2-3 is valid when the entire volume change stems solely from the deposition of heat to the solvent. If the heat deposition process is accompanied by a difference in the solvated volumes of the reactants and products (i.e. $\Delta V_{rxn} \neq 0$), there will be a second contribution to the photoacoustic wave that must be explicitly accounted for, as in Equation 2-4. In this case, an individual experiment is actually measuring f_h^{obs} rather than f_h, and Equation 2-3 should be restated as in Equation 2-5. In the following chapters, this dissertation will carefully consider cases where failure to differentiate between f_h and f_h^{obs} leads to substantial errors in determining reaction enthalpies.

$$S_{obs} = S_{thermal} + S_{volume} \tag{2-4}$$

$$S_{obs} = \kappa f_h^{obs} E_p (1 - 10^{-A}) \tag{2-5}$$

κ includes solvent-dependant viscous dampening effects alongside other experimental factors. κ is sometimes expanded to allow the solvent expansivity (X_s) to be explicitly accounted for ($\kappa = \kappa' X_s$). If this expanded form of the instrumental response constant is combined with Equations 2-4 and 2-5, an equation that explicitly accounts for the accompanying volume change results (Equation 2-6). This equation may be further simplified into the form show in Equation

$$S_{obs} = \kappa' f_h^{obs} E_p (1 - 10^{-A}) + \kappa' E_p (1 - 10^{-A}) \frac{\Delta V_{chem}}{h\nu} \tag{2-6}$$

2-7; this form of the equation shows that by conducting measurements of f_h^{obs} for various X_s, it is possible to recover both f_h and ΔV_{chem} (the volume change accompanying the chemical reaction measured in the experiment).

$$f_h^{obs}\, h\nu X_s = f_h h\nu X_s + \Delta V_{chem} \tag{2-7}$$

The solvent expansivity ($X_s = \alpha\,\mathrm{MW} / C_p\,\rho$) depends upon the thermal expansion coefficient (α), the molecular mass, the molar heat capacity (C_p), and the density (ρ) of the solvent. X_s has been experimentally controlled via three different approaches. For analytes that are soluble in water, the expansivity may be modified by changing the temperature. This approach uses the same solvent throughout, ensuring consistent solvent effects, but it is limited by a narrow expansivity range (0 – 100°C gives an expansivity range 0.8 mL/kcal wide). For analytes soluble in organic solvents, the solution may be placed under high pressures to decrease X_s. This approach has an even more narrow range of X_s (0.3 mL/kcal), further limiting the quality of f_h and ΔV_{chem}. The third approach uses a homologous solvent series (in this case, linear alkanes), and operates under the assumption that the analyte has the same enthalpy and volume of reaction across this series. This method allows the widest range of expansivities to be used; this series runs from pentane (the smallest liquid linear alkane under ambient conditions) to hexadecane (the largest liquid linear alkane under ambient conditions) and spans 2.5 mL/kcal. The f_h^{obs} measured in each solvent are plotted using Equation 2-7 (*e.g.* Figure 2-3), separating the enthalpic and volumetric contributions.

Ultimately, the quantum yield for the processes allows f_h and ΔV_{chem} to be interpreted into ΔH_{rxn} and ΔV_{rxn} using Equations 2-8 and 2-9.

$$f_h = \frac{h\nu - \Delta H_{rxn}\Phi_{diss}}{h\nu} \tag{2-8}$$

$$\Delta V_{chem} = \Delta V_{rxn}\Phi_{diss} \tag{2-9}$$

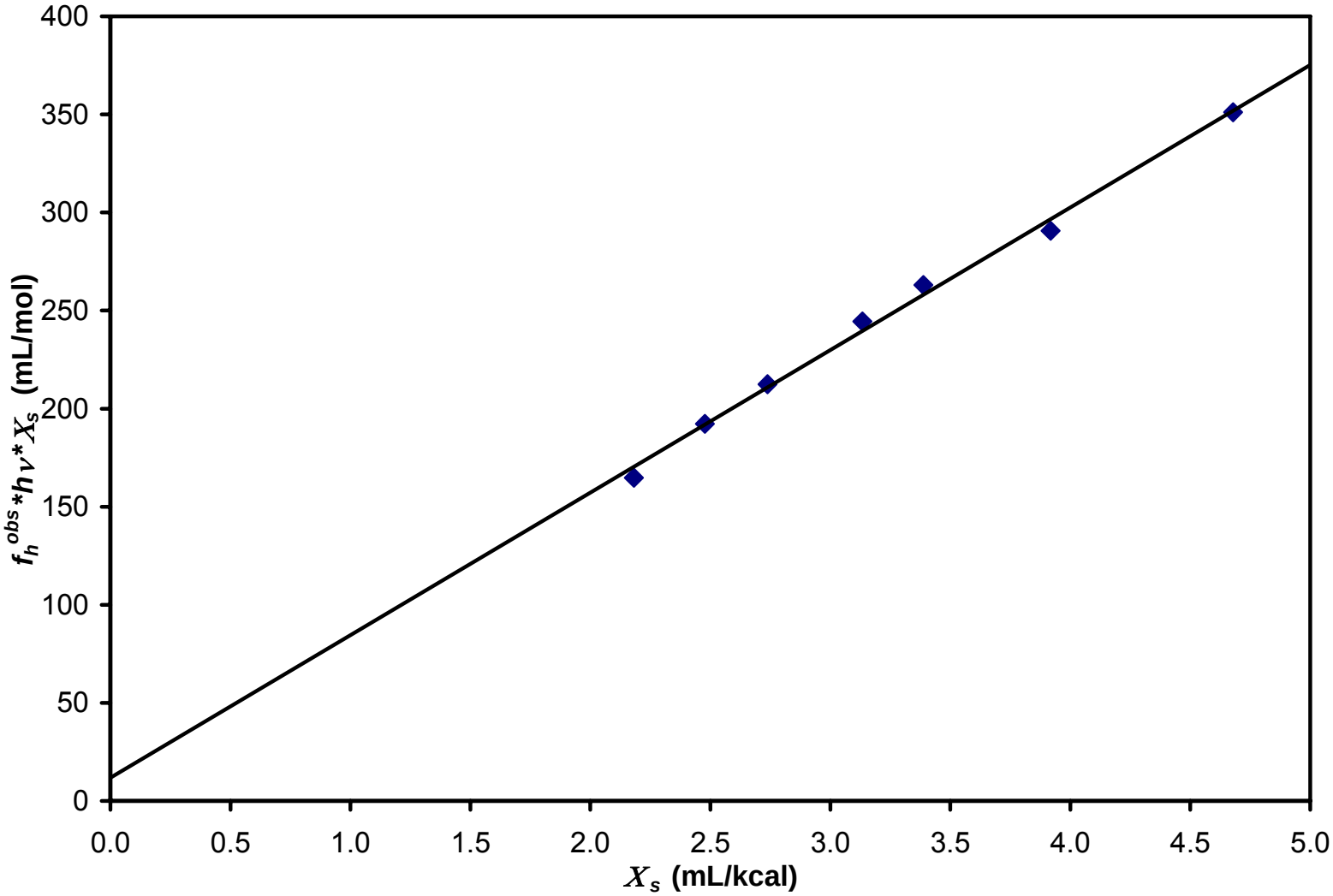

Figure 2-3 Representative plot showing the determination of f_h (slope) and ΔV_{chem} (intercept) from f_h^{obs} measured in various linear alkanes, using Equation 2-7

Equations 2-7 through 2-9 are well-suited to analyzing PAC data for which the quantum yield has been determined to be invariant. These three equations must be combined into the form of Equation 2-10 in order to account for quantum yields which demonstrate solvent-dependence.

$$\frac{\left(1 - f_h^{obs}\right) h\nu \mathrm{X}_s}{\Phi_{diss}} = \Delta H_{rxn} \mathrm{X}_s - \Delta V_{rxn} \tag{2-10}$$

2.2 THE PHOTOACOUSTIC CALORIMETER

All experiments described this dissertation were performed on a custom-built photoacoustic calorimeter, shown in Figure 2-4. The working of the photoacoustic calorimeter are described in three sections: a description of the light source used to photoexcite our samples; a detailed explanation of the physical apparatus used to make the individual measurements recorded in a PAC experiment; and a description of the signal collection electronics.

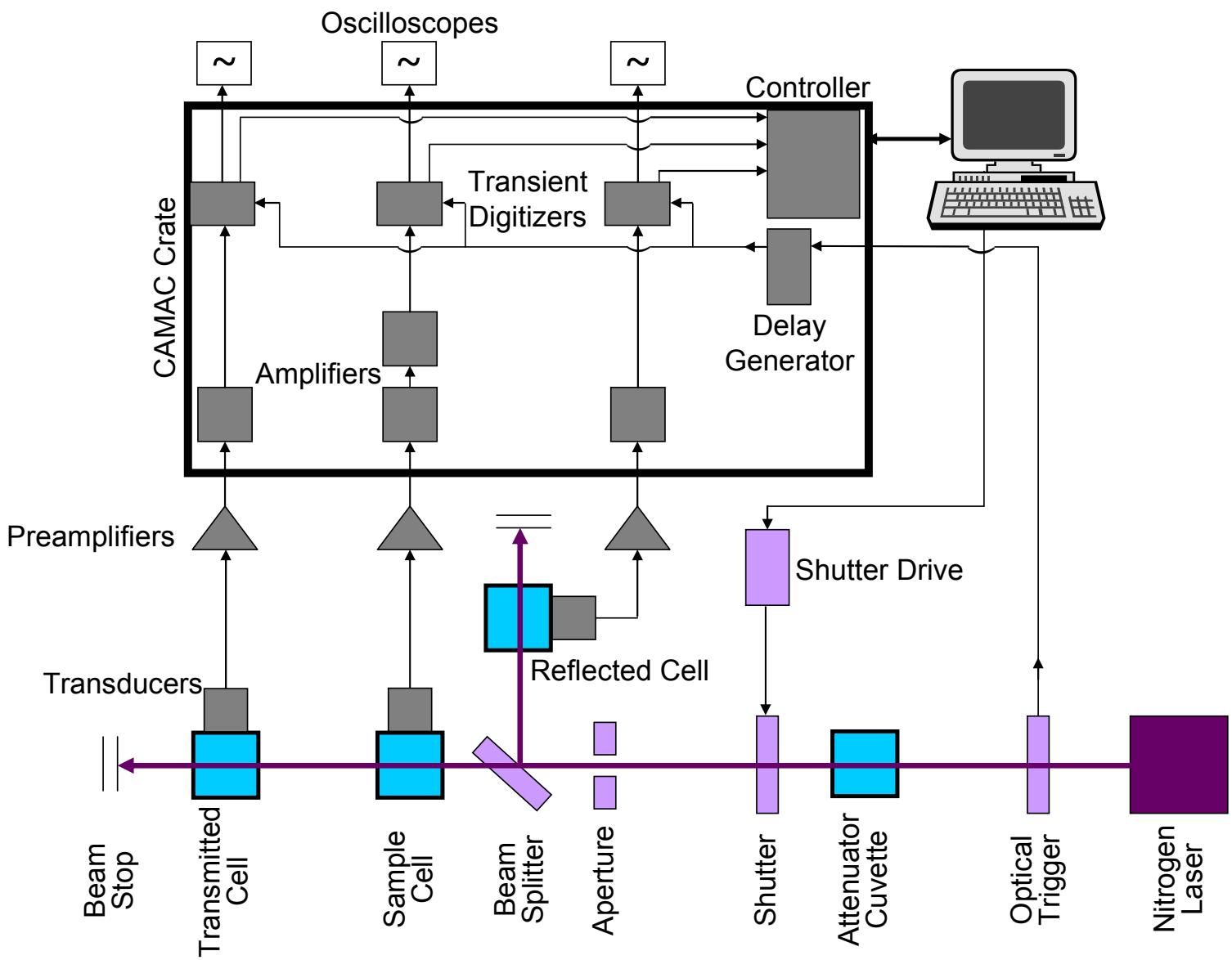

Figure 2-4 Layout of the photoacoustic calorimeter used in this work

2.2.1 Light Source

The light source used in these experiments is a Laser Photonics Model LN-1000 pulsed nitrogen gas laser. This pulsed laser is operated in a free-run mode, which results in a more even shot-to-shot pulse energy than in its triggered mode. The laser emits light at 337.1 nm, with a temporal peak width of ~1 ns. The total laser pulse energy is rated as 1.3 mJ/pulse. The beam energy varies considerably throughout the rectangular-shaped beam; a small uniform portion of a high-intensity region of this beam this beam is passed to the rest of the instrument. The laser pulse repetition rate is user-selectable and was maintained in the range of 1-2 Hz for our PAC experiments. Our laser is typically run with a discharge capacity of 18-20 kV. Though the laser head is shielded, this discharge energy results in a large (but short-lived) burst of electromagnetic noise that is recorded by our detection electronics. This noise burst is used in our PAC data analysis as an indicator of the exact time when the laser was fired (*e.g.* Figure 2-2).

2.2.2 Light Path

Upon exiting the laser aperture, the laser beam is passed through a beam splitter/photodiode (custom-built), which is used to provide a trigger signal to the data collection electronics. The beam is then passed through an attenuation cuvette, in which solutions of various absorbances (usually ferrocene/acetonitrile) are used to decrease the laser intensity (E_p). The concentrations of the attenuation solutions are not closely monitored, as their only purpose is to modify E_p, which is measured in the course of the PAC experiment.

A computer-controlled optical shutter (A. W. Vincent Associates, Model 26L) is used to ensure that the samples are only illuminated by the laser during active data collection. When open, this shutter reduces the laser beam to 6.4 mm in diameter; this aperture is qualitatively positioned such that the measured photoacoustic signal is of sufficient intensity. During data collection, the shutter is held open until after a laser pulse is detected by the optical trigger, then closed after the laser has fired.

The beam is passed through a user-adjustable aperture (typically 1-3 mm in diameter) to further reduce the beam dimensions. Each laser pulse is then split into two portions by a beamsplitter; the smaller portion of the pulse is reflected for measurement of E_p, while the bulk is used for the PAC measurement and a real-time absorbance measurement. These two measurements are performed with three photoacoustic cells, all of which are built identically (shown in Figure 2-5).

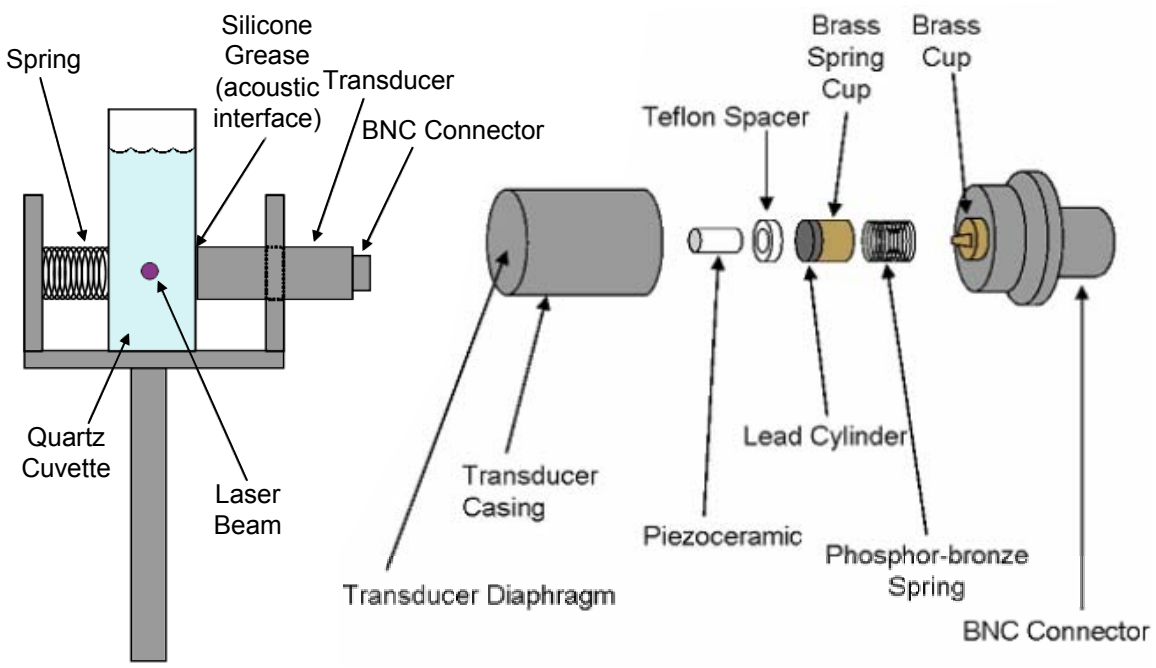

Figure 2-5 The photoacoustic cell and photoacoustic transducer (drawings not to scale)

The quartz cuvette containing the solution is spring-loaded against the surface of a custom-built photoacoustic microphone, which is based on the design of Tam and Patel.[24] A thin layer of vacuum grease is applied between the cell and microphone to provide acoustic coupling. Our microphone uses a 500 MHz piezoceramic transducer element (Transducer Products Model LTZ-2, 4 mm diameter) to convert the photoacoustic pressure wave into a voltage signal.

The reflected and transmitted cells shown in Figure 2-4 provide a relative measure of the energy incident upon that cell, allowing these two cells to serve (respectively) as a measurement of E_p or the amount of light transmitted through the sample cell. Typically, a ferrocene/acetonitrile solution is used in these cell positions to efficiently convert the incident

light energy into heat. This configuration allows the intensity of either signal to be easily adjusted by modifying the solution absorbance, allowing us to fully utilize the voltage resolution of the digitizer.

2.2.3 Signal Collection

A preamplifier (Panametrics Model 5660B, 0.2 – 2 MHz) is used to amplify each of the three photoacoustic signals (sample, reflected, and transmitted) by 60 dB (*i.e.* 1000x amplification) Each of these three signals are then passed to a second amplifier (LeCroy Model 6102, 150 MHz), which provides variable gain settings (0.2 – 10x). Since the sample signal is often weaker than the reflected and transmitted signals (lower absorbance, f_h), it is passed through a second of these amplifiers. The amplifications are chosen such that the full range of the signal spans up to 512 mV.

When the laser fires, the optical trigger passes a signal through a delay generator (Philips Scientific Model 7194). This delay generator passes the trigger signal to each of the three digitizers used to record the photoacoustic signal, allowing each of these digitizers to be given an independently-tuned trigger signal. The reflected and transmitted signals are each recorded by a 20 MHz digitizer (DSP Model 2008A, 8 bits, 50 ns resolution, 512 mV range), which typically records 512 time samples (record length 25.6 μs). The sample signal is recorded with a 100 MHz digitizer (DSP Model 2001A, 8 bits, 10 ns resolution, 512 mV range), which typically records 1024 time samples (record length 10.2 μs).

The digitizers are set to record continuously while awaiting the firing of the laser. When the digitizer receives the trigger signal from the delay generator, it keeps the newest fraction of points in its memory from before this trigger, and overwrites the remainder with data from after

the trigger signal; this fraction is set by the user at the beginning of the PAC experiment. All three digitizers record both a pre-firing baseline, and a post-firing waveform. The ratio between the number of 'baseline' and 'signal' points may be further fine-tuned by manipulation of the delay time setting for that signal on the delay generator.

After recording each laser pulse, each of the digitizers transfers the data in memory to the instrument's computer via a GPIB interface. The digitizers also output an analog copy of the signal for real-time display on an oscilloscope, allowing the operator to observe each of the three signals for each laser pulse.

The PAC uses a custom control/acquisition program, which is described in detail in [25]. This program collects the individual photoacoustic signals for each of the three PAC positions (reflected, transmitted, and sample), and performs some rudimentary error-checking for each of the three signals on a pulse-by-pulse basis, to ensure that grossly deviant waveforms are excluded from the collected signal average. The operator selects a number of 'good' waves; the program then compares each of the signals resulting from a single laser pulse against the average of these user-selected signals. All data from a laser pulse is excluded if any of the following conditions are met vs. the selected waves: any baseline deviates by >10 mV; E_p varies by >10%; the peak to be measured is cut off by the max/min of the digitizer range; a GPIB data transfer error occurs.

Typically, 'good' data for 30-100 laser pulses are averaged by the program and saved to disk for later analysis. This data is collected for 6-8 E_p per sample (this is referred to as a 'run'). Usually, 2-3 runs are performed for performed for the solution of interest, 1 run is performed for each of 2-3 photoacoustic standards, and 1 run is performed for a sample of pure solvent. The spreadsheet code I have written to determine $f_h^{obs}\kappa$ from each run is found in Appendix A.

2.3 ACTINOMETRIC MEASUREMENTS

Photoacoustic data can either be used to determine reaction enthalpies (with knowledge of accurate quantum yields) or quantum yields (with complete knowledge of the energetics of the involved states). In photoacoustic calorimetry, we are typically interested in understanding the energetics of photoinitiated reactions, which requires that accurate quantum yields have been reported or that we measure them ourselves.

Quantum yields have been reported in at least one linear alkane for each of the reactions studied in this dissertation. However, to ensure high-quality enthalpic and volumetric measurements via the linear alkane method, it was necessary to ascertain whether or not the quantum yield demonstrated any solvent dependence over the linear alkane range. This was generally possible from literature results alone, but in the case of $CpMn(CO)_3$, it was necessary to perform actinometric measurements for pentane and hexadecane (the extrema of our solvent series). This section discusses the conversion of our photoacoustic calorimeter into a suitable apparatus for actinometric measurements, and details the analysis involved. The specific experimental details of this measurement may be found in Section 3.3.3.

2.3.1 Experimental Setup

The photoacoustic calorimeter can serve as a sensitive measure of the number of incident photons when calibrated with a chemical actinometer such as potassium ferrioxalate. In order to perform actinometric experiments, our photoacoustic calorimeter was modified as shown in Figure 2-6.

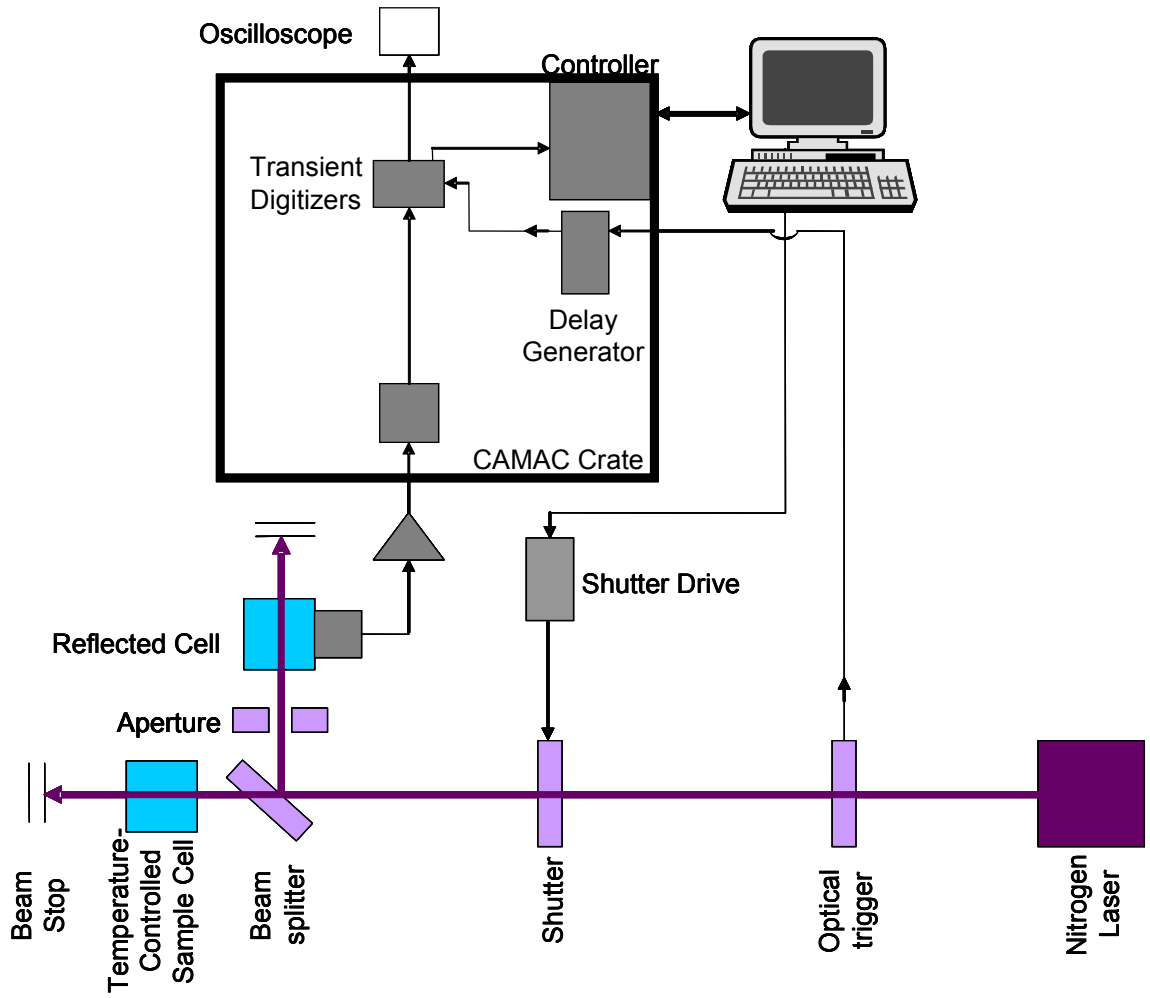

Figure 2-6 Modified photoacoustic calorimeter for actinometric measurements.

This apparatus used the same laser as in the PAC measurements, ensuring both measurements were performed under nearly identical excitation conditions. The laser passed through an optical trigger, which served as a trigger signal for the photoacoustic data collection system. A computer-controlled shutter ensured the sample was only photoexcited during active data collection. When the shutter was opened, the laser beam was split into two portions. The

reflected portion of the beam passed through an adjustable aperture, reducing the beam width to dimensions comparable to those in a normal PAC experiment. The beam was then directed to a PAC cell, which served as our photon-counting device. The remainder of the laser beam illuminated a quartz spectrophotometer cell mounted within a temperature controlled brass block. This portion of the laser beam was ~5 mm in width (wider than a typical PAC experiment), in order to maximize the number of photoexcited molecules without affecting the incident power ($\mu J/cm^2$); this maintained PAC-like conditions while improving the ultimate quality of the quantum yield measurement, which is dependent upon the measurement of ΔA. The temperature-controlled cell alternately held either the chemical actinometer, which was used to calibrate the reflected-position PAC cell, or the metal-carbonyl sample.

2.3.2 Photoacoustic Actinometry Data Analysis

When ferrioxalate absorbs a photon, it generates Fe^{2+} ($\Phi = 1.23$) which readily complexes with phenanthroline. By monitoring the production of Fe^{2+}, it is possible to determine the number of photons that were incident upon the photoacoustic cell, which in turn allows the PA signal to be calibrated to measure the absolute number of photons which entered the sample cell during irradiation. This analysis requires a two-part calibration. First, the absorbances of known concentrations of Fe^{2+}/phenanthroline complex are measured, generating a calibration curve relating absorbance vs. [Fe^{2+}/phenanthroline]. Next, ferrioxalate is photoexcited while collecting the PAC signal from the reflected position, and the Fe^{2+} generated in the sample position is complexed with phenanthroline and the absorbance is measured, relating [generated Fe^{2+}] to the PA signal. By using the quantum yield for ferrioxalate and the absorbance of the ferrioxalate

solutions, we can determine the relationship between the number of incident photons and the photoacoustic signal.

To ensure the best-quality PA signal, the data acquisition digitizer was set to truncate the positive portion of the PA wave, maximizing the available resolution for the negative excursion. A portion of this negative excursion was integrated, and this area served as the numerical PA signal for the calibration curves. At least 200 PA waves were summed per $CpMn(CO)_3$ sample, and 200 digitized points in the PA wave were integrated, both of which served to maximize signal-to-noise.

3.0 CHARACTERIZATION OF THE REACTION ENTHALPY AND VOLUME FOR THE PREPARATION OF A REACTIVE INTERMEDIATE FROM CYMANTRENE

Reprinted from (with permission from Elsevier):

Kevin W. Davies, David Maivald, and Joseph J. Grabowski. A Photoacoustic Calorimetric Characterization of the Reaction Enthalpy and Volume for the Preparation of a Reactive Intermediate from $CpMn(CO)_3$, *J. Photochem. Photobiol., A* **2008,** 197, (2-3), 335-341.

3.1 ABSTRACT

Photoacoustic calorimetry (PAC) allows measurement of the energetics of reactive intermediates. Here, we report the examination of the metal carbonyl η^5-$CpMn(CO)_3$ (Cp = cyclopentadiene) via time-independent PAC, in a homologous series of solvents. The measured heat releases allow one to determine simultaneously the enthalpy and volume change resulting from the photodissociation of $CpMn(CO)_3$. While the photoacoustic signal results from both of these processes, it has often been assumed that the volume change contribution to the observed photoacoustic signal is negligible for small molecules undergoing photodissociation. The current study tests the assumption of a negligible reaction volume by using a more complete treatment. The reaction of an equimolar number of photons and $CpMn(CO)_3$ molecules, the

subsequent photodissociation of the Mn-CO bond, and the ligation of a solvent molecule in an alkane solvent yields ΔH_{obs} = 32.7 ± 0.7 kcal/mol and ΔV_{chem} = 11.0 ± 1.3 mL/mol, both of which are independent of the quantum yield of photodissociation. A detailed analysis of the quantum yield is included (using both previously reported measurements, and new data from this work), from which we determine Φ_{diss} = 0.635. This quantum yield allows us to determine ΔH_{rxn} = 51.6 kcal/mol and ΔV_{rxn} = 17.3 mL/mol. These results demonstrate that if the contribution of the reaction volume change to the photoacoustic signal is ignored, the reaction enthalpy derived would underestimate the true value by 7%. We also estimate the BDE{$Cp(CO)_2Mn–CO$} to be 59.4 kcal/mol.

3.2 INTRODUCTION

Over the last few decades, organometallic systems have been the focus of a number of detailed studies due to their increasingly appreciated role in biological and synthetic systems.[26-31] Transition metal reagents have been quite successful to date in C-C and C-H bond activation of otherwise unreactive bonds,[29-31] but much remains unknown about how to tailor reagents to approach those desirable capabilities found in biological systems. To that end, better knowledge of the energetics of these molecules may help to understand the interactions that drive these organometallic reactions.

Photoacoustic calorimetry (PAC, also known as laser-induced optoacoustic calorimetry, LIOAC) has been used to determine the reaction enthalpies of photoinduced processes,[2-8] to determine the heats of formation of reactive intermediates,[9-11] to determine quantum yields,[12] and to determine the kinetics and lifetimes of transient intermediates [13-16]

(citations are representative, not exhaustive). In PAC, a molecule undergoes photoexcitation followed by thermal relaxation; a pressure wave results, which may be measured and analyzed to recover kinetic and enthalpic information simultaneously. In many PAC studies carried out in organic solvents, the entire photoacoustic signal has been assigned to the thermal relaxation of the photoexcited species, i.e. assuming that $\Delta V_{rxn} = 0$. In this study, we examine the contribution of ΔV_{rxn} to the photoacoustic signal to probe the acceptability of the assumption of a negligible reaction volume. To date, few examples of the ΔV_{rxn}'s contribution to photoacoustic signals have been documented for systems in organic solvents. For aqueous systems, where the solvent expansivity is often a factor of ten or more smaller than for organic solvents, consideration of non-thermal contributions to the photoacoustic signal typically are treated explicitly.[11, 17-20] To separate the contribution of the volumetric and enthalpic changes to the photoacoustic signal, solvent expansivity can be varied by: (i) changing the temperature (if the solvent has significant expansivity dependence on temperature as is the case for water);[11] (ii) varying the pressure;[21] (iii) or using a homologous series of solvents over which ΔH_{rxn} will be unaffected.[22] This last method, which utilizes linear alkanes as its solvent series (in which relative solvation effects are constant, but for which the solvent expansivity varies)[23] is considerably easier to experimentally conduct than the high-pressure approach.[21]

Here, we report the use of a series of linear alkanes as solvents in the determination of the reaction enthalpy for the photodissociation of a carbon monoxide from a metal compound, while explicitly accounting for the reaction volume contributions to the photoacoustic signal. ΔH_{rxn} is considered both with/without accounting for ΔV_{rxn} in order to ascertain the magnitude of neglecting the volumetric term. We chose $CpMn(CO)_3$ (Cp = cyclopentadiene) because of its usefulness in synthetic routes as well as the fact that it has been examined in several previous

kinetic and thermodynamic studies.[32] The photodissociation of CO from $CpMn(CO)_3$ has been studied by PAC in heptane; in those studies, the entire photoacoustic signal was attributed to the thermal expansion of the solvent due, in turn, to the heat released following the absorption of a photon and photofragmentation (Equation 3-1).[1, 33-37]

$$CpMn(CO)_3 + h\nu \xrightarrow[\text{solvent}]{} CpMn(CO)_2(\text{solvent}) + CO + \text{heat} \tag{3-1}$$

$$CpMn(CO)_2(\text{solvent}) + \text{nucleophile} \xrightarrow[\text{solvent}]{} CpMn(CO)_2(\text{nucleophile}) + \text{solvent} \tag{3-2}$$

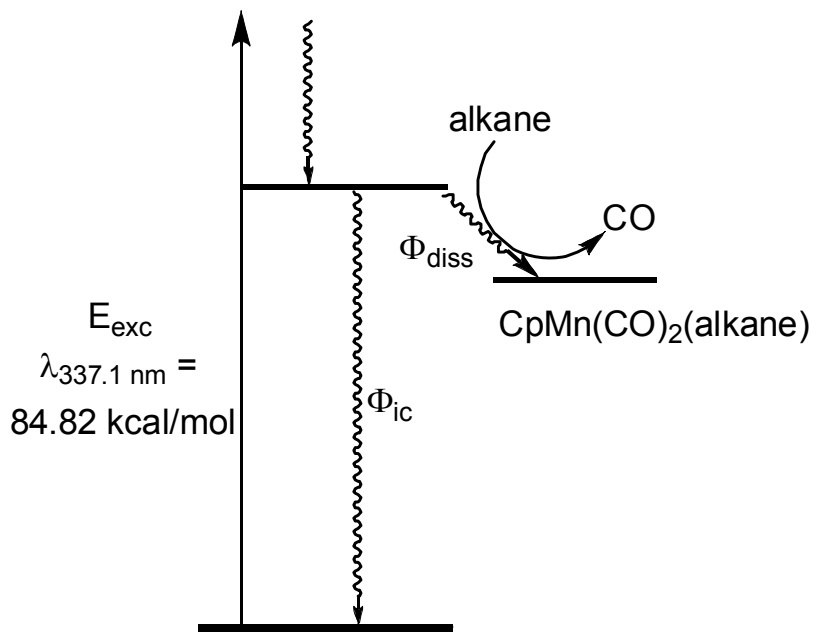

Figure 3-1 Jablonski diagram for the photoprocesses relevant to the PAC measurement of $CpMn(CO)_3$. As the lifetime of $CpMn(CO)_2$(alkane) is on the order of seconds in the absence of nucleophiles,[38] its decay pathways are too slow to impact the PAC measurement [39]

Figure 3-1 diagrams the processes occurring upon photoexcitation which occur during the time resolution window of our instrument. Upon photoexcitation with a near-UV photon, $CpMn(CO)_3$ is promoted to an excited state, followed by CO dissociation from the metal center.[40] A solvent molecule is then agostically bound in the empty ligand site.[41] Both the photodissociation and the solvent ligation processes occur much faster (70 fs and 120 ps) than the resolution limit of our detector (10 ns).[11, 40, 41] In the absence of a nucleophile, the reaction proceeds as summarized in Equation 3-1, and the 'too-fast' PAC treatment applies (i.e. the processes are indistinguishable from a concerted reaction).[14] If a nucleophile (*e.g.*, pyridine) were to be present, the nucleophile would replace the ligated solvent molecule on a 10^{-7} – 10^{-6} s time scale (depending on nucleophile concentration) (Equation 3-2).[42] The simultaneous heat depositions would result in a unique waveform containing contributions from each of the two heat release pathways (Equations 3-1 and 3-2), causing a phase shift in the observed photoacoustic signal with respect to the reference wave. The signal may be deconvoluted into its composite waveforms to recover information about processes in the resolvable time scale (10^{-8} - 10^{-5} s) via the 'time-resolved' treatment.[14, 43, 44]

Previous work on $CpMn(CO)_3$, both photoacoustic and otherwise, has focused on measuring the enthalpy or the kinetics (or both) of the processes shown in Equations 3-1 and 3-2, and did not consider ΔV_{rxn}.[1, 33-37] In this study, we test the assumption that volume treatment is unnecessary for $CpMn(CO)_3$, and report the difference in results between the volume-dependant and volume-independent treatments for $CpMn(CO)_3$ photodissociation and thereby. In doing so, we are able to establish the best value for the enthalpy of the liquid-phase reaction shown in Equation 3-1. Furthermore, by comparing that result to an estimate of the agostic interaction, we are able to derive the BDE{$Cp(CO)_2Mn$–CO}.

3.3 EXPERIMENTAL

3.3.1 General

All compounds used in this work were of the highest purity available, and all solvents were reagent grade; all were obtained from commercial sources. $CpMn(CO)_3$ was purified by vacuum sublimation. Ferrocene (FER) was recrystallized twice from hexane. Tetraphenylethylene (TPE) was recrystallized from ethanol/hexane. 2,4-dihydroxybenzophenone (DHBp) was used as received. Pentane and octane were used both as received and after purification by washing with basic $KMnO_4$ and drying with $CaCl_2$. As no difference in photoacoustic measurements were observed in pentane or octane purified in this manner/used as received, all subsequent measurements were performed without further preparation. In our quantum yield measurements, potassium ferrioxalate, pyridine, and 1,10-phenanthroline were used as received.

3.3.2 Photoacoustic Calorimetry

The photoacoustic calorimeter used has been previously described in detail and so only the key aspects are summarized here.[11] Sample absorbances (as measured by a Hitachi U-2000 spectrophotometer) ranged from 0.130 to 0.260, and all solutions were matched within 0.005 absorbance units in a single experiment. A nitrogen laser (Laser Photonics Model LN-1000, 337.1 nm, fwhm ~ 1 ns, 1.3 mJ/pulse, ~2 Hz repetition rate) was used for photoexcitation, while a computer-controlled shutter ensured the sample was only irradiated during data acquisition. The excitation pulse passed sequentially through a 1 mm circular aperture and then through a 10 mm quartz cuvette containing ferrocene/acetonitrile of varying optical density. These two

components worked together to reduce the excitation pulse to ≤ 15 μJ; these low pulse excitation energies are used to minimize the occurrence of multiphoton events. The laser pulse then passed through a beam splitter where ~30% of the pulse was reflected into a reference cell containing a photoacoustic standard (either ferrocene or tetraphenylethylene). The photoacoustic signal generated by this reference cell served as a relative measure of pulse energy. The remaining portion of the beam passed through a photoacoustic cell containing the sample. A third cell containing a photoacoustic standard (the 'transmitted' cell) was placed such that it measured the portion of the beam remaining after excitation of the sample; this cell allowed in-situ monitoring of the sample absorbance. Each photoacoustic cell (sample, reference, and transmitted) consisted of a 10 mm quartz cuvette spring-loaded against a custom-built piezoelectric microphone, described elsewhere.[45] The photoacoustic standards used, FER,[46] DHBp,[47] and TPE,[48] are known to absorb at 337.1 nm excitation without occurrence of photoinitiated reactions and to release all absorbed energy as heat faster ($\tau < 10$ ns) than the resolution of our transducer (i.e., $f_h = 1.00$). The signal recorded for the standard was used to determine the instrumental response factor (κ', described in Section 3). If in the sample waves a phase-shift were to be observed versus the reference waves, it would indicate the need to use 'time-resolved' PAC. The time window, during which the photoacoustic signal (Figure 3-2) was acquired, was chosen such that pre and post-laser-firing data were recorded in order to capture baseline and the first positive and negative excursions.

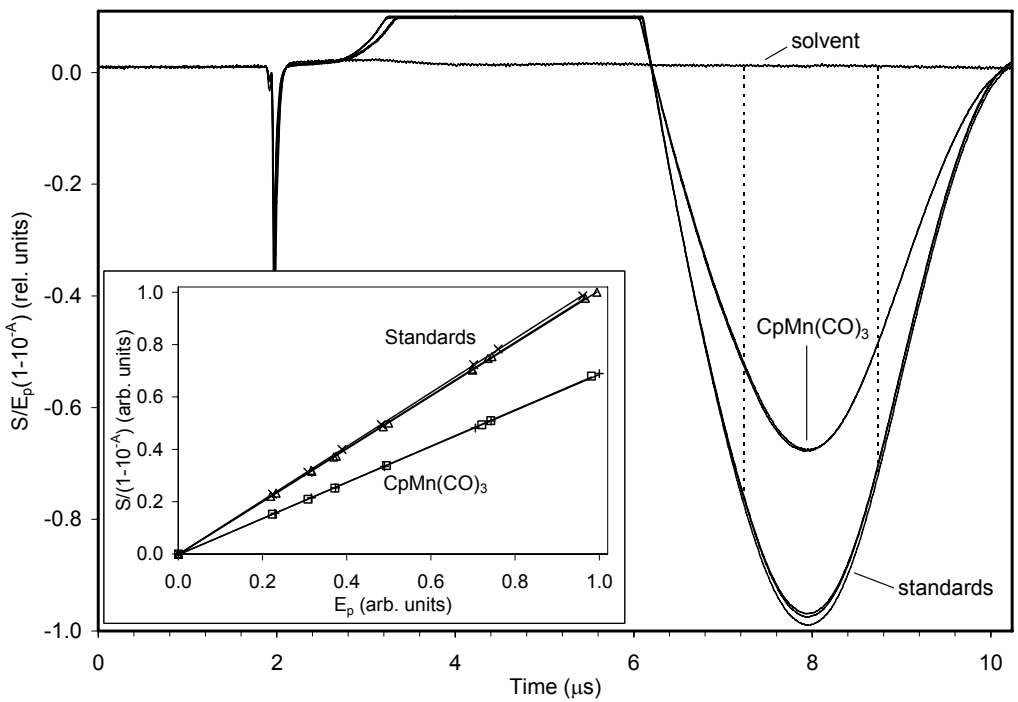

Figure 3-2 Averaged waves (30 shots) from a typical PAC experiment at a single laser energy. Inset: PAC signals for $CpMn(CO)_3$ and two standards plotted according to Equation 3-3

Shown are three waves from standards (2 ferrocene, 1 DHBp) and two from $CpMn(CO)_3$, along with that for pure solvent. The noise spike at ~2 μs corresponds to the firing of the laser. Data before this point serves to define the baseline for wave integration. Integration limits are shown by dashed lines. To maximize sensitivity of the 8-bit digitizer, the baseline of the acoustic wave is deliberately offset to ensure the first negative excursion of the wave is recorded with the best possible S/N ratio. The first positive excursion of the wave is therefore 'clipped' and not fully captured.

3.3.3 Quantum Yield Determination

In photoacoustic calorimetry, a quantum yield (Φ = (# of events) / (# of molecules absorbing a photon)) is needed to extract the fundamental thermodynamic properties of the system under investigation (*vide infra*, Equations 3-7 and 3-8). The quality of ΔH_{rxn} and ΔV_{rxn} determined is limited in part by the how well Φ_{diss} is known. For this study, where we will examine the photoacoustic signal for one reaction across a homologous series of solvents, it is important to ascertain if the quantum yield of photodissociation for $CpMn(CO)_3$ varies over the solvents used. To determine if there is a solvent dependence for this quantum yield, Φ_{diss} was determined in both hexane and hexadecane, the extrema of the solvent range (pentane was not used out of concern over its fast rate of evaporation and the resulting possibility of an unaccounted for increase in concentration).

In order to perform the actinometry experiments, the photoacoustic calorimeter was used in a slightly modified form. Laser intensities were maintained at the same level used in photoacoustic experiments (≤ 15 μJ/pulse). The output from the nitrogen laser was passed through the optical trigger and shutter to the beam splitter; the shutter reduced the laser beam diameter to ~6.5 mm. The light passing through the beam splitter illuminated a 10 mm quartz cuvette (the sample cell), containing either the chemical actinometer or the $CpMn(CO)_3$ sample; this cell was housed within a temperature-controlled brass block (22.0 ± 0.1 °C) coupled to a NESLAB RTE-110 refrigerated bath. The reflected portion of the laser was directed through a 1 mm aperture (to maintain signal intensity on par with that of a photoacoustic experiment), then into a photoacoustic cell containing ferrocene in acetonitrile.

This cell served as a relative measurement of the incident laser energy, just as in the traditional PAC experiment.

Ferrioxalate was used as the actinometer, allowing calibration of the photoacoustic signal to the incident number of photons.[49-51] All solutions were freshly prepared, and all measurements were performed in a single experiment. A 0.006 M potassium ferrioxalate solution in 0.1 N H_2SO_4 was prepared under red photosafe light, and both it and aqueous 0.1% 1,10-phenanthroline were stored in the dark until needed. 2 mL of the ferrioxalate solution was irradiated with 50-400 laser shots ($<10^{-8}$ einsteins incident), after which a 1 mL aliquot was removed from the cuvette. The irradiated ferrioxalate aliquot was added to 0.5 mL of the phenanthroline solution and 1 mL of acetate buffer solution (600 mL 1 N CH_3COONa, 360 mL 1 N H_2SO_4 diluted to 1 L), then diluted to 5 mL with deionized water. These samples were stored for one hour at room temperature in the dark to allow the phenanthroline to complex with the photoreduced Fe^{2+}, after which their absorbance at 510 nm was determined. By using known quantum yields for the photoconversion of the actinometer,[49] the number of photons incident on the cell was correlated to the relative intensity as measured by the photoacoustic cell. 0.005 g $CpMn(CO)_3$ were added to 20 mL of solvent (0.0012 M) and 100 μL pyridine (0.061 M). 2 mL of this solution were irradiated for either 200 or 400 laser shots using hexane or hexadecane as the solvent. Formation of $CpMn(CO)_2$pyridine was monitored at 412 nm ($\varepsilon_{412} = 5100\ M^{-1}cm^{-1}$)[39] to determine the amount of $CpMn(CO)_3$ photolyzed. This portion of the experiment was performed under room lighting (Giordano and Wrighton have shown that in the presence of excess pyridine, $CpMn(CO)_2$pyridine is quantitatively regenerated making it effectively photostable)[39] and immediately measured via the spectrophotometer.

3.4 THEORY

The photoacoustic signal is defined as shown in Equation 3-3, where E_p is the incident photon energy, A is the absorbance of the sample, f_h^{obs} is the apparent fraction of absorbed energy released as heat, X_s is the thermal expansivity of the solvent, and κ' is an empirical instrument response factor.

$$S_{obs} = \kappa' E_p (1 - 10^{-A}) f_h^{obs} \mathrm{X}_s \tag{3-3}$$

The observed signal (S_{obs}) results from the volume change accompanying thermal deposition ($S_{thermal}$) to the solvent as well as any volume change due to chemical reaction (S_{volume}) (Equation 3-4). [2, 5, 9, 52-60]

$$S_{obs} = S_{thermal} + S_{volume} \tag{3-4}$$

Equation 3-3 can be restated as in Equation 3-5 to expressly delineate the volumetric contributions. In Equation 3-5, ΔV_{chem} is the volume change associated with the chemical reaction measured in the experiment.

$$S_{obs} = \kappa' E_p (1 - 10^{-A}) f_h \mathrm{X}_s + \kappa' E_p (1 - 10^{-A}) \frac{\Delta V_{chem}}{h\nu} \tag{3-5}$$

Equation 3-5 can be simplified into Equation 3-6.

$$f_h^{obs} h\nu \mathrm{X}_s = f_h h\nu \mathrm{X}_s + \Delta V_{chem} \tag{3-6}$$

By measuring f_h^{obs} for different X_s (Figure 3-3) over a homologous solvent series (we take linear alkanes to fill this requirement)[23] one can recover the actual fraction of energy converted to heat due to thermal deposition (f_h) and ΔV_{chem} of the system via Equation 3-6. Equations 3-7 and 3-8 allow the recovery of the reaction enthalpy and reaction volume (ΔH_{rxn} and ΔV_{rxn}) from the

measured photoacoustic results (f_h and ΔV_{chem}) by normalizing to the number of dissociative events (i.e., Φ_{diss}).

$$f_h = \frac{h\nu - \Delta H_{rxn}\Phi_{diss}}{h\nu} \tag{3-7}$$

$$\Delta V_{chem} = \Delta V_{rxn}\Phi_{diss} \tag{3-8}$$

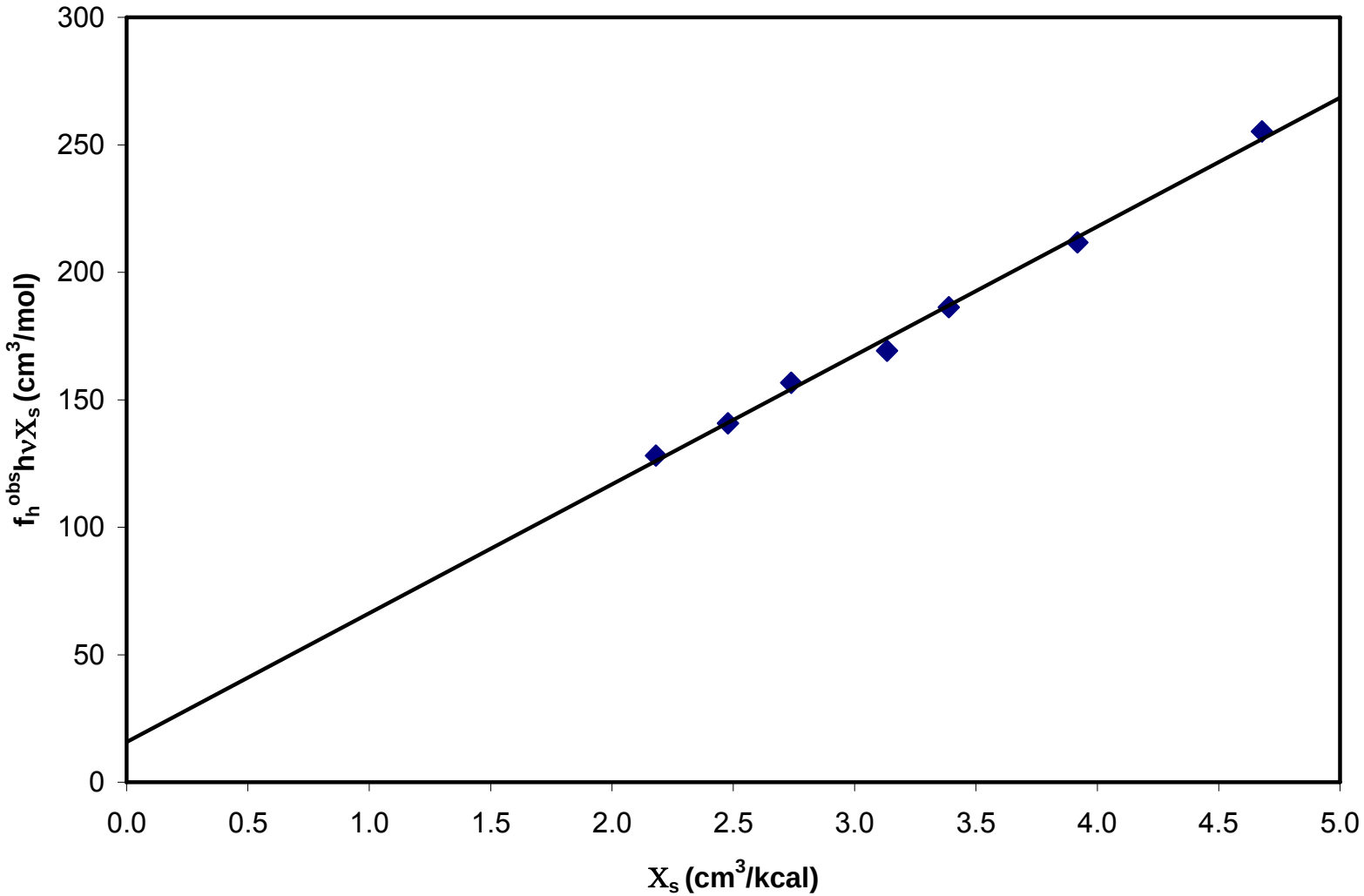

Figure 3-3 Plot of $f_h^{obs} h\nu X_s$ versus X_s (Equation 3-6) for the photoinitiated reaction of $CpMn(CO)_3$ in linear alkanes. The point size used is representative of the largest error in the entire series.

3.5 RESULTS AND DISCUSSION

3.5.1 Quantum Yield

Quantum yield measurements were performed in hexane and hexadecane. The ferrioxalate actinometer ($\Phi_{337.1\ nm}$ = 1.23, determined by interpolation of $\Phi_{334\ nm}$ = 1.23 and $\Phi_{341\ nm}$ = 1.22, no errors listed)[49] was used to calibrate the relative energy detector (E_p). No non-linear effects were observed in this experiment; this is unsurprising given that we are working at laser intensities similar to that of a PAC experiment. Knowledge of the amount of ferrioxalate photolysis product formed per unit of reflected signal allowed determination of the number of incident photons for any number of laser firings. ΔA_{412} was used to monitor the formation of $CpMn(CO)_2$(pyridine) (Equation 3-9).[39] With the knowledge of the ratio of incident photons vs. signal (E_p) found from the ferrioxalate actinometer, Φ_{diss} for $CpMn(CO)_2$–CO was determined twice for each solvent. All Φ_{diss} determinations accounted for the absorbance of $CpMn(CO)_3$ used, and the errors derive from the uncertainty of the slope of the detector calibration (n = 8).

$$CpMn(CO)_3 + \text{pyridine} \xrightarrow[\text{solvent}]{} CpMn(CO)_2(\text{pyridine}) + CO \qquad (3\text{-}9)$$

In hexane, we measured Φ_{diss} to be 0.570 ± 0.085 based on 200 laser pulses, and 0.572 ± 0.086 based on 400 laser pulses. In hexadecane, we measured Φ_{diss} to be 0.591 ± 0.088 based on 200 laser pulses, and 0.602 ± 0.090 based on 400 laser pulses. Evaluation of these results indicates that no significant difference in quantum yield exists for $CpMn(CO)_3$ between

these two solvents (0.571 ± 0.060 in hexane, 0.596 ± 0.063 in hexadecane). These data demonstrate that the quantum yield for photodissociation is constant over the solvent range used; as such, we find $\Phi_{diss} = 0.584 \pm 0.044$. This is comparable to the value of 0.65 ± 0.10 for $CpMn(CO)_3$ in octane at 313 nm reported by Giordano and Wrighton,[39] as well as 0.67 ± 0.04 in heptane at 337.1 nm measured by Pang *et al.*[61] In the analysis reported here, we use the average of these three known measurements ($\Phi_{diss} = 0.635 \pm 0.038$).

3.5.2 Photoacoustic Calorimetry

The results of 30 laser pulses were averaged for each photoacoustic wave (Figure 3-2), and were normalized for both sample absorbance ($1\text{-}10^{-A}$) and incident energy (E_p) (Eq. 3-2). Waveforms were visually inspected to ensure no change in cell alignment (i.e., a change in κ') had occurred and for indications of time-dependant behavior (none were found); such events are known to cause shifts in the observed waveform.[24, 62] A portion of the first negative excursion of each waveform (typically 1.51 μs in length) was integrated to give S_{obs} (Figure 3-2). In the determination of f_h^{obs}, the observed PAC waves from 7 different E_p intensities were analyzed according to Equation 3-3 (Figure 3-2 Inset). The plots of $S_{obs}/(1\text{-}T_s)$ vs. E_p demonstrated excellent linear form ($R^2 > 0.9980$). In each experiment (an experiment consists of a new set of solutions on a separate day) 2-3 sets of PAC waves were collected for the standards along with 2 sets for $CpMn(CO)_3$, yielding slopes equal to $f_h^{obs}\kappa'$ for the standards and $CpMn(CO)_3$. The slopes for the standards were then averaged to recover κ' (for standards, $f_h = 1.00$, $\Delta V = 0$, $\tau < 10$ ns, no change in S_{obs} over > 500 laser pulses), allowing the average $f_h^{obs}\kappa'$ of $CpMn(CO)_3$ to be used to determine f_h^{obs}. Multiple experiments were performed in each solvent; the

compiled results along with relevant solvent data are presented in Table 3-1. The f_h^{obs} were analyzed according to Equation 3-6 (Figure 3-3) to determine the f_h for Equation 3-1 to be 0.614 ± 0.013, which can be represented as ΔH_{obs} = 32.7 ± 0.7 kcal/mol ($\Delta H_{obs} = \Delta H_{rxn} \Phi_{diss}$), and ΔV_{chem} was found to be 11.0 ± 1.3 mL/mol.

The line obtained by fitting the data to Equation 3-3 and used to derive the values just noted has excellent linear form (R^2 = 0.9978); note that the size of the points in Figure 3-3 represents the largest error in the series. Using f_h and ΔV_{chem} along with Φ_{diss} = 0.635 and Equations 3-7 and 3-8, we determine ΔH_{rxn}{Eq. 3-1} = 51.6 ± 3.5 kcal/mol, and ΔV_{rxn}{Eq. 3-1} = 17.3 ± 2.3 mL/mol (errors include error propagated from both f_h and Φ_{diss}; the error in the quantum yield is often neglected in photoacoustic reports, and is the primary source of error in this measurement.)

We next examine the effect of ignoring ΔV_{rxn} for the photodissociation of $CpMn(CO)_3$, as well as the impact of the Φ_{diss} used. If, for the purposes of comparison, we reinterpret the value reported by Hester *et al.* in heptane [35] using the quantum yield found in this work, ΔH_{rxn} = 47.9 ± 2.2 kcal/mol. If we then treat our f_h^{obs} for heptane as f_h (i.e., neglect the contribution of ΔV_{rxn}), we would predict ΔH_{rxn} = 47.0 ± 2.8 kcal/mol. Our results are in excellent agreement with the reinterpreted findings of Hester *et al.* Separation of the ΔV_{rxn} contribution results in a 7% underestimation of ΔH_{rxn} when the reaction volume is neglected. This comparison serves to illustrate that though the data obtained in heptane in both Hester *et al.*'s study and this work are in superb agreement, and highlights that accounting for the volume of reaction is more important than previously appreciated (especially in order to ensure the most accurate determination of M-CO photodissociation reaction enthalpies.)

Table 3-1 Solvent Parameters and f_h^{obs} for $CpMn(CO)_3$ at 25°C

	n[a]	f_h^{obs}	st. dev.	α[b,c] (1/°C)	MW (g/mol)	C_p[b,d] [cal/(mol °C)]	ρ[b,d] (g/cm^3)	X_s[e] (cm^3/kcal)	f_h^{obs} $*h\nu$ $*X_s$	st. dev.	% Error
Pentane	3	0.6431	0.0104	0.00161	72.15	39.96	0.6214	4.678	255.2	4.1	1.6%
Hexane	3	0.6499	0.0214	0.001391	86.177	46.72	0.6548	3.918	216.0	7.1	3.3%
Heptane	4	0.6482	0.0026	0.001234	100.2	53.72	0.6795	3.388	186.2	0.8	0.4%
Octane	4	0.6410	0.0061	0.001164	114.23	60.74	0.6986	3.133	170.3	1.6	0.9%
Decane	3	0.6624	0.0058	0.001051	142.28	75.18	0.7264	2.738	156.6	4.0	2.6%
Dodecane	3	0.6696	0.0053	0.000974	170.34	89.86	0.7452	2.478	140.7	1.1	0.8%
Hexadecane	3	0.6715	0.0079	0.000889	226.45	119.85	0.77	2.182	124.2	1.5	1.2%

a. Number of experiments.

b. [63].

c. [64].

d. [65].

e. $X_s = \alpha\, MW / C_p\, \rho$

If ΔV_{rxn} were equal to zero, our data also would imply a solvent dependency for ΔH_{rxn}. For linear alkanes smaller than pentane, a solvent-interaction energy dependence has been observed in $W(CO)_5$,[66] though the trend appears to level off between pentane and hexane, consistent with our assumption that ΔH_{rxn} remains constant over our range of solvents.

We turn now to the determination and evaluation of the BDE{$Cp(CO)_2Mn–CO$}. The average bond dissociation energy of three Mn-CO bonds has been reported via bomb calorimetry,[67] but this value cannot be compared to the value derived here. Hester *et al.* have reported 7.8 kcal/mol as a lower-bound for the Mn-heptane interaction in the solution phase, and state that the actual interaction strength is probably not substantially different.[35] Using this estimation of the agostic interaction, we are able to derive the rigorous lower limit of the BDE{$Cp(CO)_2Mn–CO$} at 59.4 kcal/mol (Equation 3-10), and note that the actual value is not likely to be substantially different. To place this estimation into context, we point out three previous reports of BDE{$Cp(CO)_2Mn–CO$}. Li *et al.* reported BDE{$Cp(CO)_2Mn–CO$} to be 43.4 kcal/mol as determined by TPEPICO (gas-phase),[68] while theoretical calculations by Fan and Hall place BDE{$Cp(CO)_2Mn–CO$} at 52.7 kcal/mol.[69] The gas-phase BDE{$Cp(CO)_2Cr–CO$} of the isoelectronic species $CpCr(CO)_3^-$ was measured as 47.8 kcal/mol by Squires and Sunderlin by energy-resolved collision-induced dissociation.[70]

$$\mathrm{BDE}\{\mathrm{Cp(CO)_2Mn-CO}\} - \mathrm{BDE}\{\mathrm{Cp(CO)_2Mn-solvent}\} = \Delta H_{rxn}\{\mathrm{Eq.\ 3\text{-}1}\} \qquad (3\text{-}10)$$

The significant difference between threshold energy and PAC measurements prompted us to consider the validity of both our data, and the applicability of the TPEPICO-determined BDE's to metal carbonyls. As the PAC data are in complete agreement with previous studies (if ΔV_{rxn} were to be ignored) we focus here on the TPEPICO measurement. Few BDE measurements for $CpMn(CO)_3$ have been reported, and so we examine a number of BDE reports

for $Cr(CO)_6$. Four gas-phase measurements of the first carbonyl dissociation for $Cr(CO)_6$ have been made by methods other than TPEPICO: 37.0, 36.8, 38.7, and 34.8 kcal/mol (avg. 36.8 ± 1.6 kcal/mol).[71-74] Measurement by TPEPICO places the BDE{$(CO)_5Cr–CO$} to be 27.1 kcal/mol,[75] representing a 26% underestimation of the BDE of $Cr(CO)_6$. Similarly, TPEPICO measurement places the BDE{$Cp(CO)_2Mn–CO$} for $CpMn(CO)_3$ 29% below that determined by PAC. Despite the similarities in the magnitude of underestimation, we believe them to be coincidental (i.e. not a scaling factor). We note that the use of the TPEPICO-determined BDE{$Cp(CO)_2Mn–CO$}, 43.4 kcal/mol,[68] and our measured ΔH_{rxn}, 51.6 kcal/mol in Equation 3-10 would result in a negative agostic interaction (43.4 − 51.6 = -8.2 kcal/mol) which is not possible. In summary, we find that for $CpMn(CO)_3$, the PAC determination of the BDE is more consistent.

Both Gitterman *et al.* [76] and Farrell and Burkey [77] have used PAC to determine ΔH_{rxn} and ΔV_{rxn} for metal carbonyls undergoing a similar process to that described in Equation 3-1. For $Cr(CO)_6$ Farrell and Burkey found ΔH_{rxn} = 27.6 ± 0.8 kcal/mol and ΔV_{rxn} = 21 ± 2 mL/mol.[77] For $Mo(CO)_6$ in linear alkanes, Gitterman *et al.* found ΔH_{rxn} = 27.2 ± 1.9 kcal/mol and ΔV_{rxn} = 13 ± 6 mL/mol.[76] For $Cr(CO)_6$, Farrell and Burkey noted that ignoring the contribution of ΔV_{rxn} resulted in an error of 5-6 kcal/mol. For example, ignoring ΔV_{rxn}, their data would predict ΔH_{rxn} = 21.5 kcal/mol. Similarly, for $Mo(CO)_6$, Gitterman *et al.* showed that ignoring ΔV_{rxn} results in an error of 3.3 kcal/mol. These errors amount to 22% and 12% underestimates respectively. To our knowledge, there are only three other simple metal carbonyls studied by PAC. ΔV_{rxn} may contain useful information, but at this time the data set is too small to be extendable.

In conclusion, we find that the volume of reaction significantly contributes to the photoacoustic signal, and should be accounted for in this system. We also note that Farrell and Burkey and Jiao *et al.* [77, 78] have observed a similar effect with $Cr(CO)_6$ and $Mo(CO)_6$, implying that a full accounting of enthalpic and volumetric contributions generally is called for in metal carbonyls to ensure accurate thermochemical determinations. For $CpMn(CO)_3$ in linear alkanes, we determine $\Delta H_{obs} = 32.7 \pm 0.7$ kcal/mol and $\Delta V_{chem} = 11.0 \pm 1.3$ mL/mol for the equimolar reaction of photons and $CpMn(CO)_3$ molecules as in Equation 3-1, both of which are independent of the quantum yield of photodissociation. Knowledge of Φ_{diss} for $CpMn(CO)_3$ in linear alkanes (0.635) allows these values to be interpreted to yield the derived values $\Delta H_{rxn} = 51.6$ kcal/mol and $\Delta V_{rxn} = 17.3$ mL/mol. We find the lower limit of the BDE{$Cp(CO)_2Mn$-CO} to be 59.4 kcal/mol, and demonstrate the independence of Φ_{diss} over the range of linear alkanes examined.

3.6 ACKNOWLEDGMENTS

KWD acknowledges the National Science Foundation's GK-12 Grant # 0338135 to JJG for financial (stipend) support that enabled him to complete this project.

4.0 A PHOTOACOUSTIC CALORIMETRY STUDY OF CHROMIUM HEXACARBONYL: COMPARISON OF THE TWO METHODS OF PHOTOACOUSTICALLY DETERMINING THE REACTION VOLUME

4.1 ABSTRACT

Photoacoustic calorimetry (PAC) is a technique which can be used to determine the thermodynamics of reactive intermediates. Here, we report the examination of the photoinduced dissociation of $(CO)_5Cr$-CO and the subsequent stabilization of the coordinatively unsaturated intermediate by a solvent molecule. We have simultaneously determined the ΔH_{rxn} and ΔV_{rxn} for the photoinduced replacement of a carbonyl ligand with a solvent molecule for $Cr(CO)_6$ in linear alkanes. Based on these measurements, we determine the agnostic interaction between the metal center and the alkane. We examine the solvent dependence of the quantum yield of photodissociation over the alkane range examined (pentane to hexadecane), and find ΔH_{rxn} for the ligand exchange reaction $(CO)_5Cr$–CO to $(CO)_5Cr$–alkane to be 21.8 ± 1.0 kcal/mol and ΔV_{rxn} to be -19.1 ± 1.7 mL/mol. Based on these measurements, the agnostic interaction between the metal center and a coordinated alkane is 14.4 kcal/mol. In order to yield the best enthalpic determinations, we find that it is important to consider the volume change of the reaction. Failure to account for this ΔV_{rxn} results in significant overestimation in ΔH_{rxn}. Finally, the results

from two different methods of varying X_s to determine the contribution of ΔV_{rxn} to the photoacoustic signal are compared (linear alkanes and high-pressure PAC).

4.2 INTRODUCTION

In order to better understand reaction pathways, chemists have need of detailed information regarding the structures and energetics of each molecule along a reaction coordinate. Reactive intermediates formed from metal carbonyls are of particular interest due to their role in C-H bond activation; like most reactive intermediates, metal carbonyl intermediates are often difficult to study due both to their low concentrations and short lifetimes. In order to fully understand the process by which C-H bond activation occurs, reliable experimental values of M-CO bond dissociation energies are critical in locating the reactive intermediate relative to the starting materials on the reaction coordinate. A number of techniques exist for the measurement of the enthalpies of transient intermediates in the gas phase.[79] In the condensed phase, where the bulk of reactions occur, PAC has been established as a particularly sensitive technique for the determination of bond dissociation enthalpies.[9, 47, 54, 80, 81]

Photoacoustic calorimetry (PAC), also known as laser-induced optoacoustic calorimetry (LIOAC), has been used to determine the reaction enthalpies of photoinduced processes,[2-8] to determine the heats of formation of reactive intermediates,[9-11] to determine quantum yields,[12] and to determine the kinetics and lifetimes of transient intermediates.[13-16] When photoexcited, a molecule may undergo photochemistry, relax by photon emission, or release excess energy via heat deposition to the solvent. A change in the temperature of the solvent typically results in a change in volume, which propagates through the solvent as a pressure wave

and may be analyzed to recover enthalpic information. In many PAC studies carried out in organic solvents, the entire photoacoustic signal has been assigned to the thermal relaxation of the photoexcited species. A more rigorous approach considers that the overall photochemistry of the reaction (especially photofragmentation) may also contribute to the total volume change alongside that of the thermal relaxation (i.e., $\Delta V_{rxn} \neq 0$). Though the assumption of a negligible reaction volume may be warranted for some systems without net photochemistry, the magnitude (and even the sign) of this effect is difficult to predict, with positive,[76] negative,[77] and near zero [82] values reported.

In this study, we continue our ongoing examination of the importance of the volumetric contribution in obtaining accurate enthalpic determinations by photoacoustic calorimetry. To date, few examples of the contribution to photoacoustic signals resulting from a difference in solvated volumes between the reactants and products have been documented for systems in organic solvents. For aqueous systems, where the solvent expansivity (X_s) is often a factor of ten or more smaller than for organic solvents, consideration of non-thermal contributions to the photoacoustic signal typically are treated explicitly.[11, 17-20] Three experimental conditions can be varied to modify the solvent expansivity, which allows separation of the volumetric and enthalpic contributions of the photoacoustic signal: (i) temperature, if the solvent has significant expansivity dependence on temperature, as is the case for water;[11] (ii) pressure;[21] or (iii) solvent composition, so long as the change in solvents does not measurably affect the energetics of the system.[22] Organic solvents demonstrate only a small temperature dependence upon solvent expansivity, and as such X_s may only be controlled by varying pressure or using a series of homologous solvents in which relative solvation effects are constant, but for which the solvent expansivity varies.[23] To our knowledge, there has been no direct

comparison of these latter two methods. Farrell and Burkey have used high-pressure PAC to measure the same ligand exchange in heptane as we report here using the linear alkane method, allowing us to directly compare the results of both methodologies.[77] It is advantageous to discover whether or not the linear alkane method for PAC provides comparable results to the high-pressure method, as the linear alkane method of measuring ΔV_{rxn} is considerably easier to implement experimentally than the high-pressure approach.[21]

In PAC, knowledge of the quantum yields and kinetics are essential to allow interpretation of the photoacoustic results. As previously described, heat-release pathways for which $\tau < 10$ ns are not resolved on our photoacoustic calorimeter, and our time-resolved detection window extends to processes for which $\tau < 100$ μs.[15, 22] If any heat-release processes should occur within the time-resolvable window ($\tau = 10$ ns to 100 μs), these process produces a phase-shifted photoacoustic wave. The superposition of each of these component waves results in a waveform phase-shifted to a later time than the time-independent case; an expanded data treatment (called 'time-resolved' PAC) is available which allows simultaneous recovery of the energetics and kinetics of each component. If all detectable heat depositions occur faster than the resolution of the photoacoustic calorimeter, a simplified data treatment is possible (called 'too-fast' PAC). In the case of $Cr(CO)_6$, the photoinitiated reaction (Equation 4-1) occurs with $\tau = 93$ fs.[83] In the absence of nucleophiles, no other processes occur during the PAC-observable time window.[84] A summary of photoprocesses relevant on the PAC timeframe are shown in Figure 4-1.

$$Cr(CO)_6 + \text{alkane} \xrightarrow{h\nu} Cr(CO)_5(\text{alkane}) + CO + \text{heat} \qquad (4\text{-}1)$$

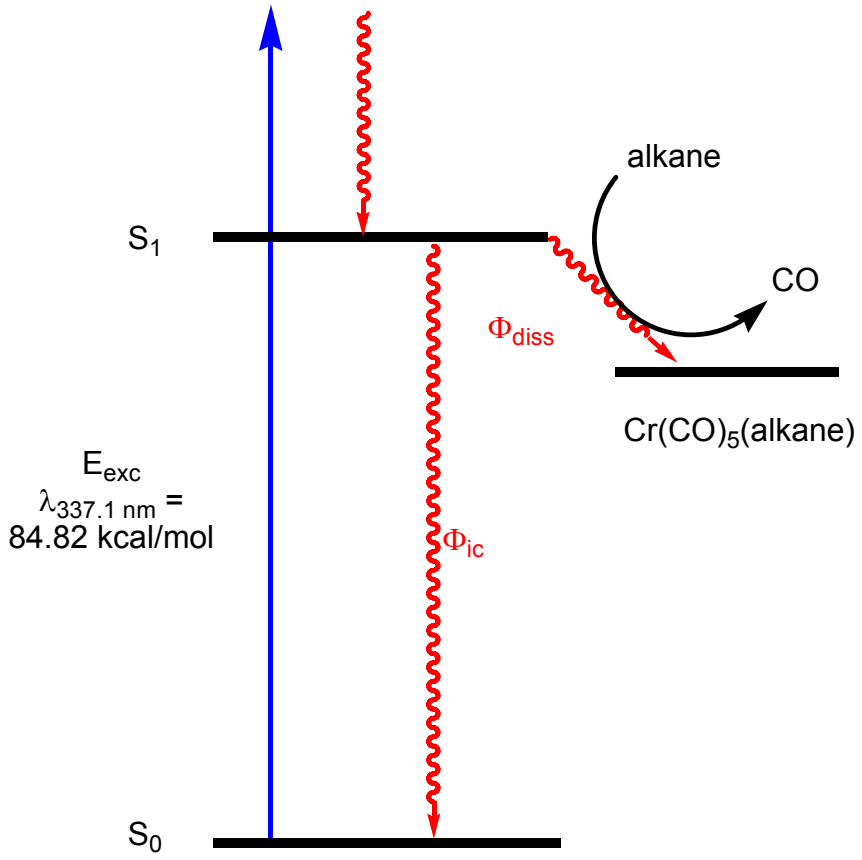

Figure 4-1 Jablonski diagram for the photoprocesses relevant to the PAC measurement of $Cr(CO)_6$.

4.3 EXPERIMENTAL

Chromium hexacarbonyl (99%) was obtained from Aldrich and was used as received. Ferrocene (98%) (FER), *o*-hydroxybenzophenone (oHBP), and tetraphenylethylene (98%) (TPE), used as

photoacoustic calibration compounds, were obtained from Aldrich and were purified by recrystallization prior to use. The alkane solvents were purchased from standard suppliers and were used as received. All photoacoustic experiments were carried out under ambient atmosphere and temperature (25-27°C) with samples having an optical density of $0.10 < A_{337.1\ nm} \leq 0.24$. Sample absorbances at 337.1 nm were obtained on a Hitachi U-2000 spectrophotometer with special care taken to ensure the most accurate value possible. The absorbances of the standard and sample we typically matched within 10% in a single experiment.

The photoacoustic calorimeter used has been previously described in detail and so only the key aspects are summarized here.[11] A nitrogen laser (Laser Photonics Model LN-1000, 337.1 nm, fwhm ~ 1 ns, 1.3 mJ/pulse, ~1 Hz free-run mode) was used for photoexcitation. A computer-controlled shutter ensured the sample was only irradiated during data acquisition. The excitation pulse passed through an optical trigger which established the timing for all data acquisition. The pulse then passed through a 1 mm circular aperture and a 10 mm quartz cuvette containing ferrocene/ethanol of varying optical density (used to attenuate the pulse strength). These two components work together to reduce the excitation pulse to $\leq 100\ \mu J$; the pulse excitation energies are kept low to minimize the occurrence of multiphoton events.

The laser pulse then passed through a beam splitter where ~30% of the pulse was reflected into a photoacoustic reference cell. The photoacoustic signal generated by this reference cell served as a relative measure of pulse energy. The reference cell contained ferrocene/ethanol which was slowly circulated from a ~500 mL reservoir. The remainder of the beam energy passed through the sample photoacoustic cell. The unabsorbed photons continued to a third photoacoustic cell (identical to the reference cell) which allowed the photoacoustic calorimeter to be used as a single-beam spectrophotometer for real-time absorbance quality

control measurements on the sample. All photoacoustic cells consisted of a 10 mm quartz cuvette spring-loaded against a custom-built piezoelectric microphone, described elsewhere.[45] A thin layer of vacuum grease between the cell wall and the transducer provided acoustic contact in all three cell positions. The photoacoustic standards used, FER,[46] oHBP,[85] and TPE,[48] are known to absorb 337.1 nm excitation without occurrences of photoinitiated reactions ($\Delta V_{rxn} = 0$) and to release all absorbed energy as heat faster ($\tau < 10$ ns) than the resolution of our transducer (i.e., $f_h = 1.00$). Representative sets of our data were subjected to time-resolved analysis to ensure no phase-shifts were present, and all data were visually inspected to further confirm the lack of time-resolved behavior.

Since the standards are known to have $\tau < 10$ ns, the photoacoustic wave acquired from a standard can be used both to verify that all thermal relaxations of the sample fit the 'too-fast' PAC requirements, and to determine the instrumental response factor (κ'). The time window during which the photoacoustic wave was recorded was chosen such that a portion of the data was collected before the laser fired (such data served as a baseline measurement) and both a positive and negative excursion were observed. The digitizer voltage offset was chosen to maximize the voltage range allotted to the negative excursion, which was selected as the signal of interest, resulting in 'clipping' of the positive excursion; in some experiments waves were collected without clipping to allow time-resolved analysis to inspect whether this expanded data treatment was required. A sharp negative peak is observed before the photoacoustic signal (*e.g.* Figure 4-2) as a result of electronic noise induced in the detection system by the firing of the laser; this provided a convenient method of distinguishing between baseline and signal data). During collection, our data acquisition program performed simple error-checking resulting in ~1% of the wave sets being rejected for various reasons. 30-50 collected waveforms were

averaged at each photolysis energy, and 6-8 photolysis energies (manipulated by varying the attenuation solution absorbance) were used for each compound in an experiment. Duplicate measurements were performed for both $Cr(CO)_6$ and the standards in each experiment, and to ensure accuracy of the determination of κ', we generally used two different reference compounds in a single experiment.

The theory of photoacoustic calorimetry has been previously derived, and will only be summarized here.[2, 5, 9, 52-59, 86] The photoacoustic signal is described by Equation 4-2.

$$S_{obs} = \kappa' E_p (1 - 10^{-A}) f_h^{obs} \mathrm{X}_s \tag{4-2}$$

The PAC signal is linearly related to the energy of the laser pulse ($E_p = n\, h\nu$), the fraction of the laser pulse absorbed by the analyte ($1 - 10^{-A}$), the apparent fraction of absorbed photon energy released as heat (f_h^{obs}), the expansivity of the solvent ($X_s = \alpha\, MW / C_p\, \rho$), and an instrumental response factor (κ'). α is the thermal expansion coefficient of the solvent, MW is the solvent molecular weight, C_p is the molar heat capacity of the solvent, and ρ is the solvent density. κ' is determined experimentally through photoacoustic measurement of a standard with a well known f_h^{obs}. Measurement of κ' for a standard allows determination of f_h^{obs} of the analyte in that particular solvent.

Equation 4-2 may be expanded to Equations 4-3 and 4-4, which account for change in volume over the reaction; here, the observed signal (S_{obs}) is separated into contributions

$$S_{obs} = S_{thermal} + S_{chem} \tag{4-3}$$

$$S_{obs} = \kappa' E_p (1 - 10^{-A}) f_h \mathrm{X}_s + \kappa' E_p (1 - 10^{-A}) \frac{\Delta V_{chem}}{h\nu} \tag{4-4}$$

originating from heat deposition ($S_{thermal}$) and the reaction (S_{chem}).[22] Equation 4-4 may be simplified into Equation 4-5, where ΔV_{chem} is the volume change associated with the chemical

reaction, and f_h is the actual fraction of absorbed energy released as heat. By measuring f_h^{obs} in a series of homologous solvents with different expansivities (i.e., varying X_s), Equation 4-5 allows recovery of the actual f_h, as well as ΔV_{chem}. In turn, these recovered values can be converted into the reaction enthalpy and volume (ΔH_{rxn} and ΔV_{rxn}) values through inclusion of the quantum yields into Equation 4-6 and 4-7. If the quantum yield of the sample varies over the solvent series, Equation 4-5 must be modified to account for the quantum yield for each solvent explicitly; the modified Equation is shown in Equation 4-8.

$$f_h^{obs} h\nu \mathrm{X}_s = f_h h\nu \mathrm{X}_s + \Delta V_{chem} \tag{4-5}$$

$$f_h = \frac{h\nu - \Delta H_{rxn}\Phi_{diss}}{h\nu} \tag{4-6}$$

$$\Delta V_{chem} = \Delta V_{rxn}\Phi_{diss} \tag{4-7}$$

$$\frac{\left(1 - f_h^{obs}\right)h\nu \mathrm{X}_s}{\Phi_{diss}} = \Delta H_{rxn}\mathrm{X}_s - \Delta V_{rxn} \tag{4-8}$$

4.4 RESULTS

Each photoacoustic wave was normalized for sample absorbance ($1 - 10^{-A}$) and incident energy (E_p) (Equation 4-2). All waveforms were analyzed for phase shifts and changes in wave shape, either of which would be indicative of a change in cell alignment (i.e. κ') or time-dependent behavior.[24, 62] The first negative excursion of the photoacoustic wave was integrated (typically 1.5 μs) to yield S_{obs} (Figure 4-2). S_{obs} was collected for 6-8 E_p intensities and analyzed by Equation 4-2 (Figure 4-2). All plots of $S_{obs}/(1-T_s)$ vs. E_p demonstrated excellent linear form,

typically with $R^2 > 0.9990$. In a single experiment, at least two $f_h^{obs}\kappa'$ were determined for $Cr(CO)_6$; likewise, at least 2 $f_h^{obs}\kappa'$ were determined for the standards; $f_h^{obs}\kappa'$ of standards were averaged and κ' determined. The f_h^{obs} determined for $Cr(CO)_6$ were averaged to give its final value. In each experiment, photoacoustic waves were also collected for neat solvent to confirm the absence of a solvent photoacoustic response. Since the standard is known to have $f_h = f_h^{obs} = 1.00$, its entire slope ($f_h\kappa'$) may be taken as κ'. The $f_h^{obs}\kappa'$ measured for $Cr(CO)_6$ were then averaged, allowing f_h^{obs} to be determined for that experiment as the ratio of the slopes. The compiled results are shown in Table 4-1.

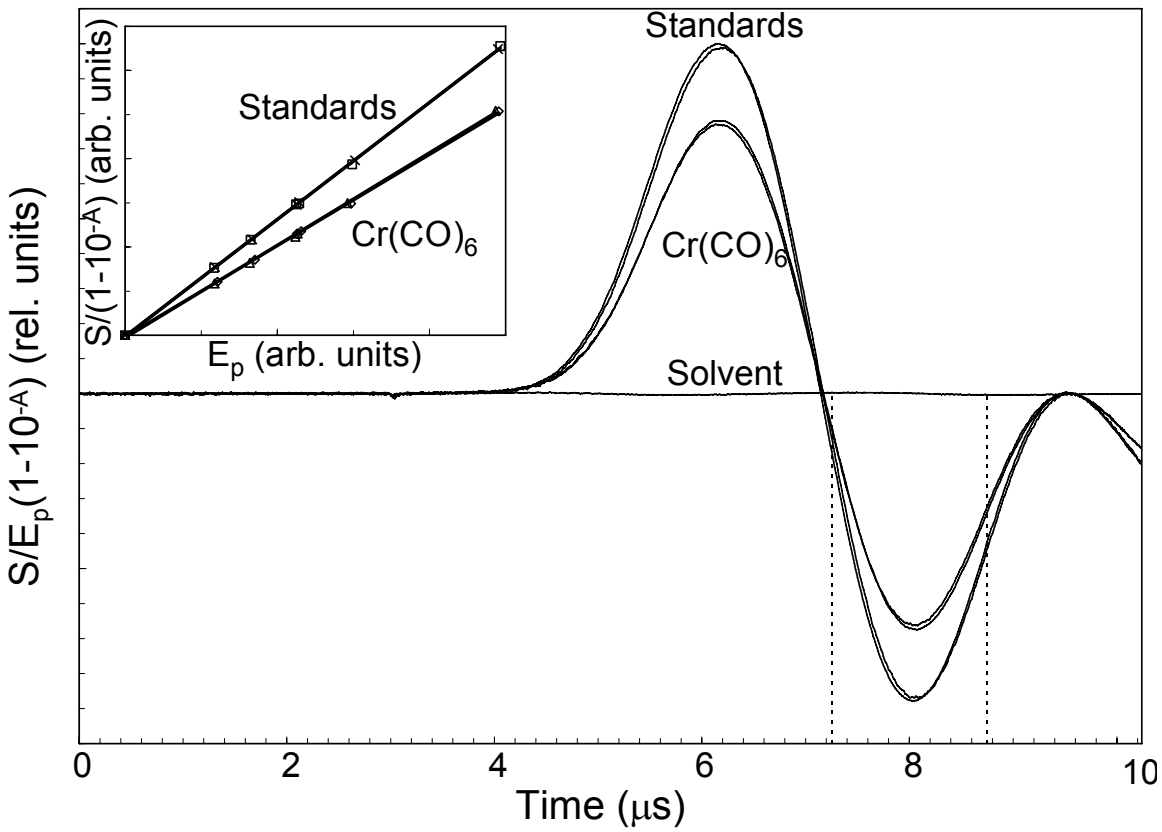

Figure 4-2 PAC signals for two $Cr(CO)_6$ measurements and two standards plotted according to Eq. 4-2. Shown are two waves from standards, two from $Cr(CO)_6$, and one from pure solvent. The small negative spike observed at 3 μs corresponds to the firing of the laser. Data before this point serves as the baseline for wave integration. Integration limits used are shown by dashed lines. Inset: Averaged waves (50 laser shots) from a typical PAC experiment at a single laser energy (E_p).

Table 4-1 Solvent Parameters and f_h^{obs} for $Cr(CO)_6$ at 25°C

Solvent	n^a	f_h^{obs}	$\alpha^{b,c}$ (1/°C)	**MW** (g/mol)	$C_p^{b,d}$ [cal/(mol*°C)]	$\rho^{b,d}$ (g/cm^3)	X_s (g/cm^3)	Φ_{diss}^{e}	$[(1-f_h^{obs})\, h\, \nu X_s] / \Phi_{diss}$	**% Error**
Pentane	3	0.7782 ± 0.0139	0.001610	72.150	39.96	0.62139	4.678	0.722	121.9 ± 2.2	1.8%
Heptane	2	0.7785 ± 0.0063	0.001234[f]	100.203	53.72	0.67946	3.388	0.702	90.7 ± 0.7	0.8%
Octane	1	0.7822 ± 0.0104	0.001164	114.230	60.74	0.69862	3.133	0.676	85.7 ± 1.1	1.3%
Nonane	3	0.7775 ± 0.0096	0.001085[f]	128.257	68.01	0.71375	2.867	0.644	84.1 ± 1.0	1.2%
Decane	2	0.7931 ± 0.0033	0.001051	142.284	75.18	0.72635	2.738	0.612	78.6 ± 0.3	0.4%
Hexadecane	2	0.8342 ± 0.0046	0.000889[f]	226.450	119.85	0.76996	2.182	0.458	66.9 ± 0.4	0.5%

a. number of experiments
b. [63]
c. [64]
d. [65]
e. Calculated via best-fit quadratic fitting of values from [87-90]; see Section 4.5.1
f. at 20°C

4.5 DISCUSSION

4.5.1 Quantum Yield

The quantum yield of photodissociation for $Cr(CO)_6$ demonstrates a solvent dependence, as is evident from measurements in linear alkanes performed by Wieland and van Eldik at 313 nm [91] and Nasielski and Colas at 292 nm [87] (Figure 4-3). The quantum yield of $Cr(CO)_6$ in cyclohexane has been reported as 0.67 ± 0.01 at 337.1 nm,[92] 0.67 ± 0.02 at 313 nm,[93] and 0.67 ± 0.04 at 292 nm,[87] demonstrating that Φ_{diss} of $Cr(CO)_6$ is wavelength independent over this range for a common solvent. Therefore, we consider the quantum yields measured at 292 and 313 nm as applicable to 337.1 nm.

The Booth-Noyes model of cage escape predicts that quantum yields may be determined by a quadratic fit of the reciprocal of the cage escape fraction ($1 - \Phi_{diss}$) and fluidity (the reciprocal of the viscosity, $1/\eta$);[88, 89, 94] the relationship between viscosity and cage escape has been plotted in Figure 4-3, along with that of di-*tert*-butyl peroxide (for comparison).[94-96] The quadratic fit of the $Cr(CO)_6$/linear alkane data in Figure 4-3 is predictive ($R^2 = 0.9309$); this fit has been used to calculate smoothed Φ_{diss} for $Cr(CO)_6$, and is the source of the quantum yields listed in Table 4-1 and our analysis of the photoacoustic data. Di-*tert*-butyl peroxide demonstrates a high rate of cage escape at high fluidities (i.e. Φ_{diss} is high for low viscosities). We note a similar though less emphatic trend for the alkanes heptane and larger; cage escape appears to reach a maximum in heptane, and remains constant for more fluid solvents.

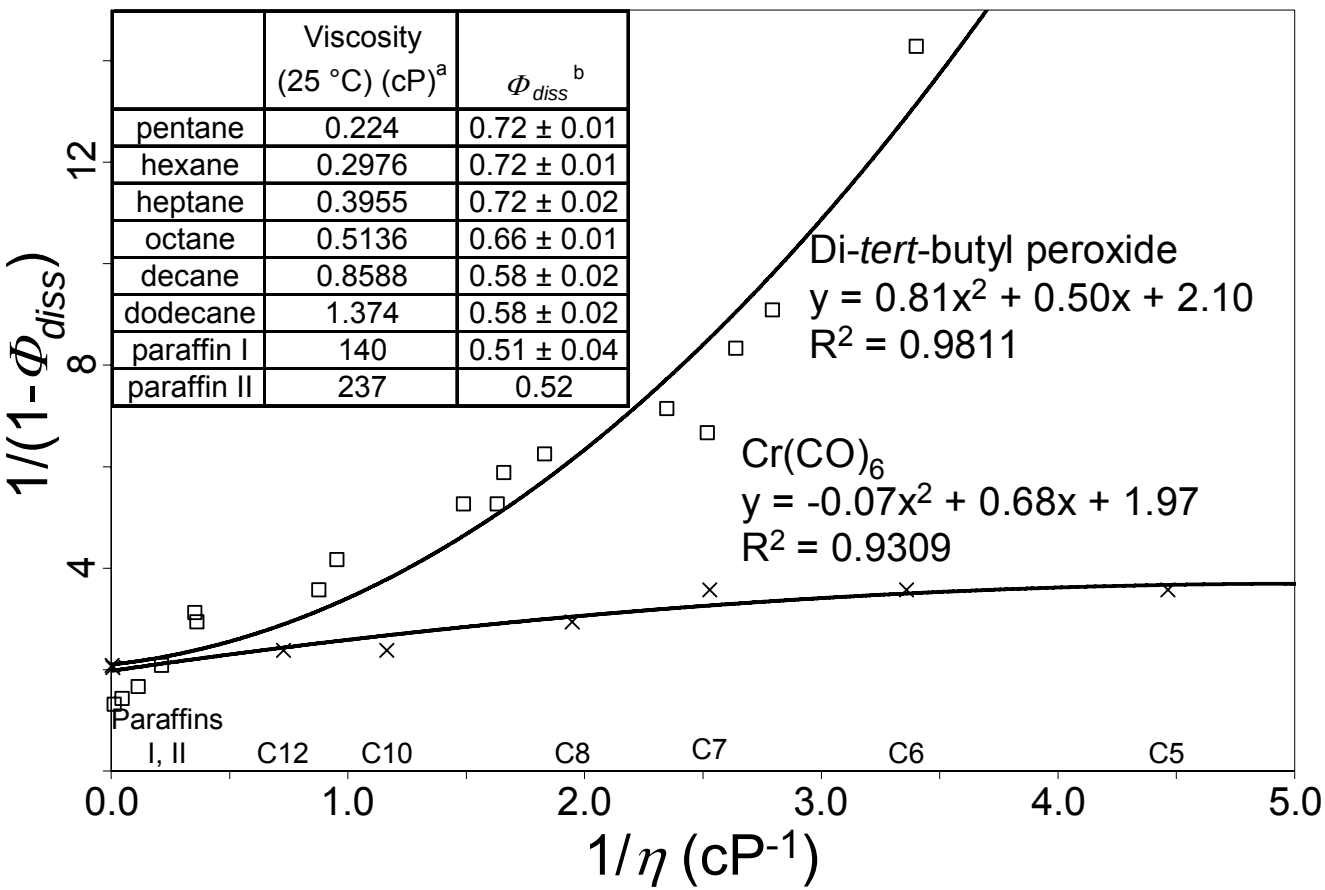

	Viscosity (25 °C) (cP)[a]	Φ_{diss} [b]
pentane	0.224	0.72 ± 0.01
hexane	0.2976	0.72 ± 0.01
heptane	0.3955	0.72 ± 0.02
octane	0.5136	0.66 ± 0.01
decane	0.8588	0.58 ± 0.02
dodecane	1.374	0.58 ± 0.02
paraffin I	140	0.51 ± 0.04
paraffin II	237	0.52

Figure 4-3 Plot of 1 / (1 - Φ_{diss}) versus $1/\eta$ [88, 89] for $Cr(CO)_6$ (♦) [87, 90] and di-*tert*-butyl peroxide (■) [94, 95]. Inset: Viscosities and quantum yields of $Cr(CO)_6$.

a. [87, 96, 97]

b. [87-90]

4.5.2 Photoacoustic Calorimetry

In Figure 4-4, we show the data listed in Table 4-1Table 4-1, plotted in the form of Equation 4-8. The plot in Fig. 4 has en excellent linear fit ($R^2 = 0.9912$). ΔH_{rxn} and ΔV_{rxn} may be determined directly from the slope and y-intercept of this plot; we find $\Delta H_{rxn} = 21.8 \pm 1.0$ kcal/mol and $\Delta V_{rxn} = -19.1 \pm 1.7$ mL/mol. As a comparison, if we were to analyze our PAC data by assuming $\Delta V_{rxn} = 0$, we would overestimate ΔH_{rxn} by at least 4.3 kcal/mol (20%) in pentane and as much as 8.9 kcal/mol (41%) in hexadecane. Clearly, in the case of $Cr(CO)_6$ it is important to explicitly consider ΔV_{rxn} to ensure the derivation of high-quality thermochemical determinations.

The magnitude of ΔV_{rxn} and the importance of explicitly including this term is comparable to the few similar measurements for metal carbonyls. For $Mo(CO)_6$ in linear alkanes, Gitterman *et al.* found $\Delta H_{rxn} = 27.2 \pm 1.9$ kcal/mol and $\Delta V_{rxn} = 13 \pm 6$ mL/mol, and that neglecting ΔV_{rxn} results in an underestimate of 3.1 kcal/mol (11%).[76] In a recent paper, we reported ΔH_{rxn} for $CpMn(CO)_3$ to be 51.6 ± 3.5 kcal/mol and $\Delta V_{rxn} = 17.3 \pm 2.3$ mL/mol, and that neglecting ΔV_{rxn} results in an underestimate of 3.7 kcal/mol (7%).[98] To our knowledge, these are the only three metal carbonyls which have been likewise investigated. Because the volume changes for reactive intermediates have remained largely unexplored, we are limited in our ability to comment on the magnitude and sign of ΔV_{rxn}.

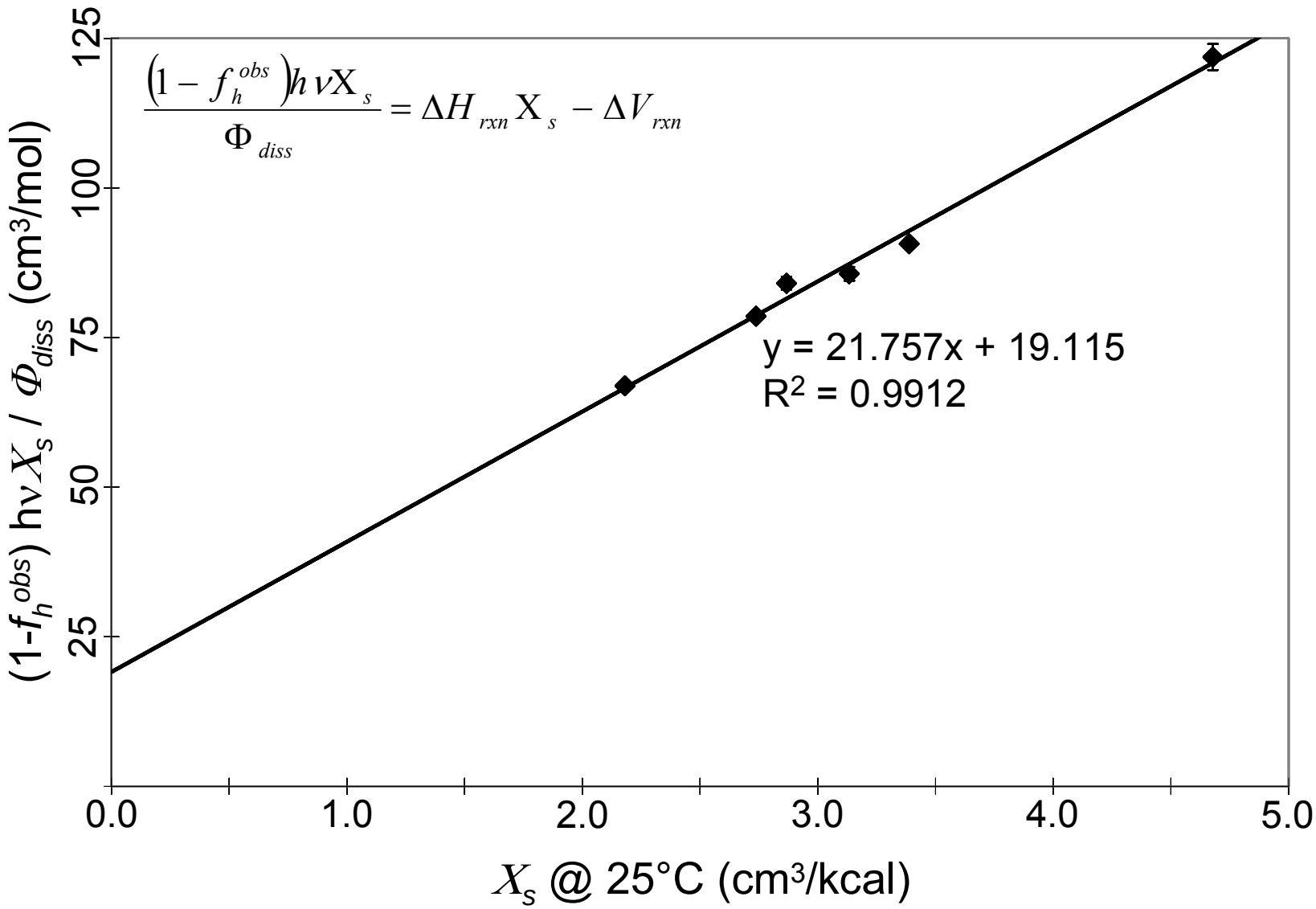

Figure 4-4 Plot of $[(1-f_h^{obs})h\nu X_s]/\Phi_{diss}$ versus X_s (Equation 4-8) for the photoinduced reaction of $Cr(CO)_6$ in linear alkanes.

4.5.3 Comparison of Linear Alkane and High-pressure PAC

To date, no studies have compared the results for ΔH_{rxn} and ΔV_{rxn} measured by the linear alkane and high-pressure methods. High-pressure PAC measurements of have been reported by Burkey *et al.* for $Cr(CO)_6$, allowing us to consider the agreement between the two approaches.[77] As the ΔH_{rxn} measured by the linear alkane (ΔH_{rxn} = 21.8 ± 1.0 kcal/mol) and high-pressure methods (ΔH_{rxn} = 27.6 ± 0.8 kcal/mol) are in poor agreement, we now compare data from each study taken at a single solvent expansivity (i.e. same pressure or same solvent) to another PAC study under the same conditions to probe whether the difference lies in the underlying data or the approach. For the sake of comparison, we have reinterpreted our measurement in heptane without accounting for ΔV_{rxn}; Farrell and Burkey also reported single-pressure measurements in heptane.[77] Both our measurements and the Farrell and Burkey measurements can be compared to previous PAC studies that did not account for ΔV_{rxn}.[99, 100] This allows us to comment on the differences between the results that account for ΔV_{rxn}. These data have been compiled in Table 4-2. If we assign the entire PAC signal to ΔH_{rxn}, our results are in excellent agreement (within 1 s.d.) with previous reports which did not account for ΔV_{rxn}, indicating that our current study differs from previous results not in the raw result, but only in our application of a more thorough treatment.

Table 4-2 Comparison of PAC measurements of ΔH_{rxn} and ΔV_{rxn} at both ambient and high-pressures. The value measured by Farrell and Burkey has been estimated from their published plots.[77]

		Conditions	ΔH_{rxn} (kcal/mol)	ΔV_{rxn} (mL/mol)
Ambient Pressure	This Work	Linear Alkanes	21.8 ± 1.0	-19.1 ± 1.7
	This Work	Heptane	26.8 ± 0.2	--
	[99]	Heptane	25.9 ± 0.8 (using Φ_{diss} = 0.702)	--
High Pressure	[77]	1.4 - 103 MPa	27.6 ± 0.8	-20.8 ± 1.9
	[77]	1.4 MPa	33.7	--
	[77]	13 MPa	34.3	--
	[100]	13 MPa	25.1 ± 1.0	--

We turn now to the high-pressure data. Walsh *et al.* [100] measured ΔH_{rxn} at 13 MPa without accounting for ΔV_{rxn} allowing us to compare the result of Farrell and Burkey [77] against another high-pressure measurement. Unfortunately, Farrell and Burkey did not include explicit values for f_h^{obs}, the quantum yields used, and other important parameters; we have estimated the ΔH_{rxn} that would be measured when neglecting ΔV_{rxn} from their figures, and interpolated a result for 13 MPa (values shown in Table 4-2).

The result from Walsh *et al.* is 2 kcal/mol lower than measured by PAC at ambient pressure; we would indeed expect these results to differ due to the difference in solvent expansivity at this higher pressure. However, there is a troubling disagreement between the estimated result of Farrell and Burkey and the measurement of Walsh *et al.* at 13 MPa (the Farrell and Burkey data yields ΔH_{rxn} as 9 kcal/mol higher than Walsh *et al.*'s measurement).

Unfortunately, without more detailed information about the data treatment in Farrell and Burkey's paper, we cannot determine whether this difference is attributable to the underlying PAC data or differences in values used in the analysis (X_s, α, *etc.*). A separate paper by Daffron *et al.* does note that use of their high-pressure system gave anomalous results for the analysis of diphenylcyclopropenone (DPCP) compared to values determined by linear alkane PAC and bomb calorimetry.[21] Clearly, caution should be used when comparing ambient and high-pressure studies of enthalpy.

4.5.4 The Cr-alkane Agostic Bond

The gas-phase bond dissociation energy of $Cr(CO)_5$-CO has been determined to be 36.2 kcal/mol (average of references [72-74]). This allows us to determine the agostic interaction between Cr and the alkane (Equation 4-9) to be 14.4 kcal/mol. This agostic interaction is of comparable strength to other agostic interactions reported in the literature (Table 4-3).

$$\text{BDE}\{(CO)_5\text{Cr–CO}\} - \text{BDE}\{(CO)_5\text{Cr–solvent}\} = \Delta H_{rxn}\{\text{Eq. 4-1}\} \quad (4\text{-}9)$$

Table 4-3 Examples of Agostic Interactions

Compound	Agostic Interaction	Methodology	Reference
$Et_2B(pz)_2]Mo(CO)_2(\eta^3\text{-allyl})$	17-20 kcal/mol	H-NMR	[101]
$Mo(CO)_5$(alkane)	13.4 kcal/mol	PAC, laser pyrolysis	[76]
$W(CO)_5(CH_3CH_2F)$	12 kcal/mol	time-resolved IR	[66]
$\eta^5\text{-}(C_5H_5)Mn(CO)_3$	7.8 kcal/mol	time-resolved IR	[35]

4.6 CONCLUSION

We have found that for $Cr(CO)_6$ it is important to account for ΔV_{rxn} in order to determine high-quality thermochemical data. This appears to be generally true of metal carbonyls in alkane solutions based on our results for $Cr(CO)_6$ and $CpMn(CO)_3$,[58] and this conclusion is further supported by Gitterman *et al.* for $Mo(CO)_6$.[21] We report $\Delta H_{rxn} = 21.8 \pm 1.0$ kcal/mol and $\Delta V_{rxn} = -19.1 \pm 1.7$ mL/mol, and by comparison to a gas-phase bond dissociation found in the literature have determined the agostic interaction between the metal center and the alkane to be 14.4 kcal/mol. We also find cause for caution when comparing ΔH_{rxn} and ΔV_{rxn} determined by the linear alkane and high-pressure PAC methods.

5.0 THE PHOTOACOUSTIC MEASUREMENT OF THE INTERMEDIATE OF THE MIGRATORY INSERTION REACTION

5.1 INTRODUCTION

Alkyl group migration reactions are widely used in organometallic chemistry; a textbook example of this class of reaction is the migratory insertion of a carbonyl into the M-CH_3 bond in $Mn(CO)_5CH_3$. Though this reaction has been known for over 50 years,[102] the structural form of the intermediate is still a matter of debate.

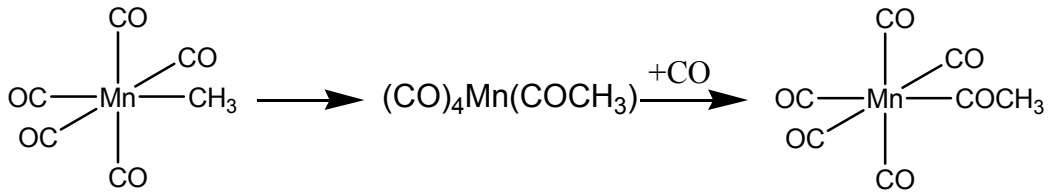

(M) (I) (A) (5-1)

The basic reaction is well understood, and proceeds as shown in Equation 5-1.[103-114] In this enthalpically-favorable reaction, a carbonyl group cis to the methyl group of the manganese alkyl (M) is inserted into the metal-alkyl bond. The coordinately unsaturated metal-acetyl intermediate (I) then reacts with a carbon monoxide molecule in solution, yielding the acetyl manganese form (A). Photoexcitation of (A) follows the pathway shown in Equation 5-2; Boese *et al.* have determined that the form of (I) is the same for either the photoinitiated

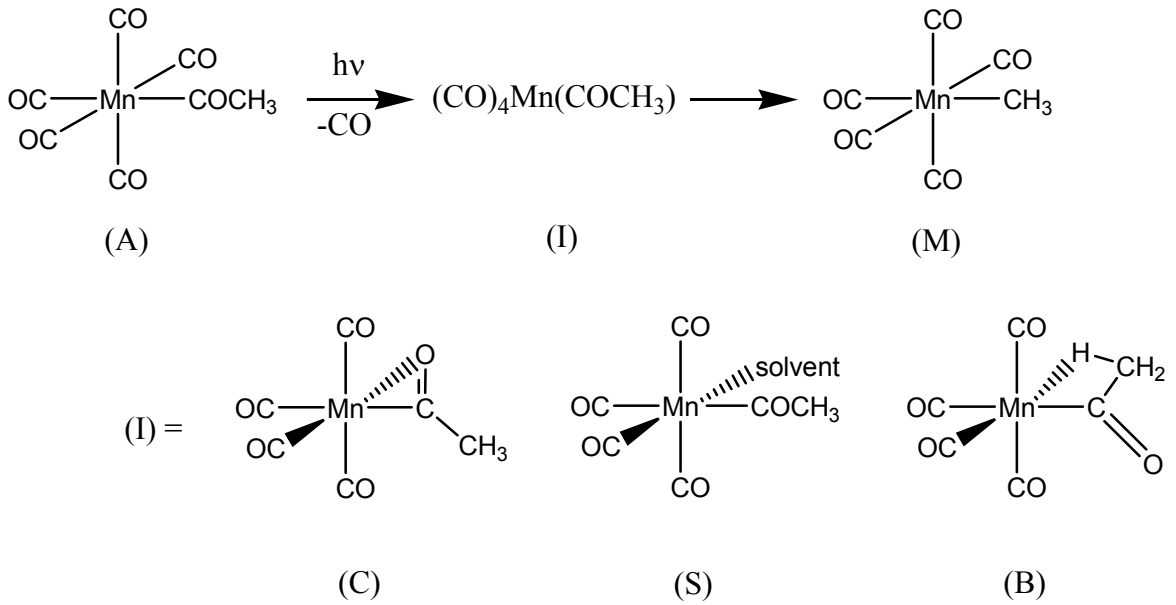

(5-2)

reaction (A → I) or the thermal reaction (M → I).[105] There are three likely candidates for the structure of (I), each of which are shown in Equation 5-2.

Form (C) is an η^2-acyl complex, form (S) represents the 'solvento' complex (i.e. an externally agostically stabilized form), and (B) is an internally agostically-stabilized form. Various studies have uncovered evidence for the presence of at least one of these three intermediates along the reaction coordinate. Forms (B) and (C) are thought to be the most likely intermediates in Equation 5-1 for non-polar solvents. Overall however, there remains little consensus as to the actual reaction pathway (*e.g.* references [103, 104, 106]).

Previous experimental attempts to identify (I) have relied upon indirect energetic measurements, which were determined through flash-photolysis kinetic measurements (*e.g.* time-resolved IR spectroscopy). In these experiments, $(CH_3OC)Mn(CO)_5$ was photoexcited, and spectral changes were monitored to determine the reaction kinetics of the intermediate. Since the transient intermediate is only present in small concentrations, and the intermediate is in a solution of (A), it is challenging to measure the small ΔA's accurately, limiting the quality of these measurements and leading to differing interpretations of the kinetic data.

High level theoretical calculations (B3P86/sb, B3P86/lb, B3LYP/lb) have been performed by Derecskei-Kovacs and Marynick,[104] offering optimized geometries and an estimation of the energies for each of the intermediates, transition states, and activation energies proposed. Their results suggest the existence of (at least) two possible reaction channels. However, due to uncertainties as to whether their computational models accurately represent the energetics of the solvated transition states and intermediates, it is difficult to ascertain if these proposed pathways have physical significance.

Clearly, more direct evidence would be desirable. Photoacoustic calorimetry may be able to shed some light upon the reaction pathway through measurement of volume change resulting from the reaction. If photoacoustic measurements are taken in a series of linear alkanes, both the enthalpy and volume changes of the reaction may be measured directly, and ΔV_{rxn} may provide some insight into the structure of the intermediate, based on the differences in solvent-excluded volumes for each structure. This would be an exciting development and would provide a new point-of-entry in determining the nature of short-lived intermediates. Kinetic measurements have shown that complete photoconversion from (A) to (I) is complete in less than 150 ns, [105] while the intermediate (I) is long-lived ($\tau > \mu s$) even under 1 atm of CO.[108] These kinetics are fully compatible with a straightforward PAC measurement approach.

The ΔV_{rxn} measured by PAC is known to be physically meaningful, but to date these measurements have only been used in photoacoustic calorimetry as a correction factor that must be accounted for to give high-quality reaction enthalpies. In this chapter, we measure ΔH_{rxn}, ΔV_{rxn}, and attempt to correlate ΔV_{rxn} to differences in computed molecular volumes for (A) and (B), (C), and (S).

5.2 EXPERIMENTAL

5.2.1 Synthesis of $(CH_3OC)Mn(CO)_5$

The preparation of $(CH_3OC)Mn(CO)_5$ is a modification of the synthesis described in [115]. $Mn_2(CO)_{10}$ (Alfa Aesar) was purified by vacuum sublimation at 50°C under 0.3 mmHg, and stored under argon below 0°C until use. Acetyl chloride (Acros Organics) was refluxed under argon for 3 hours in the presence of calcium chloride to collect dry CH_3COCl and minimize the presence of acetic acid; the distillate was collected and stored under argon in a glass-stoppered flask. Deoxygenated THF (under nitrogen gas) was collected in a flame-dried flask from the glove box still of Dr. Tara Meyer (University of Pittsburgh). A sealed but pre-scored ampoule of 20% Na/Hg amalgam beads (Strem) was placed into a sealed glove bag with all compounds and glassware to be used in this synthesis. The glove bag contained an open dish of Dryerite, and was serially filled and purged with nitrogen gas, followed by multiple fill/purge cycles of argon gas. The glove bag was maintained under positive pressure by a continual influx of argon gas, which was vented through an oil-filled bubbler. Finally, the sealed glove bag was allowed to sit overnight, ensuring a dry and oxygen-free environment.

A compact, single arm balance inside the glove bag was used to obtain masses of the reactants this synthesis. 0.3 g of $Mn_2(CO)_{10}$ was dissolved in 6 mL of THF. This solution was transferred into a round-bottom flask containing 10 g of Na/Hg amalgam beads; the solution and Na/Hg beads were magnetically stirred for 75 minutes at room temperature. A dark-green solution of $NaMn(CO)_5$ in THF was generated; the solution was transferred into another flask. The Na/Hg beads were washed with 2 aliquots of 5 mL of THF. The $NaMn(CO)_5$ solution was stoppered, wrapped in the wall of the glove bag, and a rubber band was placed on the outside of

the glove bag. A dry ice/acetone bath (-78°C) was prepared outside the glove bag, and the flask wrapped in the glove bag 'pocket' was immersed in the bath. Inside the glove bag, the stopper was removed, and 0.2 mL of acetyl chloride was added to the cooled solution; the stopper was replaced, and the solution was maintained at -78°C for 1 hour. The solution was then removed from the glove bag, and the solvent was removed by rotary evaporation at room temperature under a pressure of 5 torr. 10 mL of hexane were added to the solid, and the mixture was stirred at room temperature for 30 minutes. The solution was filtered, and the filtrate was maintained in a -20°C cold room for 16 hours. Pale yellow crystals were collected, later demonstrated to be $(CH_3OC)Mn(CO)_5$ (white) with a significant impurity of $Mn_2(CO)_{10}$ (yellow). The remaining solution was serially evaporated to 50% of its remaining volume and cooled, resulting in additional batches of crystals; each yield of crystals was each kept separate. The stoppered tubes of crystals were then maintained in the laboratory freezer. During this time, long white crystals developed on the sides of the test tube (presumably by sublimation/deposition); these crystals were analyzed on a Micromass Autospec using an EI source, and determined to be pure crystals of $(CH_3OC)Mn(CO)_5$ (Figure 5-1). The peaks of this mass spectrum match previous reports for this complex.[110] Crystals formed by this sublimation process were used for all PAC experiments.

.

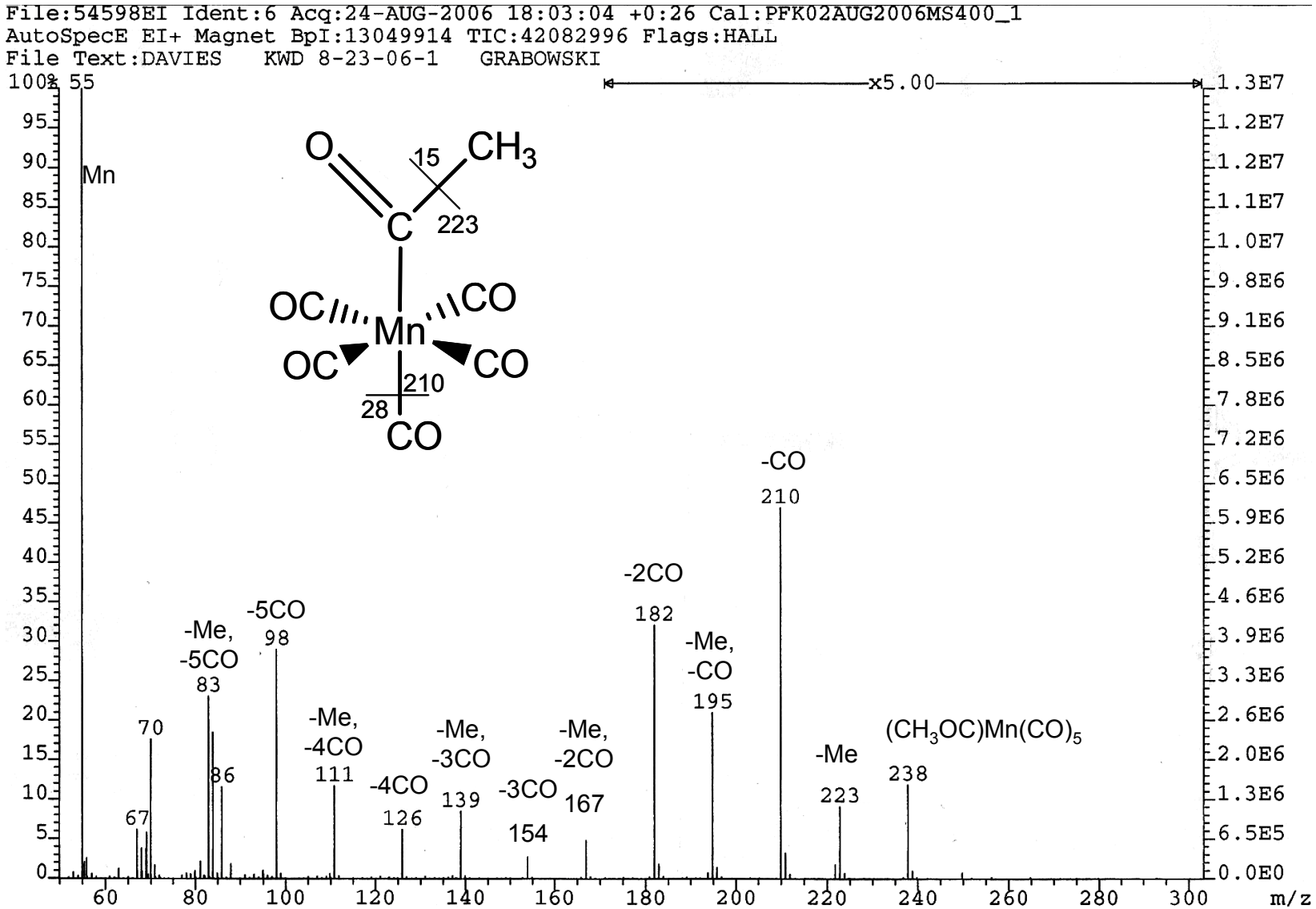

Figure 5-1 Mass spectrum of $(CH_3OC)Mn(CO)_5$

5.2.2 Photoacoustic Calorimetry

All PAC experiments were conducted under similar conditions to those reported in previous chapters, and only a brief description of the specific photoacoustic conditions is given here. The linear alkane method for determining ΔV_{rxn} was used, with a solvent series ranging from pentane to hexadecane. Ferrocene and tetraphenylethylene were used as photoacoustic standards. Sample and standard absorbances were measured on either a Hitachi U-2000 or a Varian/Cary 5000. These solutions were prepared with absorbances between 0.093 - 0.157, and were typically matched within 3% in a single experiment. During these experiments, the absorbance of the $(CH_3OC)Mn(CO)_5$ solution was seen to change over time; to ensure accuracy of both the absorbance and photoacoustic measurements, all solutions of $(CH_3OC)Mn(CO)_5$ were freshly prepared and care was taken to ensure all measurements were complete within 20 minutes. All PAC experiments showed a change of less than 0.003 absorbance units (i.e. <0.3%) at 337.1 nm. Initial PAC experiments were performed both with and without argon-purging in order to determine whether dissolved gasses (e.g. O_2) affected the measured f_h^{obs}; no differences were observed in these experiments, and all subsequent PAC experiments were done without argon flow to minimize changes in sample absorbance due to evaporation.

5.3 RESULTS

Each photoacoustic wave was normalized for the absorbance of the sample ($1 - 10^{-A}$) and the average incident laser energy of the collected laser pulses (E_p). The photoacoustic waveforms

acquired for $(CH_3OC)Mn(CO)_5$ were visually compared to those of the standards to ascertain if any processes deposited heat in the time-resolved time domain; no time-dependant behavior was observed. The photoacoustic waves were also analyzed to ensure no changes in the peak shape had occured; this would indicate that the geometry of our instrument had changed during the experiment (i.e. that the experimentally-measured κ had changed). 1.5 μs of the negative excursion of the photoacoustic wave were integrated, and this measurement was used as the photoacoustic signal, S_{obs}. The laser intensity was attenuated by changing the concentration of an absorptive solution (typically ferrocene in acetonitrile) in the laser beam path; 7 different attenuations were used, allowing us to measure S_{obs} for various E_p. These data were plotted using Equation 2-5 for each experiment; all plots of $S_{obs} / (1 - 10^{-A})$ vs. E_p demonstrated excellent linear form (typically $R^2 > 0.9980$). Figure 5-2 shows two waves from standards (Fer and TPE) and two waves for $(CH_3OC)Mn(CO)_5$ normalized for laser energy and absorbance. A solvent wave is also shown, normalized for laser energy. The noise spike at ~1.4 μs corresponds to the firing of the laser. Data before this point serves to define the baseline for wave integration. Integration limits are shown by dashed lines. To maximize sensitivity of the 8-bit digitizer, the baseline of the acoustic wave is deliberately offset to ensure the first negative excursion of the wave is recorded with the best possible S/N ratio. The first positive excursion of the wave is therefore 'clipped' and not fully captured.

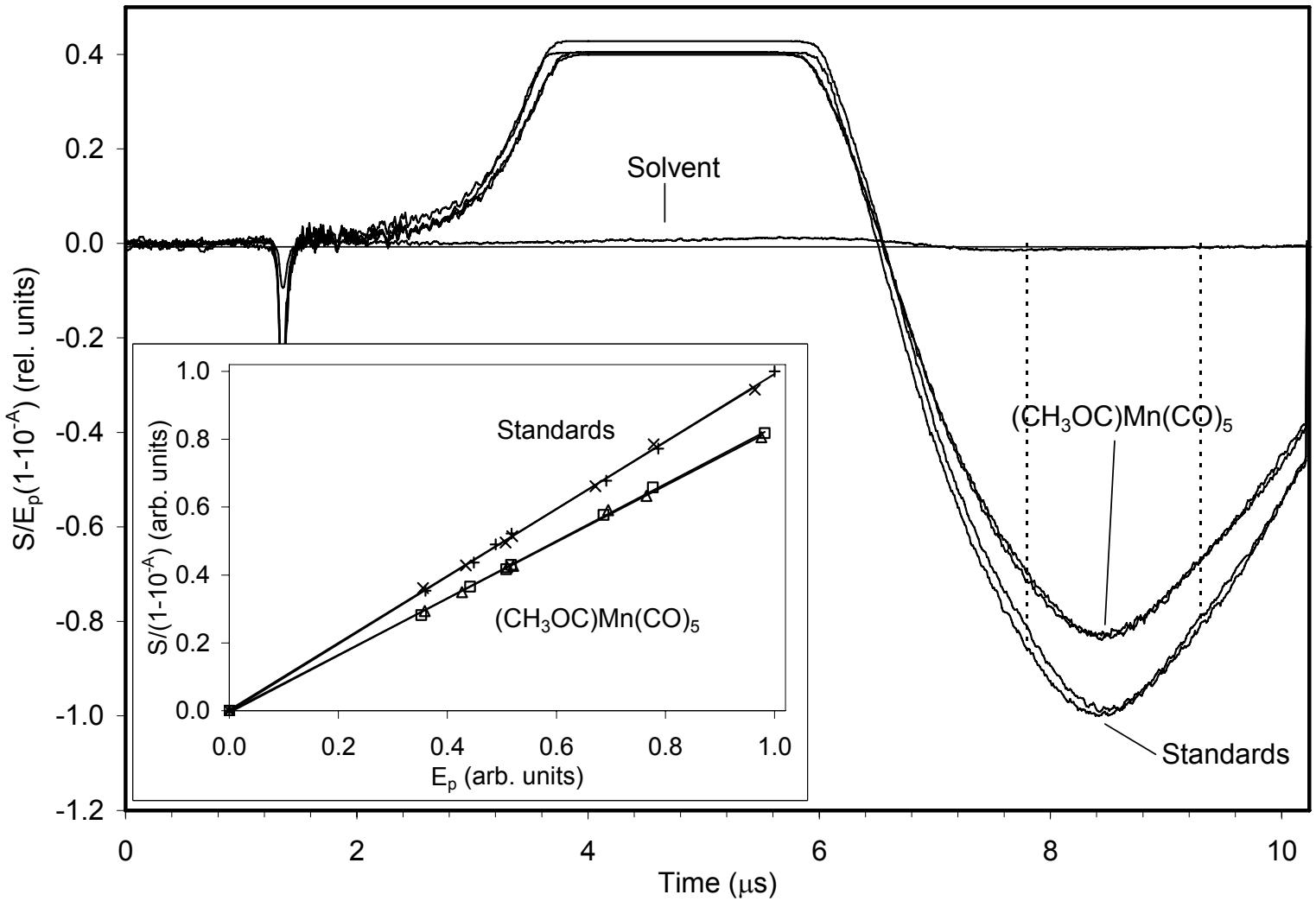

Figure 5-2 Averaged waves (30 shots) from a typical $(CH_3OC)Mn(CO)_5$ experiment at a single energy. Inset: PAC signals for $(CH_3OC)Mn(CO)_5$ and two standards plotted according to Equation 2-5

Table 5-1 Solvent Parameters and f_h^{obs} for $(CH_3OC)Mn(CO)_5$ at 25°C

Solvent	n^a	f_h^{obs}	$\alpha^{b,c}$ (1/°C)	**MW** (g/mol)	$C_p^{b,d}$ [cal/(mol*°C)]	$\rho^{b,d}$ (g/cm^3)	X_s (g/cm^3)	$f_h^{obs} * h\nu * X_s$ (cm^3)	**% Error**
Pentane	2	0.8850 ± 0.0187	0.001610	72.150	39.96	0.62139	4.678	351.1 ± 7.4	2.1%
Hexane	2	0.8746 ± 0.0108	0.001391	86.177	46.72	0.65484	3.918	290.6 ± 3.6	1.2%
Heptane	2	0.9153 ± 0.0058	0.001234[e]	100.203	53.72	0.67946	3.388	263.0 ± 1.7	0.6%
Octane	2	0.9199 ± 0.0071	0.001164	114.230	60.74	0.69862	3.133	244.5 ± 1.9	0.8%
Decane	2	0.9147 ± 0.0087	0.001051	142.284	75.18	0.72635	2.738	212.5 ± 2.0	1.0%
Dodecane	2	0.9151 ± 0.0156	0.000974	170.337	89.86	0.74518	2.478	192.3 ± 3.3	1.7%
Hexadecane	2	0.8906 ± 0.0093	0.000889[e]	226.450	119.85	0.76996	2.182	164.8 ± 1.7	1.0%

a. number of experiments
b. [63]
c. [64]
d. [65]
e. at 20°C

In a single experiment, at least four measurements of $f_h^{obs}\kappa'$: two for the sample, and one each for two different standards (typically ferrocene or tetraphenylethylene). $f_h^{obs}\kappa'$ for the sample and standards were averaged to determine f_h^{obs} for $(CH_3OC)Mn(CO)_5$ in each experiment. Photoacoustic signals were observed to be baseline for the neat solvent (*i.e.* no background photoacoustic response was generated by the solvent). All f_h^{obs} measurements for a particular solvent were averaged; the compiled results for all experiments are shown in Table 5-1.

5.4 DISCUSSION

5.4.1 The Reaction Enthalpy

Figure 5-3 shows the data in Table 5-1 plotted with Equation 2-7; for comparison, plots for $Cr(CO)_6$, $CpMn(CO)_3$, and standards (known to have $\Delta V_{rxn} = 0$) are also shown. Analysis of the PAC data for $(CH_3OC)Mn(CO)_5$ with Equation 2-7 gives a highly linear fit ($R^2 = 0.9950$) and yields $f_h = 0.8568 \pm 0.0270$ and $\Delta V_{chem} = 11.79 \pm 2.36$ mL/mol.

The Φ_{diss} has been reported to be 0.63 in cyclohexane,[108] 0.60 in various hydrocarbons, halocarbons, and ether,[106] and 0.62 in various organic solvents (no errors reported);[105] we have used the average of these values in our analysis ($\Phi_{diss} = 0.617$). Using this quantum yield and Equations 2-8 and 2-9, we have determined $\Delta H_{rxn} = 19.7 \pm 0.6$ kcal/mol, and $\Delta V_{rxn} = 19.1 \pm 3.8$ mL/mol.

$$f_h^{obs} h \nu X_s = f_h h \nu X_s + \Delta V_{chem}$$

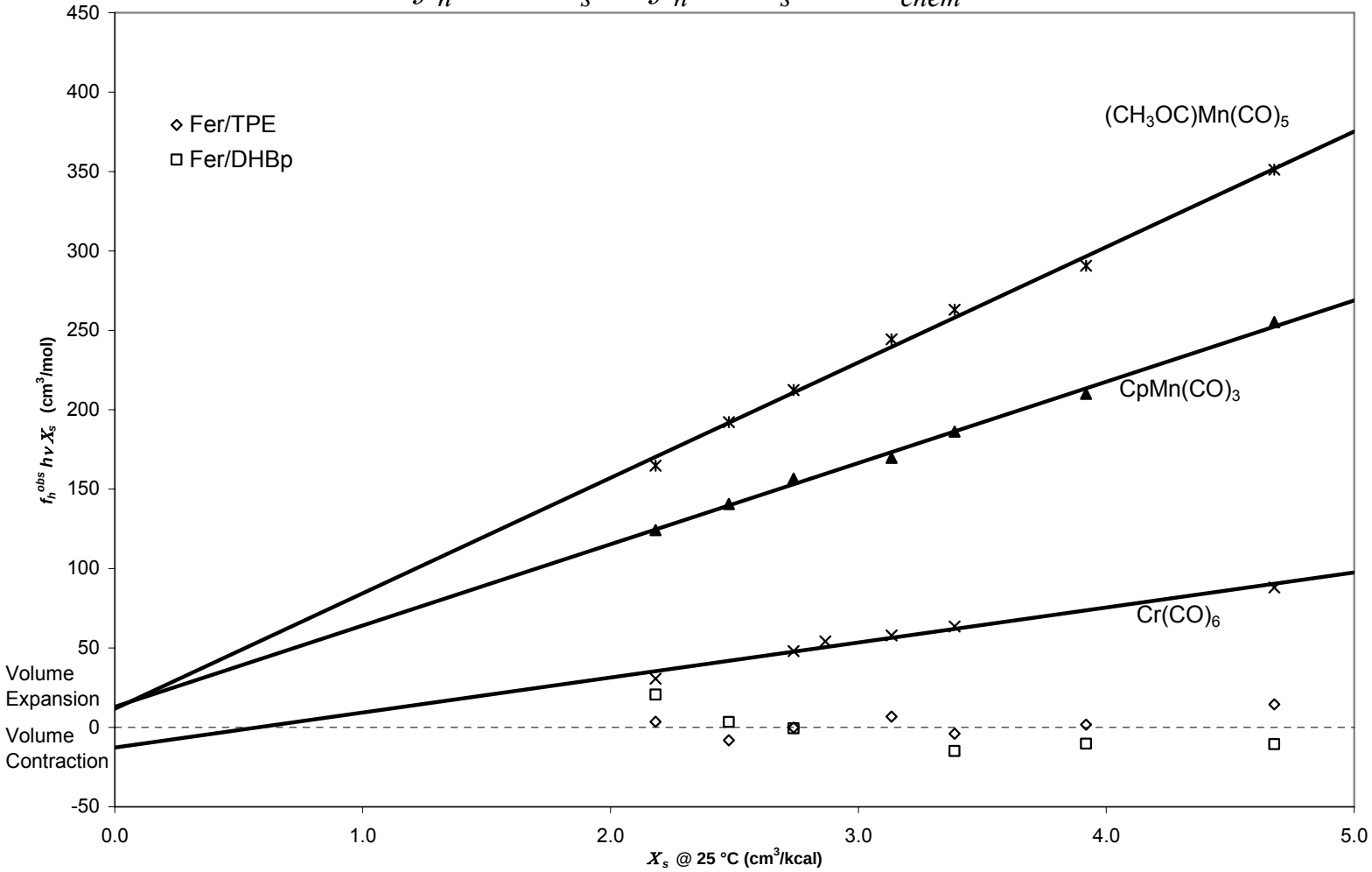

Figure 5-3 f_h^{obs} data for $(CH_3OC)Mn(CO)_5$, $CpMn(CO)_3$, $Cr(CO)_6$, and standards in linear alkanes, plotted according to Equation 2-7. The data points for $Cr(CO)_6$ have been corrected to account for the differences in Φ_{diss}.

Computational work performed by Derecskei-Kovacs and Marynick predicts ΔH_{rxn} for (A) → (C) to be 14.1 kcal/mol, and (A) → (B) to be 23.0 kcal/mol using high-level calculations (DFT/B3LYP with a triple-ζ representation of the metal atom and an f polarization function).[104] Both of these calculated enthalpies are comparable to our experimental result, but (I) cannot be assigned to either (C) nor (B) from these calculations. Computational determinations of organometallic energetics commonly result in errors comparable to the difference between these experimental and computational results. Additionally, the actual reaction may be partitioned between both (C) and (B), further complicating the assignment of the intermediates structure via energetic considerations alone.

5.4.2 The Volume Change of the Reaction

In order to appreciate the error that ignoring ΔV_{rxn} (i.e. assuming the entire photoacoustic signal was attributable to heat deposition) would add to ΔH_{rxn}, we report in Table 5-2 the ΔH_{rxn} for each solvent following the incorrect assumption that $f_h = f_h^{obs}$ for $(CH_3OC)Mn(CO)_5$. Clearly, it is essential to account for ΔV_{rxn} in this system in order to accurately measure reaction thermochemistry.

Table 5-2 Magnitude of errors caused by failing to account for ΔV_{rxn} when measuring ΔH_{rxn}

	ΔH_{rxn}, neglecting ΔV_{rxn}	Error in ΔH_{rxn} if ΔV_{rxn} neglected	% Error
Pentane	15.8	-3.9	-24%
Hexane	17.2	-2.4	-14%
Heptane	11.6	-8.0	-69%
Octane	11.0	-8.7	-79%
Decane	11.7	-8.0	-68%
Dodecane	11.7	-8.0	-69%
Hexadecane	15.0	-4.6	-31%

5.4.3 Identifying the Structure of the Intermediate from the Volume Change of the Reaction

In our early attempts to identify the structure of the intermediate, I predicted that calculation of the van der Waals volume for $(CH_3OC)Mn(CO)_5$ and each of the intermediates might couple with our PAC measurements to provide us with insight as to the form of the transient intermediate. This approach proved to be overly simplistic; while van der Waals volumes may provide a useful measure of a molecule's occupied volume, they fail to account for two important aspects of the volume of a solvated molecule: (i) the solvated volumes stem from solvent-excluded volumes; (ii) portions of the molecule's solvent-exclusive surface may not be equally accessible to the solvent as individual solvent molecules move in and out of these openings (much as a room may be less accessible when someone is standing in its doorway). Both issues may be readily visualized by the reader by imaging an extreme case, such as an ion

channel or enzyme pocket and a single solvent molecule of similar dimensions to the pocket. Not only does the surface of these macromolecules exclude the solvent from more space than the van der Waals volume of the atom alone, but the presence of a solvent molecule in the opening may block the internal free volume until it diffuses out of the pocket. It is also clear that if certain spaces may be inaccessible to the solvent at varying times, the solvated volume of the molecule will be best represented as a time-average of possible solute-solvent configurations. Accounting for these two shortcomings is far more involved than the straight-forward van der Waals approach, and so we decided to test the simpler case first.

To test the van der Waals approach, we used the optimized structural coordinates reported by Derecskei-Kovacs and Marynick for $(CH_3OC)Mn(CO)_5$ and each of the intermediates, and computed the van der Waals volume using the CACHe program (CACHe Worksystem Pro Version 6.1, Fujitsu Ltd.). The calculated van der Waals volumes are: (A) - 110.1 mL/mol; (C) - 96.6 mL/mol; (B) - 95.8 mL/mol, CO - 17.3 mL/mol. The van der Waals volume calculation predicts ΔV_{rxn} for (A) → (C) + CO = 3.8 mL/mol, and for (A) → (B) + CO = 3.0 mL/mol. Neither of these is comparable with the 19.1 mL/mol found by PAC. Clearly, a more sophisticated approach will be needed to distinguish between the proposed intermediates.

5.5 CONCLUSION

The van der Waals approach to estimating volumes is not suitable for interpreting photoacoustically-determined ΔV_{rxn}'s, because this model is overly simplistic. However, the 'missing' features in the van der Waals approach are present in molecular dynamics (MD)

simulations. Recent results from Ridley *et al.* have replicated a photoacoustically determined ΔV_{rxn} *in silico*,[116] suggesting that MD simulations may allow interpretation of the PAC-measured ΔV_{rxn}. Many organometallic compounds, such as $(CH_3OC)Mn(CO)_5$, lack force field parameters which would allow MD simulations to be performed. These force field parameters can be developed through *ab initio* calculations, but given the complexity of both molecular dynamics simulations and assignment of organometallic MD force field parameters, I chose to develop our MD approach on simpler organic systems in water. My development of a protocol for the MD simulation of ΔV_{rxn} is laid out in the next chapter of this dissertation.

6.0 PREDICTION OF THE VOLUME OF REACTION FOR ORGANIC MOLECULES VIA MOLECULAR DYNAMICS SIMULATIONS

6.1 INTRODUCTION

Molecular dynamics (MD) simulations model the interactions of individual molecules in solution by applying Newtonian forces to the molecules, the net effects of which emulate both microscale and bulk properties of the solution. MD simulations can maintain isothemal/isobaric conditions at for a constant number of molecules, temperature, and pressure by modifying the volume coordinate (nPT MD). We have used MD simulations in an attempt to determine the solvated volumes of solute molecules, and to determine the volume change accompanying a reaction. Our ultimate goal is to utilize the ΔV_{rxn} determined *in silico* to better understand experimental PAC results.

My ultimate goal is to model different the volume changes for various intermediates in a photolysis reaction, so that experimental measurements of ΔV_{rxn} may be used to gain insight into the structure of the intermediate. To ensure these simulations are able to distinguish between structurally isomeric intermediates of a photolysis reaction (such as the reaction discussed in Section 5), it is necessary to determine whether MD calculations can accurately predict ΔV_{rxn} for both dissociative reactions and isomerization processes. To accomplish this, we have selected two systems for study: the trans- to cis- photoisomerization of azobenzene (AB) in water

(Equation 6-1); and the photolytic dissociation reaction of diphenylcyclopropenone (DPCP) into carbon monoxide and diphenylacetylene (DPA) (Equation 6-2). By modeling the volume change accompanying the trans- to cis- isomerization of azobenzene, I will test the quality of the ΔV_{rxn} predicted by MD simulations of small molecules. The isomerization of AB has been previously measured photoacoustically, and in one of these studies a custom MD simulation code was able to match a modeled ΔV_{rxn} to that of the PAC measurement.[116, 117] MD simulations of AB will allow us to benchmark our MD simulations against both another MD approach and experimental data.[116] MD simulations of DPCP will test how well these calculations are able to model the reaction volume for dissociative reactions. DPCP has been extensively measured via PAC in linear alkanes,[21, 22, 45, 118, 119] allowing this system to provide a bridge between MD simulations in water and simulations using alkane solvent systems.

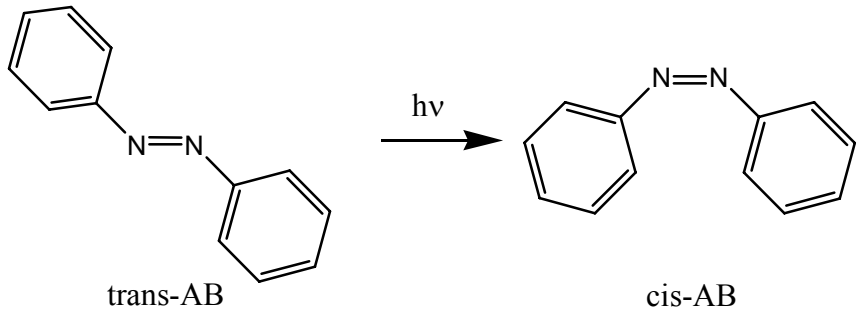

(6-1)

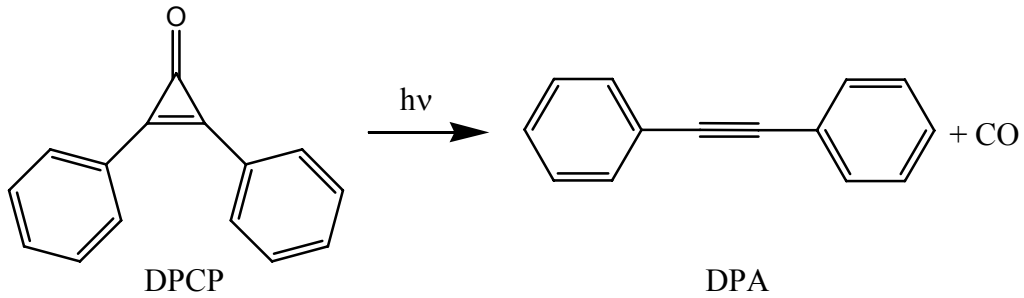

(6-2)

6.2 EXPERIMENTAL

Our MD methodology has been based on the 'pluck' approach used in a collaboration between the Space and Larsen groups.[116, 120] Significant differences exist between the Space/Larsen approach and the one described here; the Space and Larsen groups have made use of a specialized code, while we have chosen to utilize the widely-available and general Amber package.

6.2.1 Overview of Molecular Dynamics Simulations

A detailed protocol for these simulations, including the specific settings and MD force field parameters used in our simulations, has been included in Appendix B.

In MD simulations, the behavior of the individual molecules is modeled via Newton's Laws of Motion. Properties of the bulk (*e.g.* temperature, viscosity) may be determined from the net behavior of the molecules; a number of different force fields have been developed that apply model potentials to each of these molecules, and cause them to interact in ways at the microscale that replicate various macroscale physical properties. In order to successfully determine the thermodynamic solvated volume of a molecule, our MD parameters must be carefully chosen to model the conditions of our experiment.

Both steric and electrostatic interactions of molecules play a major role in the behavior of the system. We have followed the approach of Larsen, Space, *et al.* in our use of the flexible single point water model (SPC/Fw) to perform explicit solvent simulations. In this water model, a charge is placed on each of the atoms of the water molecule which accurately recreate the

permanent dipole of condensed phase water in the MD software. Our solutes were modeled using the General Amber Force Field (GAFF). We have chosen to use GAFF instead of the Amber99 force field (as was done by Larsen *et al.* in their AB simulations) because Amber99 was specifically designed for proteins and biomolecules, and as such lacks many parameters needed for our MD simulations. GAFF is an extension of the Amber99 force field parameters that is intended to serve as a general force field parameter set for organic molecules, and includes parameters for a number of additional substructures found in common organic molecules, but absent from most biomolecules.

6.2.2 Initial Structures and Charge Assignment

The initial structures of cis- and trans-AB were based on the *ab initio* calculations of Chen and Chieh.[121] The starting structure for DPCP was based on the work of Poloukhtine and Popik, [122] while the structures of DPA and CO were prepared using typical bond lengths. All starting structures were minimized in Gaussian 03 [123] using HF/6-31g* basis set in order to ensure compatibility with the charge-fitting protocol employed by Antechamber (a program in the Amber 9 suite).[124] Following this structure minimization, a single-point calculation was performed in Gaussian 03 in order to output the electrostatic potentials throughout the space surrounding the molecule. Antechamber was then used to fit RESP charges to each atom that reproduced this three-dimensional set of electrostatic potentials. Antechamber also assigned preliminary GAFF atom types to each atom in the solutes and chose force field parameters for all bond lengths, bond angles, and torsions based on these atom types. These assignments were carefully reviewed to ensure they were physically meaningful and appropriate. Though GAFF is a general force field, it lacked a number of needed force field parameters (*e.g.* the ketone moiety

of the cyclopropenone). For these missing parameters, we either used parameters from analogous molecular substructures in the GAFF parameter library, or chose parameters which would ensure physically-expected behaviors (*e.g.* the cyclopropenone moiety is expected to be highly rigid; large force constants were chosen with this in mind.) We have included our 'frcmod' files in Appendix C; the parameters in these files augment or supersede force field parameters included in GAFF.

A solvent box consisting of SPC/Fw water molecules was prepared around each solvent using xLeap, a program in the Amber 9 suite. For each of the solutes involved in a particular reaction, care was taken to add an identical number of water molecules (987 for cis- and trans-azobenzene, and 1008 for DPCP, DPA, and CO). For both reactions, a simulation was also run that consisted of only water molecules, allowing each solute volume to be determined at the end of the MD simulations via Equation 6-3. This approach has been referred to as the 'pluck' approach for determining molecular volumes.[116, 120]

$$V_{solute+water} - V_{water} = V_{solute} \tag{6-3}$$

6.2.3 Molecular Dynamics Simulations

The following simulations were all performed using 4 processors each on the University of Pittsburgh/CMMS's Opteron cluster (Markov). All simulations were performed using periodic boundary conditions, and a 9 Å cutoff for intermolecular forces was used to ensure the solute could not 'see' its own forces in a neighboring box while still keeping the box sizes and numbers of water molecules small. The positions of the solvent molecules were minimized with the position of the solute was restrained, allowing bad van der Waals contacts between water molecules to be rapidly removed. Next, the positional restraints on the solute were released,

allowing the positions of all molecules to be minimized. The system was then heated from 0 to 300 K under MD/nPV conditions (*i.e.* with constant pressure, volume, and number of molecules). The MD simulations then switched to nPT conditions (constant number of molecules, pressure, and temperature, with pressure maintained via by fluctuating periodic boundary size), the system was compressed until the pressure reached 1 atm. Additional simulations were designed to consider the effects observed if structure of the solute were made rigid via positional restraints (*vide infra*, Section 6.3.1). Initially, these simulations modeled 200 ps of nPT data, sampled every 0.1 ps. The resulting simulation values (volume, energy, pressure, *etc*.) were plotted versus simulation time in order to determine when equilibrium was reached; values collected after equilibration had been reached were averaged to allow an initial analysis.

This initial analysis was useful for determining if the simulation was well-behaved and if the chosen force field parameters were resulting in physically expected behaviors. However, a second round of simulations was required in order to yield statistically meaningful averages and standard deviations, with longer simulation times between data outputs to ensure the values were statistically uncorrelated. This correlation time was determined using the method described in [125, 126]. First, the average volume ($\overline{V}_{run}$) was determined for all time points after the pressure

$$\overline{V}_b = \frac{1}{\tau_b}\sum_{\tau=1}^{\tau_b} V(\tau) \tag{6-4}$$

$$\sigma^2\left(\overline{V}_b\right) = \frac{1}{n_b}\sum_{b=1}^{n_b}\left(\overline{V}_b - \overline{V}_{run}\right)^2 \tag{6-5}$$

$$s = \lim_{\tau_b \to \infty} \frac{\tau_b \sigma^2\left(\overline{V}_b\right)}{\sigma^2\left(\overline{V}\right)} \tag{6-6}$$

had equilibrated under nPT conditions (τ_{run}). The data were split into blocks of containing a varying number of data samples (n_b). The length of the block is then given by $n_b \tau_b = \tau_{run}$. The average volume for a particular block was calculated by Equation 6-4, and the average volume for all blocks of a given size was then used to determine the variance via Equation 6-5. The statistical inefficiency (s) was calculated for an array of block sizes via Equation 6-6 and plotted as in Figure 6-1. The plateau s value on a plot of s vs. τ_b indicates the number of times that the volume was sampled between statistically independent points for the sampling frequency used; this may alternately be determined from the y-intercept of s vs. $1/\tau_b$. We have averaged the result of both methods in our determination of the correlation time.

After determining the correlation time for each set of simulation conditions, the simulation was restarted with the sampling time chosen to output only statistically uncorrelated values for the volume. All simulations were run for >40 ns of simulation time. Once complete, a plot of volume vs. time was inspected for each simulation, and the average volumes and standard deviations were computed. Finally, the volumes of the water-only simulations were subtracted from those of the solute/water systems, and the total volumes of the products were subtracted from the total volumes of the reactants to determine ΔV_{rxn}.

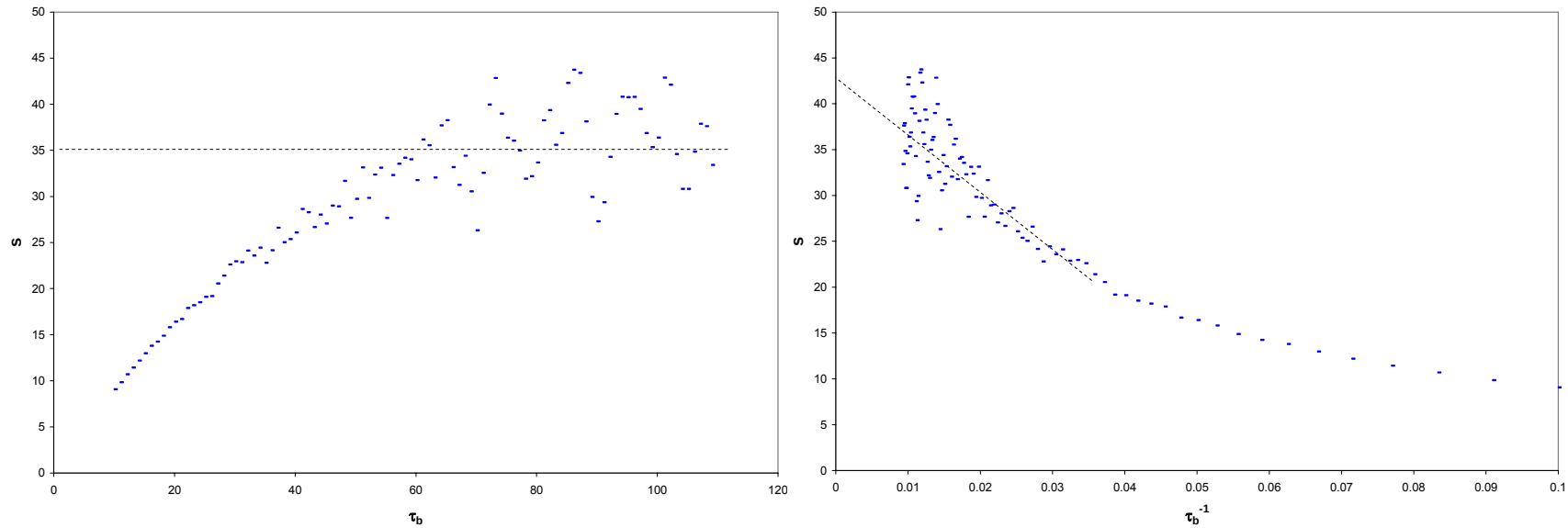

Figure 6-1 Typical plots of *s* from Equation 6-6, used to determine the number of samples between statistically uncorrelated points. In this example, the left plot predicts that 35 samples could be taken between uncorrelated points, while the plot on the right predicts 43; in this example, 40 samples (i.e. 4.0 ns) was chosen as our simulation sampling time.

6.3 RESULTS AND DISCUSSION

6.3.1 Initial Simulations

During our initial simulations the solutes were modeled under each of three conditions:

- the solute was held in place throughout the simulation by a 500 kcal*mol^{-1}*Å^{-2} restraint (*i.e.* initial structure always maintained);
- the solute was held in place after the completion of both minimization steps by a 10 kcal*mol^{-1}*Å^{-2} restraint (i.e. maintaining the structure of the post-minimization conformation, with some ability to flex/twist);
- the solute was not restrained, and behavior was solely dictated by force field parameters.

The results for each of these initial simulations are shown in Table 6-1 and Table 6-2.

If all MD parameters were completely appropriate (*i.e.* perfectly modeled nature when used with the MD algorithms), it was anticipated that the simulations would be most accurate when no restraints were used. However, we were also interested in whether MD simulations using restraints could yield accurate results, allowing these methods to be used on systems with unknown MD parameters (*e.g.* organometallic systems). We were also interested in comparing simulations times (i.e. the 'wall clock' times) to optimize our potential ability to use MD simulations alongside experimental measurements in a routine fashion.

Table 6-1 Results for the initial molecular dynamics simulations of azobenzene/water

Restraints	Solute Conditions	Water/solute Volume (mL/mol)	Molecular Volume (mL/mol)	ΔV_{rxn} trans --> cis (mL/mol)
No restraints	cis-AB - without charges	18,522.4	168.3	-23.6
	trans-AB - without charges	18,545.9	191.9	
Restraints during MD	cis-AB - without charges	18,525.7	171.7	30.6
	trans-AB - without charges	18,495.1	141.0	
Restraints always on	cis-AB - without charges	18,532.7	178.6	5.9
	trans-AB - without charges	18,526.8	172.7	
No restraints	cis-AB - with charges	18,529.9	175.8	-15.4
	trans-AB - with charges	18,545.3	191.2	
Restraints during MD	cis-AB - with charges	18,515.0	160.9	0.9
	trans-AB - with charges	18,514.1	160.1	
Restraints always on	cis-AB - with charges	18,525.8	171.8	-1.6
	trans-AB - with charges	18,527.4	173.4	
	Water only	18,354.1		

Table 6-2 Results for the initial molecular dynamics simulations of DPCP/water

Restraints	Solute Conditions	Water/solute Volume (mL/mol))	Molecular Volume (mL/mol)	ΔV_{rxn} DPCP --> DPA + CO (mL/mol)
No restraints	DPCP - with charges	18,944.8	195.8	20.8
	DPA - with charges	18,925.4	176.4	
	CO - with charges	18,789.2	40.2	
Restraints always on	DPCP - with charges	18,918.7	169.7	73.2
	DPA - with charges	18,948.5	199.6	
	CO - with charges	18,792.3	43.4	
	Water	18,749.0		

For the azobenzene simulation performed without restraints, ΔV_{rxn} was -23.6 mL/mol without charges on the solute, and -15.4 mL/mol with charges. This stands in contrast to Larsen *et al.*'s calculation of +3.8 mL/mol without charges, and -3.6 mL/mol with charges, as well as the experimentally-determined result of ΔV_{rxn} = -3.5 mL/mol (average of [116] and [118]).

The error between $\Delta V_{rxn,exp}$ and $\Delta V_{rxn,model}$ was even worse when the minimized structure was restrained; with charges turned off, ΔV_{rxn} = 30.6 mL/mol, and with them on ΔV_{rxn} = 0.9 mL/mol. If the original structure was maintained via restraints throughout the simulation, ΔV_{rxn} = 5.9 mL/mol without charges, and ΔV_{rxn} = -1.9 mL/mol with charges.

We interpret the poor agreement for our azobenzene simulations without restraints as indicating that the force field parameters were not well-suited to the simulation. We also note that if the difference between the solute volumes with/out charges is viewed as a probe of the degree of electrostriction, these results agree well with those of Burkey *et al.* (8.2 mL/mol for AB with charges vs. 7.4 mL/mol without charges.) This indicates that the average conformations in this simulation do not agree well with that of Burkey *et al.*, but the way in which the solute interacts with the solvent is similar. This suggests that by improving our chosen force field parameters, our methodology will yield results that can be used to better understand PAC data.

For the case where restraints were turned on at the end of the solvent minimization steps, our agreement with Larsen *et al.*'s calculation of ΔV_{rxn} for the uncharged case is extremely poor (30.6 mL/mol), while the calculation of ΔV_{rxn} for the charged case shows much better agreement (0.9 mL/mol). By restraining the structure of the solute at the end of the minimization step, we are effectively choosing a random conformation out of those permitted by the force field parameters. As such, this approach was not replicated in our later production MD simulations.

When the original conformation was maintained throughout the simulation both the charged (5.9 mL/mol) and uncharged (-1.6 mL/mol) results were in good agreement with that of Larsen *et al* (+3.8 and -3.6 mL/mol respectively). From this portion of the experiment we have learned that for molecules with inadequate force field parameterization, use of strong restraints may allow the accurate determination of ΔV_{rxn}. This also serves as preliminary data showing that conformational changes can be resolved through MD simulations.

These lessons were tested in the simulations of DPCP. DPCP is an inherently rigid molecule due to its highly strained ring structure and π-conjugation. DPA is an exceptionally linear molecule that is not expected to bend due to its central carbon-carbon triple bond. CO is a small molecule that is well-described by the existing GAFF parameters. These structural cues suggested that MD simulations for DPCP should yield a good approximation of ΔV_{rxn}, both with and without restraints since the structure of DPCP and DPA should be relatively insensitive to the chosen force field parameters.

Surprisingly, our initial simulations measured $\Delta V_{rxn} = 20.8$ mL/mol without restraints, and $\Delta V_{rxn} = 73.2$ mL/mol with them; comparison of the two trajectories shows that the unrestrained form has significant rotation of the phenyl groups, a motion that is 'turned off' under the condition of strong restraints. The original result from AB suggested that strong restraints may stand in for high-quality force field parameters if the molecule is expected to be rigid; a more refined view, in light of the behavior of DPA, is that strong restraints can effectively replace force field parameters only if the restrained structure accurately represents the time-average of the dynamic molecular structure.

6.3.2 MD Production Simulations

Using the results from the preliminary simulations, the correlation times were determined following the approach discussed in Section 6.2.1 for each set of conditions which were not excluded by the initial analysis. The original MD simulations were modified to only output statistically uncorrelated data sets (to minimize the size of the output files) and each simulation was run for >40 ns. The measured volumes are shown in Table 6-3, along with the determined correlation times. Plots of the solute/solvent volume vs. simulation time are shown in Figure 6-2 and Figure 6-3.

Table 6-3 Summary of MD Production Runs

	Correlation Time (ns)	Time (ns)	Samples	Volume (mL/mol)	±	Molecular Volume (mL/mol)	±
Cis-AB - with charges	3.5	46.4	13192	18508.9	68.6	164.8	96.3
Trans-AB - with charges	2.6	40.1	15161	18507.3	67.6	163.2	95.6
Cis-AB - without charges	4.4	40.4	9183	18524.9	69.5	180.8	96.9
Trans-AB - without charges	4.0	43.8	10462	18520.0	68.1	176.0	95.9
Water only	6.0	41.7	6931	18344.1	67.6		
DPCP	4.5	43.0	9414	18913.8	68.4	181.9	96.3
DPA	5.1	40.8	7947	18906.8	68.4	174.8	96.2
CO	6.4	40.3	6208	18769.2	69.0	37.3	96.7
Water only	5.9	41.0	6926	18732.0	67.7		

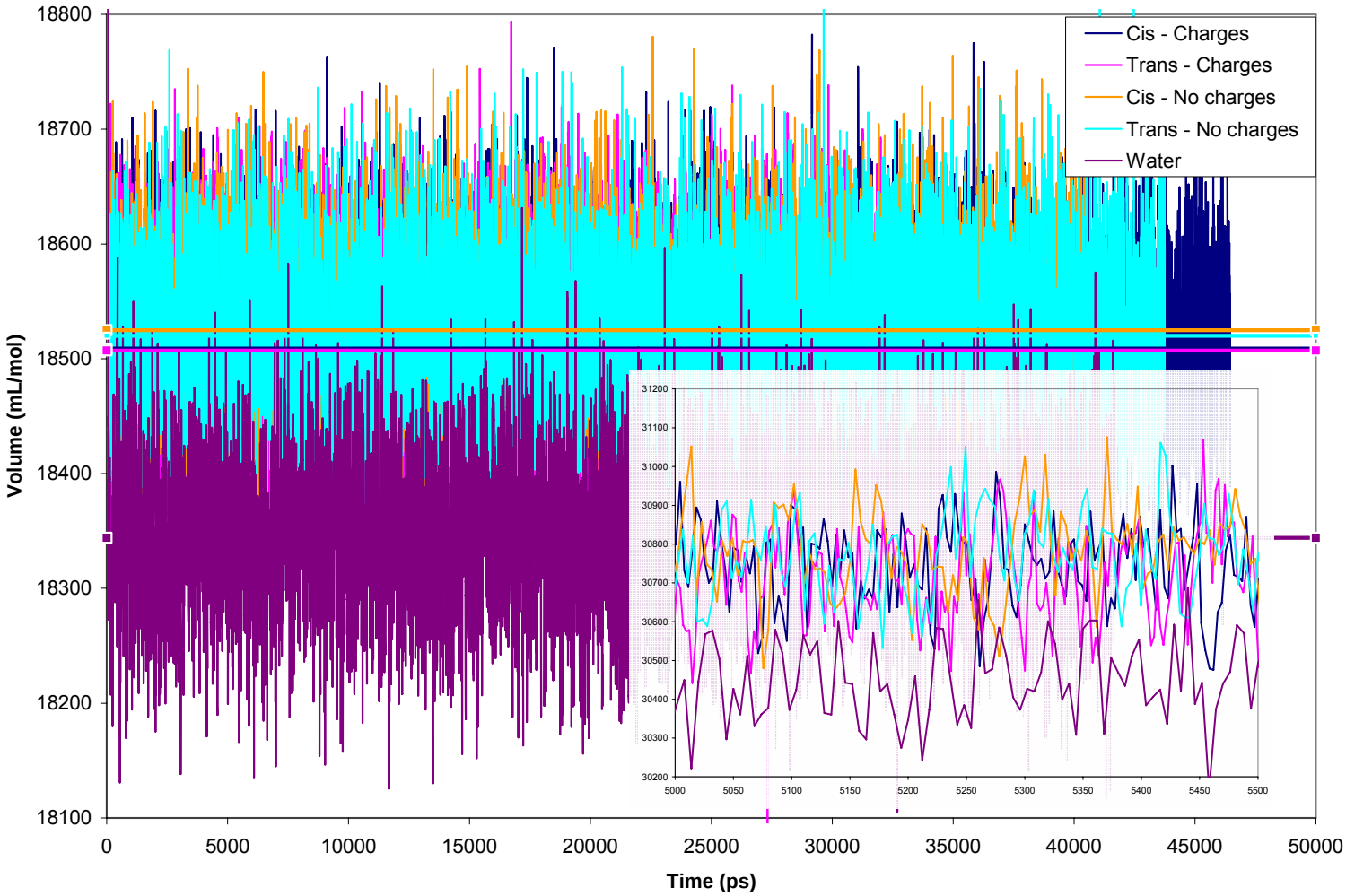

Figure 6-2 Volume vs. time plot for the azobenzene MD production run. The overlaid horizontal lines represent the average volume. Inset: detail view of part of the time coordinate.

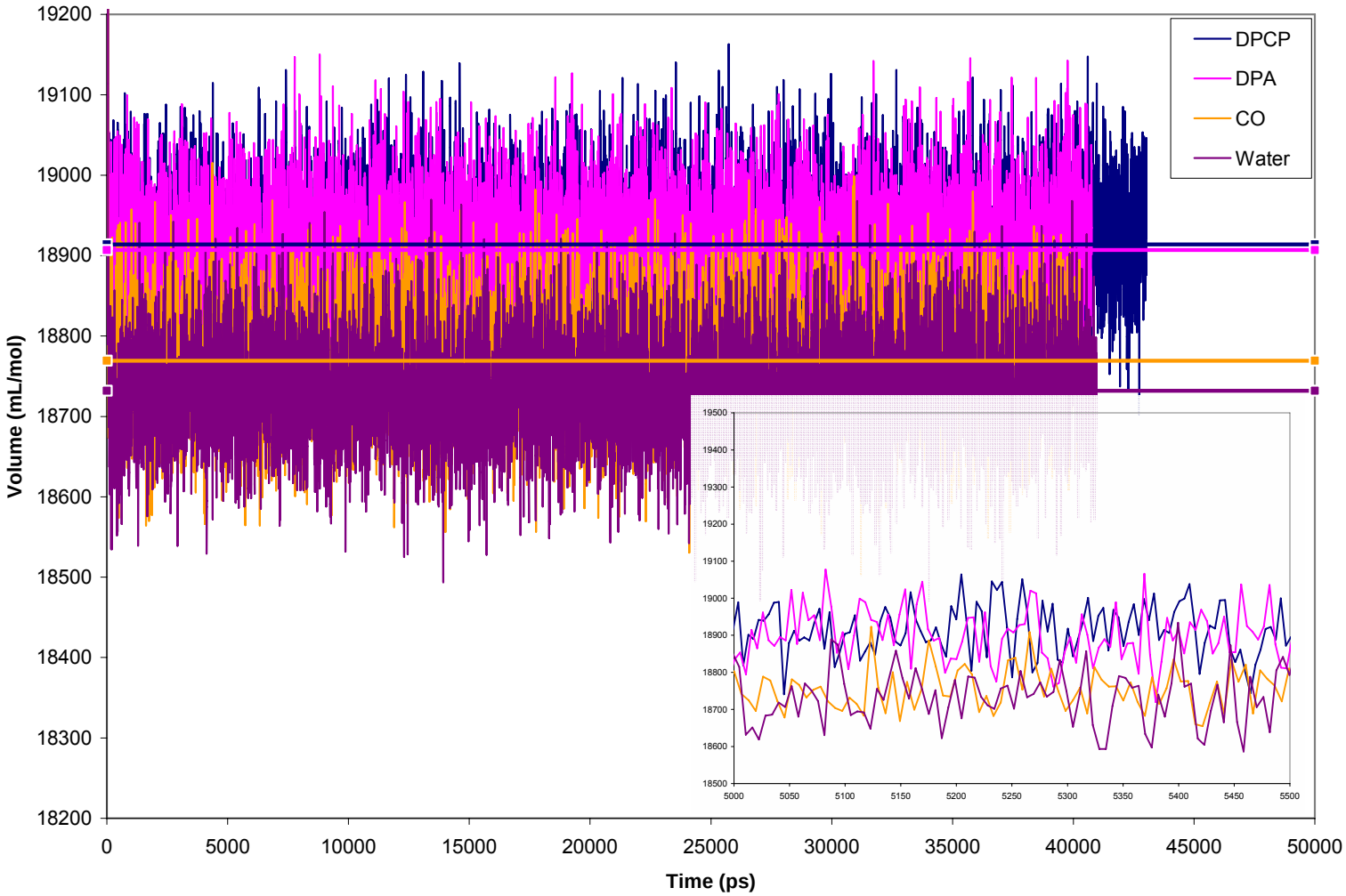

Figure 6-3 Volume vs. time plot for the DPCP MD production run. The overlaid horizontal lines represent the average volume. Inset: detail view of part of the time coordinate.

For the production runs of our MD simulations, ΔV_{rxn} = 1.6 mL/mol for the trans- to cis-isomerization of AB with solute charges, and ΔV_{rxn} = 4.9 mL/mol without them. The measurement of ΔV_{rxn} without solute charges shows good agreement with those of Larsen *et al.*, but the agreement is poor when the solute charges are incorporated in our simulation (both with the calculated result and the experimental results). This may be explained through the sheer size of the error propagated into the final ΔV_{rxn}. While the error is small *vs*. the total volumes of the system (<0.4%), this error is intractably large once the volume of the solvent has been subtracted (>50%). The simulations using the custom code of Larsen *et al.* showed much more useable errors than our in our approach. Still, a number of improvements could be made to our approach that should result in large improvements in our modeled volumes.

Our simulations used ~10x more water molecules than used by Larsen *et al*. This was necessary to ensure the electrostatics of the solute were considered over a distance where this effect is appreciable; further experiments should be performed that use smaller cutoffs, which would allow a smaller periodic box and fewer water molecules to be used. This alone should dramatically reduce the error in our average volumes. We could also move to longer simulation times and increase the number of processors allocated to each simulation in order to improve our counting statistics in a tractable amount of 'wall-clock' (*i.e.* real world, rather than simulated) time.

For the photolysis of DPCP, our simulation resulted in ΔV_{rxn} = 30.2 mL/mol. Four experimental measurements of ΔV_{rxn} have been reported in linear alkane solvents, giving an average ΔV_{rxn} of 23.2 mL/mol. Unfortunately, no PAC experiments have been performed to date that measure ΔV_{rxn} for the same reaction in both water and a linear alkane, limiting our ability to comment on this result without first completing this simulation in a linear alkane. This is

certainly the next step, both for better interpreting this simulation in water, and for laying the groundwork to perform MD simulations on $(CH_3OC)Mn(CO)_5$ in linear alkanes.

6.4 CONCLUSION

The use of molecular dynamics simulations in the analysis of photoacoustic data shows strong promise, but additional simulations are required to fully develop and test this methodology. A set of simulations should be performed for increasingly small cutoff radii in order to determine the smallest periodic cell that will give realistic volumes, in order to run simulations with fewer water molecules and the accompanying decrease in error. *Ab initio* calculations should be performed to develop high-quality force field parameters for azobenzene in order to better test the quality of simulations where large restraint potentials have been used to stand-in for these high-quality force field parameters. Finally, the photolysis of DPCP should be modeled in a linear alkane solvent; butane at ~1.2 atm or pentane at 1 atm should be computationally tractable, especially for a smaller periodic cell run on more processors than in this chapter.

APPENDIX A

PHOTOACOUSTIC DATA PROCESSING CODE FOR MICROSOFT EXCEL

The software used by our research group was developed in-house over 15 years ago, well before computer software had the level of integration that is common today. The computers that run these programs are increasingly prone to hardware failure, and even using emulation software, such as DosBox, these software programs no longer perform reliably without considerable expertise in hardware emulation. As such, I have re-written an integrated 'program' in Microsoft Excel for the analysis of photoacoustic data that allows time-independent analysis of ASCII-formatted PAC data. This spreadsheet is described here, and includes the formulae used.

A.1 ANALYSIS WORKFLOW

Insert solvent wave data sets

Insert sample wave data sets

Enter experimental record data

Enter number of laser shots

Choose integration limits for reflected, transmitted, and (optionally) transmitted waves

Set pretrigger points for reflected, transmitted, and (optionally) transmitted waves

Specify if positive or negative excursion should be integrated for sample waves

Specify absorbances for each sample set

List attenuation data used for each data set

Solvent waves

Baseline subtracted from waveforms

Peak max determined for each waveform

Integrals determined for each waveform

Solvent E(t)/E(r) determined for each wave

Sample Waves

Baseline subtracted from waveforms

Peak max determined for each waveform

Integrals determined for each waveform

Use E(t)/E(r) from solvent with E(t)/E(r) to determine PAC absorbance (if transmitted data acquired)

Plot regression for $S/(1-T_s)$, $S/(1-T_{PAC})$, $S/(1-T_{PACavg})$, and S vs. R-integral

Calculate m ± S.D., b ± S.D., and R^2 for S vs. R normalization plots – with/without (0,0) pt. included.

Normalize slopes (κf_h^{obs}) and plot

Solvent and Sample Waves

Plot waves of matched attenuation from each data set

Pool κf_h^{obs} for standards and samples

Determine f_h^{obs} for samples

A.2 SPREADSHEET CONFIGURATION

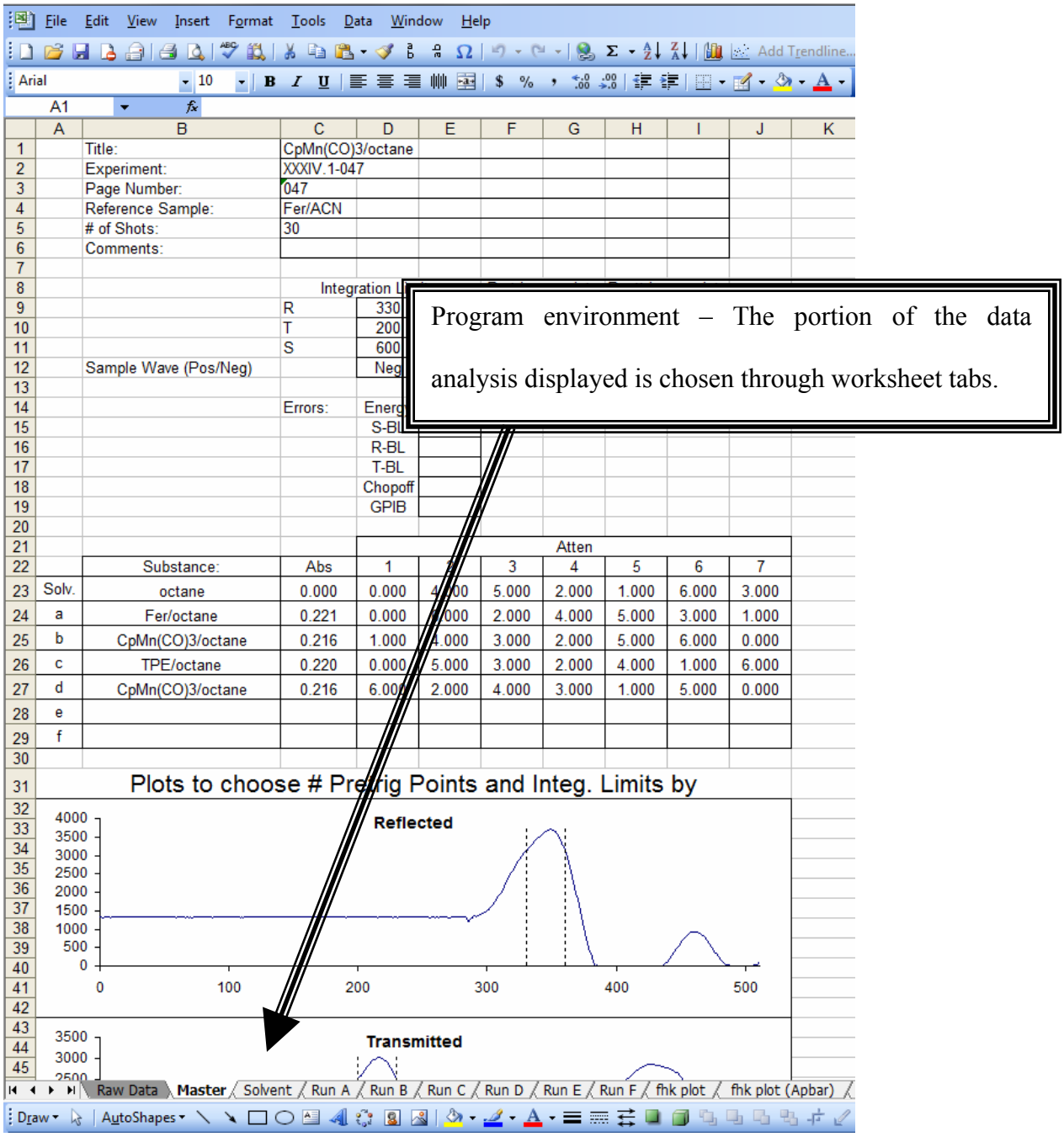

Figure A-1 Analysis spreadsheet interface

	THESE CELLS MUST BE SOLVENT DATA												Run a
Run Name→ Time↓	047-029	Channel	Value	047-030	047-031	047-032	047-033	047-034	047-035	047-001	047-002	047-003	047-004
0	1338	0	3	1282	1324	1325	1265	1346	1275	1320	1308	1286	1318
1	1339	1	4	1286	1328	1326	1264	1345	1281	1319	1303	1286	1318
2	1342	2	7	1280	1329	1328	1268	1346	1277	1315	1306	1288	1319
3	1345	3	10	[illegible]	[illegible]	[illegible]	[illegible]	[illegible]	[illegible]	1317	1309	1290	1321
4	1340	4	5	[illegible]	[illegible]	[illegible]	[illegible]	[illegible]	[illegible]	1320	1304	1286	1319
5	1342	5	7	[illegible]	[illegible]	[illegible]	[illegible]	[illegible]	[illegible]	1322	1309	1290	1321
6	1338	6	3	[illegible]	[illegible]	[illegible]	[illegible]	[illegible]	[illegible]	1326	1314	1294	1313
7	1339	7	4	[illegible]	[illegible]	[illegible]	[illegible]	[illegible]	[illegible]	1322	1309	1287	1316
8	1335	8	0	[illegible]	[illegible]	[illegible]	[illegible]	[illegible]	[illegible]	1317	1311	1285	1316
9	1338	9	3	[illegible]	[illegible]	[illegible]	[illegible]	[illegible]	[illegible]	1322	1307	1284	1313
10	[illegible]	10	3	1279	1322	1322	1271	1348	1279	1322	1309	1290	1317
11	[illegible]	11	6	1279	1326	1328	1270	1348	1275	1323	1314	1293	1321
12	[illegible]	12	0	1280	1325	1327	1271	1347	1277	1319	1307	1290	1317
13	[illegible]	13	0	1286	1323	1331	1273	1347	1280	1323	1304	1291	1320
14	[illegible]	[illegible]	[illegible]	1279	1324	1326	1270	1353	1281	1322	1306	1293	1312
15	[illegible]	[illegible]	[illegible]	1284	1325	1325	1266	1349	1278	1320	1306	1293	1322
16	[illegible]	16	2	1282	1330	1321	1264	1347	1275	1319	1308	1289	1322
17	[illegible]	17	3	[illegible]	1331	1327	1269	1350	1276	1326	1301	1292	1317
18	[illegible]	18	4	[illegible]	1327	1325	1267	1347	1275	1321	1310	1298	1319
[illegible]	[illegible]	[illegible]	-1	[illegible]	1328	1324	1264	1347	1283	1327	1303	1294	1322
[illegible]	[illegible]	[illegible]	0	1278	1328	1324	1263	1350	1275	1322	1307	1290	1320
[illegible]	[illegible]	[illegible]	0	1285	1329	1327	1267	1348	1280	1321	1304	1294	1321
22	1340	22	[illegible]	1280	[illegible]	1324	1268	1343	1276	1321	1306	1301	1321
23	1334	23	[illegible]	1275	[illegible]	1327	1269	1341	1280	1321	1307	1292	1319
24	1333	24	[illegible]	[illegible]	1328	1322	1269	1343	1272	1320	1304	1291	1319
25	1339	25	[illegible]	[illegible]	[illegible]	[illegible]	[illegible]	1347	1280	1324	1299	1297	1322
26	1337	26	[illegible]	[illegible]	[illegible]	[illegible]	[illegible]	1350	1273	1321	1301	1297	1318
27	1335	27	[illegible]	[illegible]	[illegible]	[illegible]	[illegible]	1351	1281	1321	1304	1297	1320
28	1331	28	-4	1282	[illegible]	[illegible]	[illegible]	1348	1277	1323	1306	1293	1318
29	1333	29	-2	1293	[illegible]	[illegible]	[illegible]	1352	1279	1322	1307	1290	1320
30	1339	30	4	1280	[illegible]	[illegible]	[illegible]	1345	1282	1322	1309	1293	1315
31	1339	31	4	1282	[illegible]	[illegible]	[illegible]	1343	1277	1323	1302	1296	1317
32	1336	32	1	1275	1336	1325	1265	1345	1272	1326	1311	1288	1313
33	1335	33	0	1282	1332	1324	1268	1344	1270	1324	1306	1295	1313
34	1332	34	-3	1287	1327	1328	1265	1350	1275	1324	1307	1290	1316
35	1333	35	-2	1280	1330	1324	1266	1347	1279	1325	1303	1292	1315
36	1335	36	0	1276	1329	1321	1265	1344	1277	1322	1304	1288	1315
37	1333	37	-2	1283	1327	1325	1269	1343	1270	1320	1306	1289	1322
38	1336	38	1	1282	1333	1324	1265	1347	1277	1320	1307	1292	1314
39	1338	39	3	1281	1336	1329	1268	1347	1273	1325	1309	1288	1317
40	1332	40	-3	1282	1332	1326	1267	1344	1275	1326	1309	1283	1319
41	1334	41	-1	1287	1332	1321	1271	1347	1278	1327	1300	1289	1310
42	1336	42	1	1289	1326	1321	1266	1347	1273	1323	1306	1297	1312
43	1337	43	2	1286	1328	1332	1271	1351	1278	1323	1305	1289	1315

Raw data for other solvent waves (Channel number and Baseline subtracted value columns are hidden to simplify data input.)

Raw data

Channel number

Baseline subtracted value

Figure A-2 This page contains the source data to be analyzed. There are two hidden columns between each data entry column, used to list the channel number of the point (for indexing in later formulae) and the baseline-subtracted value for each point of the wave. The first 512 points of the column contain the reflected wave data values, the second 512 points contain the transmitted points, and the final 1028 points contain the sample wave data.

Run Name→ Time↓	047-029	Channel	Value
0	1338	0	=B3-Solvent!$F$19
1	1339	1	=B4-Solvent!$F$19
2	1342	2	=B5-Solvent!$F$19
3	1345	3	=B6-Solvent!$F$19
4	1340	4	=B7-Solvent!$F$19
5	1342	5	=B8-Solvent!$F$19
6	1338	6	=B9-Solvent!$F$19
7	1339	7	=B10-Solvent!$F$19
8	1335	8	=B11-Solvent!$F$19
9	1338	9	=B12-Solvent!$F$19
10	1338	10	=B13-Solvent!$F$19
11	1341	11	=B14-Solvent!$F$19
12	1335	12	=B15-Solvent!$F$19
13	1335	13	=B16-Solvent!$F$19
14	1336	14	=B17-Solvent!$F$19
15	1333	15	=B18-Solvent!$F$19
16	1337	16	=B19-Solvent!$F$19
17	1338	17	=B20-Solvent!$F$19
18	1339	18	=B21-Solvent!$F$19
19	1334	19	=B22-Solvent!$F$19
20	1335	20	=B23-Solvent!$F$19
21	1335	21	=B24-Solvent!$F$19
22	1340	22	=B25-Solvent!$F$19
23	1334	23	=B26-Solvent!$F$19
24	1333	24	=B27-Solvent!$F$19
25	1339	25	=B28-Solvent!$F$19
26	1337	26	=B29-Solvent!$F$19
27	1335	27	=B30-Solvent!$F$19
28	1331	28	=B31-Solvent!$F$19
29	1333	29	=B32-Solvent!$F$19
30	1339	30	=B33-Solvent!$F$19
31	1339	31	=B34-Solvent!$F$19
32	1336	32	=B35-Solvent!$F$19
33	1335	33	=B36-Solvent!$F$19
34	1332	34	=B37-Solvent!$F$19
35	1333	35	=B38-Solvent!$F$19
36	1335	36	=B39-Solvent!$F$19

Figure A-3 Formulae from Figure A-2.. Constant values appear as numbers; derived values appear as an Excel formula. Only one baseline subtraction is shown above.

	Title:	CpMn(CO)3/octane							
	Experiment:	XXXIV.1-047							
	Page Number:	047							
	Reference Sample:	Fer/ACN							
	# of Shots:	30							
	Comments:								
		Integration Limits:			Pretrigger points	Posttrigger points			
		R	330	360	280				
		T	200	230	140				
		S	600	750	70				
	Sample Wave (Pos/Neg)		Neg						
		Errors:	Energy						
			S-BL						
			R-BL						
			T-BL						
			Chopoff						
			GPIB						
			Atten						
	Substance:	Abs	1	2	3	4	5	6	7
Solv.	octane	0.000	0.000	4.000	5.000	2.000	1.000	6.000	3.000
a	Fer/octane	0.221	0.000	6.000	2.000	4.000	5.000	3.000	1.000
b	CpMn(CO)3/octane	0.216	1.000	4.000	3.000	2.000	5.000	6.000	0.000
c	TPE/octane	0.220							6.000
d	CpMn(CO)3/octane	0.216							0.000
e									
f									

User input

User input, chosen by examination of displays below

User input, not required; allows reporting of instrument behavior

User input, Abs used to determine ($1-10^{-A}$), atten used to later to display waves of similar E_p

Plots to choose # Pretrig Points and Integ. Limits by

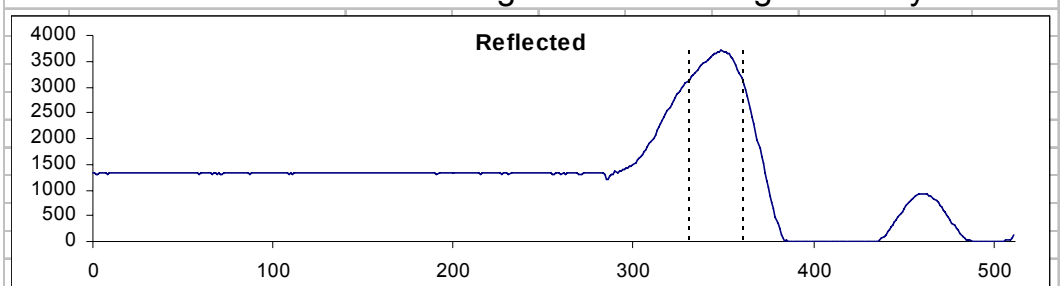

Figure A-4 Experiment input form. There are no derived values in this section. The waves displayed at the bottom of this page(the transmitted and sample wave not shown) plot the untreated data of the first sample wave entered in the source data spreadsheet, simplifying selection of the integration limits and baseline. The absorbances measured on the UV-vis spectrophotometer are used to normalize the PAC signal. Entered attenuations are used to choose waves of similar E_p for comparison and plotting. The tables on this page are typically printed by the user and included in the hardcopy report.

Title: CpMn(CO)3/octane
Experiment: XXXIV.1-047
Date Printed: 28-Sep-2005
Sample: octane
Comments:

# of Shots: 30
Reference: Fer/ACN
Sample Absorbance: 0.000

Data Subset: 047 solvent

Solvent E(t)/E(r) = 1.2603 ± 0.0148 (1.2%; n = 7)

Integration Limits for R:	330	360	1.55 µs	Number of pre-trigger points =	280
Integration Limits for T:	200	230	1.55 µs	Number of pre-trigger points =	140
Integration Limits for S:	600	750	1.51 µs	Number of pre-trigger points =	70
Pos/Neg:	Neg				

Waves Excluded:

	Peak Max			Baseline			Integrals				
Filename:	R	T	S	R	T	S	R	T	S	PAC-A	SPEC-A
047-029	348	216	677	1335	1204	6831	2090	2574	38	0.000	0.000
047-030	349	217	806	1283	1229	6817	1294	1616	79	0.000	0.000
047-031	349	217	662	1326	1211	6833	1134	1443	14	0.000	0.000
047-032	349	216	670	1326	1223	6835	1554	1962	65	0.000	0.000
047-033	349	217	674	1270	1202	6823	1837	2331	49	0.000	0.000
047-034	349	218	769	1347	1225	6828	1015	1287	61	0.000	0.000
047-035	349	217	830	1276	1211	6830	1435	1821	40	0.000	0.000
Average	349	217	727	1309	1215	6828				0	0
S.D.	0	1	72	32	11	6				0	0
Count	7	7	7	7	7	7				7	7

From this point forward, all calculations occur without user interventions

Calculation of E(t)/E(r) (if the solvent data were collected)

Spreadsheet Computations

E(t)/E(r) T-int/R-int	Avg
1.2316	1.2603
1.2488	S.D.
1.2728	0.0148
1.2630	Count
1.2690	7
1.2675	
1.2692	

Integration Limit display setup

	244	-773
	194	-797
	191	-768
	186	-743
	223	-745
	185	-739
	206	-825
Max/Min	244	-825

244	6	7.5
-825	6	7.5

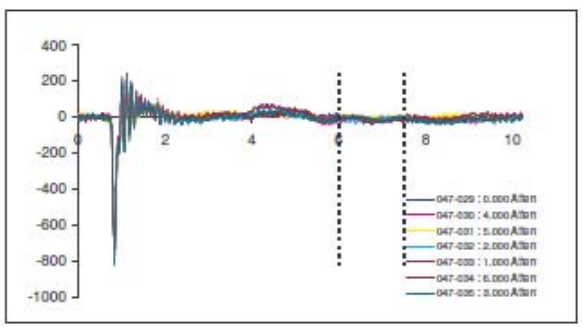

Figure A-5 Solvent wave data, with calculation of peak max, average baseline, and integral areas. The determined solvent E(t)/E(r) allows determination of the PAC absorbance (utilizing the PAC as a single-beam spectrophotometer for *in situ* absorbance measurements.) PAC absorbances for solvent data are fixed as 0.000. The portion from SPEC-A to the left (inclusive) is typically printed by the user and included in the hardcopy report.

Title:	=Master!C1
Experiment:	=Master!C2
Date Printed:	=TODAY()
Sample:	=Master!B19
Comments:	
	=IF(Master!C6=0,"",Master!C6)
Data Subset:	="0"&TEXT(Master!C3,0)

Solvent E(t)/E(r) = =TEXT(S18,"0.0000")&" ± "&TEXT(S20,"(

Integration Limits for R:	=Master!D9	=Master!E9	=TEXT((D11-C11+1)*0.05,"0.00")&S12
Integration Limits for T:	=Master!D10	=Master!E10	=TEXT((D12-C12+1)*0.05,"0.00")&S13
Integration Limits for S:	=Master!D11	=Master!E11	=TEXT((D13-C13+1)*0.01,"0.00")&S14
Pos/Neg:	=Master!D12		

Waves Excluded:

	Peak Max		
Filename:	R	T	S
=IF('Raw Data'!B2="","'(	=IF(B19="","',Peak Max'!C9)	=IF(B19="","',Peak Max'!C81)	=IF(B19="","',IF($C$14="Neg","',Peak Max'!C225,'Peak Max'!C153))
=IF('Raw Data'!E2="","'(	=IF(B20="","',Peak Max'!E9)	=IF(B20="","',Peak Max'!E81)	=IF(B20="","',IF($C$14="Neg","',Peak Max'!E225,'Peak Max'!E153))
=IF('Raw Data'!H2="","'(	=IF(B21="","',Peak Max'!G9)	=IF(B21="","',Peak Max'!G81)	=IF(B21="","',IF($C$14="Neg","',Peak Max'!G225,'Peak Max'!G153))
=IF('Raw Data'!K2="","'(	=IF(B22="","',Peak Max'!I9)	=IF(B22="","',Peak Max'!I81)	=IF(B22="","',IF($C$14="Neg","',Peak Max'!I225,'Peak Max'!I153))
=IF('Raw Data'!N2="","'(	=IF(B23="","',Peak Max'!K9)	=IF(B23="","',Peak Max'!K81)	=IF(B23="","',IF($C$14="Neg","',Peak Max'!K225,'Peak Max'!K153))
=IF('Raw Data'!Q2="","'(	=IF(B24="","',Peak Max'!M9)	=IF(B24="","',Peak Max'!M81)	=IF(B24="","',IF($C$14="Neg","',Peak Max'!M225,'Peak Max'!M153))
=IF('Raw Data'!T2="","'(	=IF(B25="","',Peak Max'!O9)	=IF(B25="","',Peak Max'!O81)	=IF(B25="","',IF($C$14="Neg","',Peak Max'!O225,'Peak Max'!O153))
Average	=AVERAGE(C19:C25)	=AVERAGE(D19:D25)	=AVERAGE(E19:E25)
S.D.	=STDEV(C19:C25)	=STDEV(D19:D25)	=STDEV(E19:E25)
Count	=COUNT(C19:C25)	=COUNT(D19:D25)	=COUNT(E19:E25)

# of Shots:	=Master!C5
Reference:	=Master!C4
Sample Absorbance:	=Master!C19

µs	Number of pre-trigger points =
µs	Number of pre-trigger points =
µs	Number of pre-trigger points =

Baseline		
R	T	S
=IF(B19="","',AVERAGE(OFFSET('Raw Data'!B3,0,0,J11,1)))	=IF(B19="","',AVERAGE(OFFSET('Raw Data'!B3,512,0,J12,1)))	=IF(B19="","',AVERAGE(OFFSET('Raw Data'!B3,1024,0,J13,1)))
=IF(B20="","',AVERAGE(OFFSET('Raw Data'!E3,0,0,J11,1)))	=IF(B20="","',AVERAGE(OFFSET('Raw Data'!E3,512,0,J12,1)))	=IF(B20="","',AVERAGE(OFFSET('Raw Data'!E3,1024,0,J13,1)))
=IF(B21="","',AVERAGE(OFFSET('Raw Data'!H3,0,0,J11,1)))	=IF(B21="","',AVERAGE(OFFSET('Raw Data'!H3,512,0,J12,1)))	=IF(B21="","',AVERAGE(OFFSET('Raw Data'!H3,1024,0,J13,1)))
=IF(B22="","',AVERAGE(OFFSET('Raw Data'!K3,0,0,J11,1)))	=IF(B22="","',AVERAGE(OFFSET('Raw Data'!K3,512,0,J12,1)))	=IF(B22="","',AVERAGE(OFFSET('Raw Data'!K3,1024,0,J13,1)))
=IF(B23="","',AVERAGE(OFFSET('Raw Data'!N3,0,0,J11,1)))	=IF(B23="","',AVERAGE(OFFSET('Raw Data'!N3,512,0,J12,1)))	=IF(B23="","',AVERAGE(OFFSET('Raw Data'!N3,1024,0,J13,1)))
=IF(B24="","',AVERAGE(OFFSET('Raw Data'!Q3,0,0,J11,1)))	=IF(B24="","',AVERAGE(OFFSET('Raw Data'!Q3,512,0,J12,1)))	=IF(B24="","',AVERAGE(OFFSET('Raw Data'!Q3,1024,0,J13,1)))
=IF(B25="","',AVERAGE(OFFSET('Raw Data'!T3,0,0,J11,1)))	=IF(B25="","',AVERAGE(OFFSET('Raw Data'!T3,512,0,J12,1)))	=IF(B25="","',AVERAGE(OFFSET('Raw Data'!T3,1024,0,J13,1)))
=AVERAGE(F19:F25)	=AVERAGE(G19:G25)	=AVERAGE(H19:H25)
=STDEV(F19:F25)	=STDEV(G19:G25)	=STDEV(H19:H25)
=COUNT(F19:F25)	=COUNT(G19:G25)	=COUNT(H19:H25)

Continued

Figure A-6 Calculations for Figure A-5

Calculation of E(t)/E(r) (if the solvent data was collected)

Spreadsheet Computations

S	PAC-A	SPEC-A	E(t)/E(r) T-int/R-int
=IF(B19="","",(ABS((SUM(OFFSET('Raw Data'!D3,($C$13+1024),0,($D$13-$C$13+1),1)))/$H$3)))	=IF(B19="","",0)	=IF(B19="","",$H$5)	=IF(B19="","",J19/I19)
=IF(B20="","",(ABS((SUM(OFFSET('Raw Data'!G3,($C$13+1024),0,($D$13-$C$13+1),1)))/$H$3)))	=IF(B20="","",0)	=IF(B20="","",$H$5)	=IF(B20="","",J20/I20)
=IF(B21="","",(ABS((SUM(OFFSET('Raw Data'!J3,($C$13+1024),0,($D$13-$C$13+1),1)))/$H$3)))	=IF(B21="","",0)	=IF(B21="","",$H$5)	=IF(B21="","",J21/I21)
=IF(B22="","",(ABS((SUM(OFFSET('Raw Data'!M3,($C$13+1024),0,($D$13-$C$13+1),1)))/$H$3)))	=IF(B22="","",0)	=IF(B22="","",$H$5)	=IF(B22="","",J22/I22)
=IF(B23="","",(ABS((SUM(OFFSET('Raw Data'!P3,($C$13+1024),0,($D$13-$C$13+1),1)))/$H$3)))	=IF(B23="","",0)	=IF(B23="","",$H$5)	=IF(B23="","",J23/I23)
=IF(B24="","",(ABS((SUM(OFFSET('Raw Data'!S3,($C$13+1024),0,($D$13-$C$13+1),1)))/$H$3)))	=IF(B24="","",0)	=IF(B24="","",$H$5)	=IF(B24="","",J24/I24)
=IF(B25="","",ABS((SUM(OFFSET('Raw Data'!V3,($C$13+1024),0,($D$13-$C$13+1),1)))/$H$3))	=IF(B25="","",0)	=IF(B25="","",$H$5)	=IF(B25="","",J25/I25)
	=AVERAGE(L19:L25)	=AVERAGE(M19:M25)	
	=STDEV(L19:L25)	=STDEV(M19:M25)	
	=COUNT(L19:L25)	=COUNT(M19:M25)	

Max/Min

=AVERAGE(R18:R24)	Avg
=STDEV(R18:R24)	S.D.
=COUNT(R18:R24)	Count

Integration Limit display setup

=IF('Raw Data'!B2="","",(MAX(OFFSET('Raw Data'!B1027,0,2,1024,1))))	=IF('Raw Data'!B2="","",(MIN(OFFSET('Raw Data'!B1027,0,2,1024,1))))	
=IF('Raw Data'!E2="","",(MAX(OFFSET('Raw Data'!E1027,0,2,1024,1))))	=IF('Raw Data'!E2="","",(MIN(OFFSET('Raw Data'!E1027,0,2,1024,1))))	
=IF('Raw Data'!H2="","",(MAX(OFFSET('Raw Data'!H1027,0,2,1024,1))))	=IF('Raw Data'!H2="","",(MIN(OFFSET('Raw Data'!H1027,0,2,1024,1))))	
=IF('Raw Data'!K2="","",(MAX(OFFSET('Raw Data'!K1027,0,2,1024,1))))	=IF('Raw Data'!K2="","",(MIN(OFFSET('Raw Data'!K1027,0,2,1024,1))))	
=IF('Raw Data'!N2="","",(MAX(OFFSET('Raw Data'!N1027,0,2,1024,1))))	=IF('Raw Data'!N2="","",(MIN(OFFSET('Raw Data'!N1027,0,2,1024,1))))	
=IF('Raw Data'!Q2="","",(MAX(OFFSET('Raw Data'!Q1027,0,2,1024,1))))	=IF('Raw Data'!Q2="","",(MIN(OFFSET('Raw Data'!Q1027,0,2,1024,1))))	
=IF('Raw Data'!T2="","",(MAX(OFFSET('Raw Data'!T1027,0,2,1024,1))))	=IF('Raw Data'!T2="","",(MIN(OFFSET('Raw Data'!T1027,0,2,1024,1))))	
=MAX(S27:S33)	=MIN(T27:T33)	
=S34	=C13/100	=D13/100
=T34	=C13/100	=D13/100

Figure A-6 (con't)

Title: CpMn(CO)3/octane
Experiment: XXXIV.1-047
Date Printed: 28-Sep-2005 # of Shots: 30
Sample: Fer/octane Reference: Fer/ACN
Comments: Sample Absorbance: 0.221

Data Subset: 047a

Solvent E(t)/E(r) = 1.2603 ± 0.0148 (1.2%; n = 7)

Integration Limits for R:	330	360	1.55 µs	Number of pre-trigger points =	280
Integration Limits for T:	200	230	1.55 µs	Number of pre-trigger points =	140
Integration Limits for S:	600	750	1.51 µs	Number of pre-trigger points =	70
Pos/Neg:	Neg				

Waves Excluded:

	Peak Max			Baseline			Integrals				
Filename:	R	T	S	R	T	S	R	T	S	PAC-A	SPEC-A
047-001	349	216	672	1322	1223	6805	2219	1646	26917	0.230	0.221
047-002	350	216	675	1307	1225	6787	1042	778	12363	0.227	0.221
047-003	349	217	673	1289	1232	6806	1559	1160	18674	0.229	0.221
047-004	349	217	676	1318	1219	6809	1244	925	14813	0.229	0.221
047-005	350	217	679	1316	1222	6822	1099	821	13209	0.227	0.221
047-006	349	218	673	1334	1225	6830	1417	1053	17024	0.230	0.221
047-007	350	216	673	1296	1219	6838	1735	1304	21269	0.224	0.221
Average	349	217	674	1312	1224	6814				0.228	0.221
S.D.	1	1	2	16	5	17				0.002	0.000
Count	7	7	7	7	7	7				7	7

		E(r)					
	Y-Value	Slope	Y-Int	% Error in Slope	S.D. in Int	R^2	Number
Automatic Inclusion of (0,0)	$S/(1-T_s)$	30.5670	-400.13	1.82%	791.12	0.9996	8
	$S/(1-T_{pbar})$	29.8388	-390.60	1.82%	772.27	0.9996	8
	$S/(1-T_p)$	29.7687	-308.60	1.79%	760.36	0.9996	8
	S	12.1909	-159.58	1.82%	315.52	0.9996	8
Automatic Exclusion of (0,0)	$S/(1-T_s)$	31.1490	-1,314.79	9.12%	4,322.90	0.9993	7
	$S/(1-T_{pbar})$	30.4069	-1,283.47	9.12%	4,219.91	0.9993	7
	$S/(1-T_p)$	30.2175	-1,014.01	7.50%	3,450.29	0.9993	7
	S	12.4230	-524.37	9.12%	1,724.09	0.9993	7

Results of plotted regressions – values from top row ((0,0) included, spectrometer abs) are typically used. Other results allow comparison with *in situ* absorbance measurements (typically lower quality, but allows interpretation of results if spec. abs. is mis-measured or has changed.)

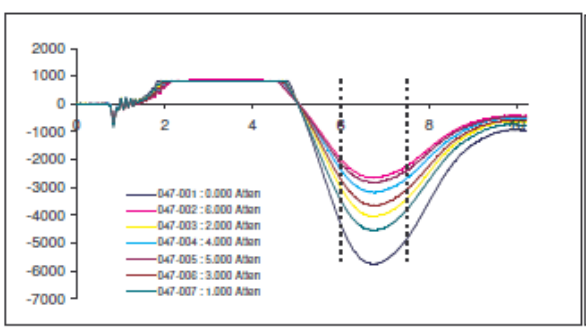

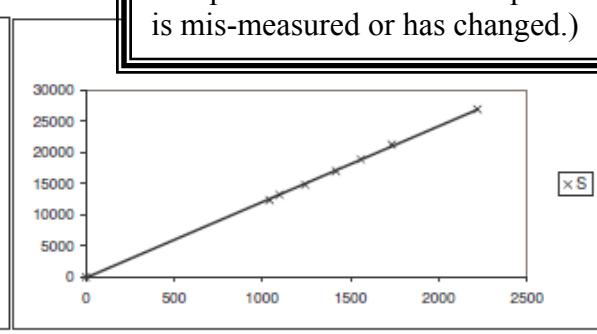

Figure A-7 Sample data for the first run (i.e. data for one sample at various E_p; E_p is called E(r) in this spreadsheet for historical reasons), including the measured peak max, average baseline, and integral areas. It is representative of the other 5 available 'run' tabs. This portion is typically printed by the user and included in the hardcopy report. PAC absorbance is reported for each sample, and the least squares fitting results for *S/(1-T)* vs. E_p are displayed (slope = κf_h^{obs}). Calculations for the portion displayed above, as well as preceding calculations (not shown above) are shown on the next pages.

Title:	=Master!C1
Experiment:	=Master!C2
Date Printed:	=TODAY()
Sample:	=Master!B20
Comments:	=IF(Master!C6=0,"",Master!C6)
Data Subset:	="0"&TEXT(Master!C3,0)&"a"

Solvent E(t)/E(r) = =Solvent!C9

Integration Limits for R:	=Master!D9	=Master!E9	=TEXT((D11-C11+1)*0.05,"0.00")&S12 µs
Integration Limits for T:	=Master!D10	=Master!E10	=TEXT((D12-C12+1)*0.05,"0.00")&S13 µs
Integration Limits for S:	=Master!D11	=Master!E11	=TEXT((D13-C13+1)*0.01,"0.00")&S14 µs
Pos/Neg:	=Master!D12		

Waves Excluded:

Filename:	R	T	S	R
=IF('Raw Data'!W2="","","Raw Data'!W2)	=IF(B19="","","Peak Max'!Q9)	=IF(B19="","","Peak Max'!Q81)	=IF(B19="","",IF($C$14="Neg","Peak Max'!Q225,"Peak Max'!Q153))	=IF(B19="","",AVERAGE(OFFSET('Raw Data'!W3,0,0,J11,1)))
=IF('Raw Data'!Z2="","","Raw Data'!Z2)	=IF(B20="","","Peak Max'!S9)	=IF(B20="","","Peak Max'!S81)	=IF(B20="","",IF($C$14="Neg","Peak Max'!S225,"Peak Max'!S153))	=IF(B20="","",AVERAGE(OFFSET('Raw Data'!Z3,0,0,J11,1)))
=IF('Raw Data'!AC2="","","Raw Data'!AC2)	=IF(B21="","","Peak Max'!U9)	=IF(B21="","","Peak Max'!U81)	=IF(B21="","",IF($C$14="Neg","Peak Max'!U225,"Peak Max'!U153))	=IF(B21="","",AVERAGE(OFFSET('Raw Data'!AC3,0,0,J11,1)))
=IF('Raw Data'!AF2="","","Raw Data'!AF2)	=IF(B22="","","Peak Max'!W9)	=IF(B22="","","Peak Max'!W81)	=IF(B22="","",IF($C$14="Neg","Peak Max'!W225,"Peak Max'!W153))	=IF(B22="","",AVERAGE(OFFSET('Raw Data'!AF3,0,0,J11,1)))
=IF('Raw Data'!AI2="","","Raw Data'!AI2)	=IF(B23="","","Peak Max'!Y9)	=IF(B23="","","Peak Max'!Y81)	=IF(B23="","",IF($C$14="Neg","Peak Max'!Y225,"Peak Max'!Y153))	=IF(B23="","",AVERAGE(OFFSET('Raw Data'!AI3,0,0,J11,1)))
=IF('Raw Data'!AL2="","","Raw Data'!AL2)	=IF(B24="","","Peak Max'!AA9)	=IF(B24="","","Peak Max'!AA81)	=IF(B24="","",IF($C$14="Neg","Peak Max'!AA225,"Peak Max'!AA153))	=IF(B24="","",AVERAGE(OFFSET('Raw Data'!AL3,0,0,J11,1)))
=IF('Raw Data'!AO2="","","Raw Data'!AO2)	=IF(B25="","","Peak Max'!AC9)	=IF(B25="","","Peak Max'!AC81)	=IF(B25="","",IF($C$14="Neg","Peak Max'!AC225,"Peak Max'!AC153))	=IF(B25="","",AVERAGE(OFFSET('Raw Data'!AO3,0,0,J11,1)))
Average	=AVERAGE(C19:C25)	=AVERAGE(D19:D25)	=AVERAGE(E19:E25)	=AVERAGE(F19:F25)
S.D.	=STDEV(C19:C25)	=STDEV(D19:D25)	=STDEV(E19:E25)	=STDEV(F19:F25)
Count	=COUNT(C19:C25)	=COUNT(D19:D25)	=COUNT(E19:E25)	=COUNT(F19:F25)

	Y-Value	Slope	Y-Int	% Error in Slope	E(r) S.D. in Int
Automatic Inclusion of (0,0)	$S/(1-T_a)$	=AH22	=AH23	=AH27	=AH28
	$S/(1-T_{char})$	=AJ22	=AJ23	=AJ27	=AJ28
	$S/(1-T_p)$	=AL22	=AL23	=AL27	=AL28
	S	=AN22	=AN23	=AN27	=AN28
Automatic Exclusion of (0,0)	$S/(1-T_a)$	=AH46	=AH47	=AH51	=AH52
	$S/(1-T_{char})$	=AJ46	=AJ47	=AJ51	=AJ52
	$S/(1-T_p)$	=AL46	=AL47	=AL51	=AL52
	S	=AN46	=AN47	=AN51	=AN52

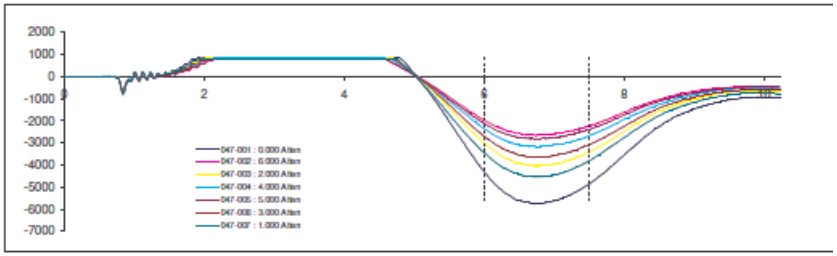

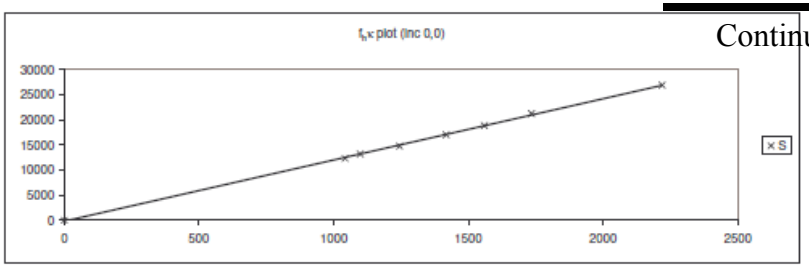

Continued

Figure A-8 Calculations from Figure A-7

# of Shots: =MasterIC5
Reference: =MasterIC4
Sample Absorbance: =MasterIC20

Number of pre-trigger points =
Number of pre-trigger points =
Number of pre-trigger points =

=MasterIF9
=MasterIF10
=MasterIF11

Baseline			Integrals
T	S	R	T
=IF(B19="","",AVERAGE(OFFSET('Raw Data'!W3,512,0,J12,1)))	=IF(B19="","",AVERAGE(OFFSET('Raw Data'!W3,1024,0,J13,1)))	/(OFFSET('Raw Data'!W3,$C$11,2,($D$11-$C$11+1),1)))/$H$3))	=IF(B19="","",((SUM(OFFSET('Raw Data'!W3,($C$12+512),2,($D$12-$C$12+1),1)))/$H$3))
=IF(B20="","",AVERAGE(OFFSET('Raw Data'!Z3,512,0,J12,1)))	=IF(B20="","",AVERAGE(OFFSET('Raw Data'!Z3,1024,0,J13,1)))	/(OFFSET('Raw Data'!Z3,$C$11,2,($D$11-$C$11+1),1)))/$H$3))	=IF(B20="","",((SUM(OFFSET('Raw Data'!Z3,($C$12+512),2,($D$12-$C$12+1),1)))/$H$3))
=IF(B21="","",AVERAGE(OFFSET('Raw Data'!AC3,512,0,J12,1)))	=IF(B21="","",AVERAGE(OFFSET('Raw Data'!AC3,1024,0,J13,1)))	/(OFFSET('Raw Data'!AC3,$C$11,2,($D$11-$C$11+1),1)))/$H$3))	=IF(B21="","",((SUM(OFFSET('Raw Data'!AC3,($C$12+512),2,($D$12-$C$12+1),1)))/$H$3))
=IF(B22="","",AVERAGE(OFFSET('Raw Data'!AF3,512,0,J12,1)))	=IF(B22="","",AVERAGE(OFFSET('Raw Data'!AF3,1024,0,J13,1)))	/(OFFSET('Raw Data'!AF3,$C$11,2,($D$11-$C$11+1),1)))/$H$3))	=IF(B22="","",((SUM(OFFSET('Raw Data'!AF3,($C$12+512),2,($D$12-$C$12+1),1)))/$H$3))
=IF(B23="","",AVERAGE(OFFSET('Raw Data'!AI3,512,0,J12,1)))	=IF(B23="","",AVERAGE(OFFSET('Raw Data'!AI3,1024,0,J13,1)))	/(OFFSET('Raw Data'!AI3,$C$11,2,($D$11-$C$11+1),1)))/$H$3))	=IF(B23="","",((SUM(OFFSET('Raw Data'!AI3,($C$12+512),2,($D$12-$C$12+1),1)))/$H$3))
=IF(B24="","",AVERAGE(OFFSET('Raw Data'!AL3,512,0,J12,1)))	=IF(B24="","",AVERAGE(OFFSET('Raw Data'!AL3,1024,0,J13,1)))	/(OFFSET('Raw Data'!AL3,$C$11,2,($D$11-$C$11+1),1)))/$H$3))	=IF(B24="","",((SUM(OFFSET('Raw Data'!AL3,($C$12+512),2,($D$12-$C$12+1),1)))/$H$3))
=IF(B25="","",AVERAGE(OFFSET('Raw Data'!AO3,512,0,J12,1)))	=IF(B25="","",AVERAGE(OFFSET('Raw Data'!AO3,1024,0,J13,1)))	/(OFFSET('Raw Data'!AO3,$C$11,2,($D$11-$C$11+1),1)))/$H$3))	=IF(B25="","",((SUM(OFFSET('Raw Data'!AO3,($C$12+512),2,($D$12-$C$12+1),1)))/$H$3))
=AVERAGE(G19:G25)	=AVERAGE(H19:H25)		
=STDEV(G19:G25)	=STDEV(H19:H25)		
=COUNT(G19:G25)	=COUNT(H19:H25)		

R^2	Number
=RSQ(K19:K26,I19:I26)	=COUNT(K19:K26)
=RSQ(K19:K26,I19:I26)	=COUNT(K19:K26)
=RSQ(K19:K26,I19:I26)	=COUNT(K19:K26)
=RSQ(K19:K26,I19:I26)	=COUNT(K19:K26)
=RSQ(K19:K25,I19:I25)	=COUNT(K19:K25)
=RSQ(K19:K25,I19:I25)	=COUNT(K19:K25)
=RSQ(K19:K25,I19:I25)	=COUNT(K19:K25)
=RSQ(K19:K25,I19:I25)	=COUNT(K19:K25)

Results of plotted regressions – values from top row ((0,0) included, spectrometer abs) are typically used. Other results allow comparison with *in situ* absorbance measurements (typically lower quality, but allows interpretation of results if spec. abs. is mis-measured or has changed.)

S	PAC-A	SPEC-A
=IF(B19="","",(ABS((SUM(OFFSET('Raw Data'!W3,($C$13+1024),2,($D$13-$C$13+1),1)))/$H$3)))	=IF(B19="","",LOG(I19*Solvent!$S$18/J19))	=IF(B19="","",$H$5)
=IF(B20="","",(ABS((SUM(OFFSET('Raw Data'!Z3,($C$13+1024),2,($D$13-$C$13+1),1)))/$H$3)))	=IF(B20="","",LOG(I20*Solvent!$S$18/J20))	=IF(B20="","",$H$5)
=IF(B21="","",(ABS((SUM(OFFSET('Raw Data'!AC3,($C$13+1024),2,($D$13-$C$13+1),1)))/$H$3)))	=IF(B21="","",LOG(I21*Solvent!$S$18/J21))	=IF(B21="","",$H$5)
=IF(B22="","",(ABS((SUM(OFFSET('Raw Data'!AF3,($C$13+1024),2,($D$13-$C$13+1),1)))/$H$3)))	=IF(B22="","",LOG(I22*Solvent!$S$18/J22))	=IF(B22="","",$H$5)
=IF(B23="","",(ABS((SUM(OFFSET('Raw Data'!AI3,($C$13+1024),2,($D$13-$C$13+1),1)))/$H$3)))	=IF(B23="","",LOG(I23*Solvent!$S$18/J23))	=IF(B23="","",$H$5)
=IF(B24="","",(ABS((SUM(OFFSET('Raw Data'!AL3,($C$13+1024),2,($D$13-$C$13+1),1)))/$H$3)))	=IF(B24="","",LOG(I24*Solvent!$S$18/J24))	=IF(B24="","",$H$5)
=IF(B25="","",(ABS((SUM(OFFSET('Raw Data'!AO3,($C$13+1024),2,($D$13-$C$13+1),1)))/$H$3)))	=IF(B25="","",LOG(I25*Solvent!$S$18/J25))	=IF(B25="","",$H$5)
	=AVERAGE(L19:L25)	=AVERAGE(M19:M25)
	=STDEV(L19:L25)	=STDEV(M19:M25)
	=COUNT(L19:L25)	=COUNT(M19:M25)

Continued

Figure A-8 (Con't)

Plot regression for S/(1-T_a), S/(1-T_{PAC}), S/(1-T_{PACavg}), and S vs. R-integral, Calculate m ± S.D., b ± S.D., and R^2 for S vs. R normalization plots - with/without (0,0) pt included

R Integral	S/(1-T_a)	S/(1-T_{pbar})	S/(1-T_p)	S Integral
=IF(B19="","",I19)	=IF(B19="","",(K19/(1-(10^-M19))))	=IF(B19="","",K19/(1-(10^-$L$26)))	=IF(B19="","",(K19/(1-(10^-L19))))	=K19
=IF(B20="","",I20)	=IF(B20="","",(K20/(1-(10^-M20))))	=IF(B20="","",K20/(1-(10^-$L$26)))	=IF(B20="","",(K20/(1-(10^-L20))))	=K20
=IF(B21="","",I21)	=IF(B21="","",(K21/(1-(10^-M21))))	=IF(B21="","",K21/(1-(10^-$L$26)))	=IF(B21="","",(K21/(1-(10^-L21))))	=K21
=IF(B22="","",I22)	=IF(B22="","",(K22/(1-(10^-M22))))	=IF(B22="","",K22/(1-(10^-$L$26)))	=IF(B22="","",(K22/(1-(10^-L22))))	=K22
=IF(B23="","",I23)	=IF(B23="","",(K23/(1-(10^-M23))))	=IF(B23="","",K23/(1-(10^-$L$26)))	=IF(B23="","",(K23/(1-(10^-L23))))	=K23
=IF(B24="","",I24)	=IF(B24="","",(K24/(1-(10^-M24))))	=IF(B24="","",K24/(1-(10^-$L$26)))	=IF(B24="","",(K24/(1-(10^-L24))))	=K24
=IF(B25="","",I25)	=IF(B25="","",(K25/(1-(10^-M25))))	=IF(B25="","",K25/(1-(10^-$L$26)))	=IF(B25="","",(K25/(1-(10^-L25))))	=K25
0	0	0	0	0
$(R\ Integral)^2$	$(S/(1-T_a))^2$	$(S/(1-T_{pbar}))^2$	$(S/(1-T_p))^2$	$S\text{-}int^2$
=IF(B19="","",AA17^2)	=IF(C19="","",AB17^2)	=IF(D19="","",AC17^2)	=IF(E19="","",AD17^2)	=IF(F19="","",AE17^2)
=IF(B20="","",AA18^2)	=IF(C20="","",AB18^2)	=IF(D20="","",AC18^2)	=IF(E20="","",AD18^2)	=IF(F20="","",AE18^2)
=IF(B21="","",AA19^2)	=IF(C21="","",AB19^2)	=IF(D21="","",AC19^2)	=IF(E21="","",AD19^2)	=IF(F21="","",AE19^2)
=IF(B22="","",AA20^2)	=IF(C22="","",AB20^2)	=IF(D22="","",AC20^2)	=IF(E22="","",AD20^2)	=IF(F22="","",AE20^2)
=IF(B23="","",AA21^2)	=IF(C23="","",AB21^2)	=IF(D23="","",AC21^2)	=IF(E23="","",AD21^2)	=IF(F23="","",AE21^2)
=IF(B24="","",AA22^2)	=IF(C24="","",AB22^2)	=IF(D24="","",AC22^2)	=IF(E24="","",AD22^2)	=IF(F24="","",AE22^2)
=IF(B25="","",AA23^2)	=IF(C25="","",AB23^2)	=IF(D25="","",AC23^2)	=IF(E25="","",AD23^2)	=IF(F25="","",AE23^2)
=AA24^2	0	0	0	0
	(R-int)(S/(1-T_a))	(R-int)(S/(1-T_{pbar}))	(R-int)(S/(1-T_p))	(R-int)(S-Int)
	=IF(B19="","",$AA17*AB17)	=IF(C19="","",$AA17*AC17)	=IF(D19="","",$AA17*AD17)	=IF(E19="","",$AA17*AE17)
	=IF(B20="","",$AA18*AB18)	=IF(C20="","",$AA18*AC18)	=IF(D20="","",$AA18*AD18)	=IF(E20="","",$AA18*AE18)
	=IF(B21="","",$AA19*AB19)	=IF(C21="","",$AA19*AC19)	=IF(D21="","",$AA19*AD19)	=IF(E21="","",$AA19*AE19)
	=IF(B22="","",$AA20*AB20)	=IF(C22="","",$AA20*AC20)	=IF(D22="","",$AA20*AD20)	=IF(E22="","",$AA20*AE20)
	=IF(B23="","",$AA21*AB21)	=IF(C23="","",$AA21*AC21)	=IF(D23="","",$AA21*AD21)	=IF(E23="","",$AA21*AE21)
	=IF(B24="","",$AA22*AB22)	=IF(C24="","",$AA22*AC22)	=IF(D24="","",$AA22*AD22)	=IF(E24="","",$AA22*AE22)
	=IF(B25="","",$AA23*AB23)	=IF(C25="","",$AA23*AC23)	=IF(D25="","",$AA23*AD23)	=IF(E25="","",$AA23*AE23)
	=$AA24*AB24	=$AA24*AC24	=$AA24*AD24	=$AA24*AE24

Continued

Figure A-8 (Con't)

inc (0,0))	S/(1-T_p) (inc (0,0))		S (inc (0,0))	
=SUM($AA17:$AA24)	sx	=SUM($AA17:$AA24)	sx	=SUM($AA17:$AA24)
=SUM(AC17:AC24)	sy	=SUM(AD17:AD24)	sy	=SUM(AE17:AE24)
=SUM($AA26:$AA33)	sx2	=SUM($AA26:$AA33)	sx2	=SUM($AA26:$AA33)
=SUM(AC26:AC33)	sy2	=SUM(AD26:AD33)	sy2	=SUM(AE26:AE33)
=SUM(AC35:AC42)	sxy	=SUM(AD35:AD42)	sxy	=SUM(AE35:AE42)
=$H$33*AJ18-AJ16^2	local1	=$H$34*AL18-AL16^2	local1	=$H$35*AN18-AN16^2
=($H$33*AJ20-AJ16*AJ17)/AJ21	m	=($H$34*AL20-AL16*AL17)/AL21	m	=($H$35*AN20-AN16*AN17)/AN21
=(AJ17*AJ18-AJ16*AJ20)/AJ21	b	=(AL17*AL18-AL16*AL20)/AL21	b	=(AN17*AN18-AN16*AN20)/AN21
=SUM(AJ30:AJ37)	local3	=SUM(AL30:AL37)	local3	=SUM(AN30:AN37)
=AJ24/($H$33-1)	vary2	=AL24/($H$34-1)	vary2	=AN24/($H$35-1)
=SQRT(AJ25/(AJ18-(AJ16^2/$H$33)))	error in slope	=SQRT(AL25/(AL18-(AL16^2/$H$34)))	error in slope	=SQRT(AN25/(AN18-(AN16^2/$H$35)))
=AJ26/AJ22	% error slope	=AL26/AL22	% error slope	=AN26/AN22
=SQRT((AJ25*AJ18)/($H$33*AJ18-AJ16^2))	error in b	=SQRT((AL25*AL18)/($H$34*AL18-AL16^2))	error in b	=SQRT((AN25*AN18)/($H$35*AN18-AN16^2))
$\Sigma(y-m^2x+b)$	Local 2 - Sum(y-m^{2}x+b)		Local 2 - Sum(y-m^{2}x+b)	
=IF(B19="","",AI30^2)	=IF(B19="","",(AD17-$AL$22*$AA17+$AL$23))	=IF(B19="","",AK30^2)	=IF(B19="","",(AE17-$AN$22*$AA17+$AN$23))	=IF(B19="","",AM30^2)
=IF(B20="","",AI31^2)	=IF(B20="","",(AD18-$AL$22*$AA18+$AL$23))	=IF(B20="","",AK31^2)	=IF(B20="","",(AE18-$AN$22*$AA18+$AN$23))	=IF(B20="","",AM31^2)
=IF(B21="","",AI32^2)	=IF(B21="","",(AD19-$AL$22*$AA19+$AL$23))	=IF(B21="","",AK32^2)	=IF(B21="","",(AE19-$AN$22*$AA19+$AN$23))	=IF(B21="","",AM32^2)
=IF(B22="","",AI33^2)	=IF(B22="","",(AD20-$AL$22*$AA20+$AL$23))	=IF(B22="","",AK33^2)	=IF(B22="","",(AE20-$AN$22*$AA20+$AN$23))	=IF(B22="","",AM33^2)
=IF(B23="","",AI34^2)	=IF(B23="","",(AD21-$AL$22*$AA21+$AL$23))	=IF(B23="","",AK34^2)	=IF(B23="","",(AE21-$AN$22*$AA21+$AN$23))	=IF(B23="","",AM34^2)
=IF(B24="","",AI35^2)	=IF(B24="","",(AD22-$AL$22*$AA22+$AL$23))	=IF(B24="","",AK35^2)	=IF(B24="","",(AE22-$AN$22*$AA22+$AN$23))	=IF(B24="","",AM35^2)
=IF(B25="","",AI36^2)	=IF(B25="","",(AD23-$AL$22*$AA23+$AL$23))	=IF(B25="","",AK36^2)	=IF(B25="","",(AE23-$AN$22*$AA23+$AN$23))	=IF(B25="","",AM36^2)
=IF(B26="","",AI37^2)	=IF(B26="","",(AD24-$AL$22*$AA24+$AL$23))	=IF(B26="","",AK37^2)	=IF(B26="","",(AE24-$AN$22*$AA24+$AN$23))	=IF(B26="","",AM37^2)

exc (0,0))	S/(1-Tp) (exc (0,0))		S (exc (0,0))	
=SUM($AA17:$AA23)	sx	=SUM($AA17:$AA23)	sx	=SUM($AA17:$AA23)
=SUM(AC17:AC23)	sy	=SUM(AD17:AD23)	sy	=SUM(AE17:AE23)
=SUM($AA26:$AA32)	sx2	=SUM($AA26:$AA32)	sx2	=SUM($AA26:$AA32)
=SUM(AC26:AC32)	sy2	=SUM(AD26:AD32)	sy2	=SUM(AE26:AE32)
=SUM(AC35:AC41)	sxy	=SUM(AD35:AD41)	sxy	=SUM(AE35:AE41)
=$H$37*AJ42-AJ40^2	local1	=$H$38*AL42-AL40^2	local1	=$H$39*AN42-AN40^2
=($H$37*AJ44-AJ40*AJ41)/AJ45	m	=($H$38*AL44-AL40*AL41)/AL45	m	=($H$39*AN44-AN40*AN41)/AN45
=(AJ41*AJ42-AJ40*AJ44)/AJ45	b	=(AL41*AL42-AL40*AL44)/AL45	b	=(AN41*AN42-AN40*AN44)/AN45
=SUM(AJ54:AJ60)	local3	=SUM(AL54:AL60)	local3	=SUM(AN54:AN60)
=AJ48/($H$37-1)	vary2	=AL48/($H$38-1)	vary2	=AN48/($H$39-1)
=SQRT(AJ49/(AJ42-(AJ40^2/$H$37)))	error in slope	=SQRT(AL49/(AL42-(AL40^2/$H$38)))	error in slope	=SQRT(AN49/(AN42-(AN40^2/$H$39)))
=AJ50/AJ46	% error slope	=AL50/AL46	% error slope	=AN50/AN46
=SQRT((AJ49*AJ42)/($H$37*AJ42-AJ40^2))	error in b	=SQRT((AL49*AL42)/($H$38*AL42-AL40^2))	error in b	=SQRT((AN49*AN42)/($H$39*AN42-AN40^2))
$\Sigma(y-m^2x+b)$	Local 2 - Sum(y-m^{2}x+b)		Local 2 - Sum(y-m^{2}x+b)	
=IF(B19="","",AI54^2)	=IF(B19="","",(AD17-$AL$46*$AA17+$AL$47))	=IF(B19="","",AK54^2)	=IF(B19="","",(AE17-$AN$46*$AA17+$AN$47))	=IF(B19="","",AM54^2)
=IF(B20="","",AI55^2)	=IF(B20="","",(AD18-$AL$46*$AA18+$AL$47))	=IF(B20="","",AK55^2)	=IF(B20="","",(AE18-$AN$46*$AA18+$AN$47))	=IF(B20="","",AM55^2)
=IF(B21="","",AI56^2)	=IF(B21="","",(AD19-$AL$46*$AA19+$AL$47))	=IF(B21="","",AK56^2)	=IF(B21="","",(AE19-$AN$46*$AA19+$AN$47))	=IF(B21="","",AM56^2)
=IF(B22="","",AI57^2)	=IF(B22="","",(AD20-$AL$46*$AA20+$AL$47))	=IF(B22="","",AK57^2)	=IF(B22="","",(AE20-$AN$46*$AA20+$AN$47))	=IF(B22="","",AM57^2)
=IF(B23="","",AI58^2)	=IF(B23="","",(AD21-$AL$46*$AA21+$AL$47))	=IF(B23="","",AK58^2)	=IF(B23="","",(AE21-$AN$46*$AA21+$AN$47))	=IF(B23="","",AM58^2)
=IF(B24="","",AI59^2)	=IF(B24="","",(AD22-$AL$46*$AA22+$AL$47))	=IF(B24="","",AK59^2)	=IF(B24="","",(AE22-$AN$46*$AA22+$AN$47))	=IF(B24="","",AM59^2)
=IF(B25="","",AI60^2)	=IF(B25="","",(AD23-$AL$46*$AA23+$AL$47))	=IF(B25="","",AK60^2)	=IF(B25="","",(AE23-$AN$46*$AA23+$AN$47))	=IF(B25="","",AM60^2)

Figure A-8 (Con't)

Attenuation to Plot: 0.000

									0.000	0.000 Atten		a	b	c	d	e	f	Overall		
				Time	Solvent	047a	047b	047c	047d		Max	845.343	814.886	833.886	821.957	0.000	0.000	845	6.00	7.50
Solvent		0.000	1	0	14.671	-12.657	-1.114	-6.114	1.957		Min	-5756.657	-3395.114	-5462.114	-3369.043	0.000	0.000	-5757	6.00	7.50
	1	4.000	2	0.01	8.671	-11.657	-15.114	-2.114	9.957											
		5.000	3	0.02	10.671	-21.657	-12.114	-8.114	10.957											
		2.000	4	0.03	0.671	-17.657	-6.114	2.886	11.957											
		1.000	5	0.04	-9.329	-17.657	10.886	-3.114	12.957											
		6.000	6	0.05	-12.329	-10.657	0.886	1.886	1.957											
		3.000	7	0.06	3.671	-12.657	1.886	-10.114	1.957											
				0.07	5.671	1.343	1.886	-7.114	-0.043											
a		0.000	1	0.08	5.671	0.343	9.886	-23.114	-2.043											
	1	6.000	2	0.09	2.671	4.343	10.886	-7.114	-3.043											
		2.000	3	0.1	1.671	-8.657	4.886	-11.114	4.957											
		4.000	4	0.11	9.671	2.343	-4.114	-10.114	7.957											
		5.000	5	0.12	-0.329	-7.657	-7.114	-22.114	9.957											
		3.000	6	0.13	6.671	-7.657	-4.114	-20.114	14.957											
		1.000	7	0.14	10.671	-22.657	-11.114	-21.114	13.957											
				0.15	13.671	-15.657	-1.114	-16.114	24.957											
b		1.000	1	0.16	14.671	-17.657	-15.114	-6.114	6.957											
	7	4.000	2	0.17	-1.329	-15.657	-17.114	-14.114	9.957											
		3.000	3	0.18	-0.329	-14.657	-16.114	-14.114	8.957											
		2.000	4	0.19	3.671	-7.657	-2.114	-6.114	5.957											
		5.000	5	0.2	3.671	-7.657	4.886	-4.114	-7.043											
		6.000	6	0.21	-5.329	-7.657	8.886	-4.114	-9.043											
		0.000	7	0.22	11.671	-8.657	2.886	-10.114	-13.043											
				0.23	2.671	0.343	6.886	-14.114	-19.043											
c		0.000	1	0.24	-3.329	8.343	16.886	-19.114	-6.043											
	1	5.000	2	0.25	-7.329	8.343	10.886	-10.114	-10.043											
		3.000	3	0.26	-1.329	-14.657	5.886	-11.114	-11.043											
		2.000	4	0.27	4.671	-4.657	-0.114	-7.114	3.957											
		4.000	5	0.28	5.671	-7.657	-8.114	-3.114	4.957											
		1.000	6	0.29	0.671	1.343	-5.114	-0.114	9.957											
		6.000	7	0.3	-0.329	-10.657	2.886	8.886	10.957											
				0.31	5.671	1.343	-0.114	2.886	3.957											
d		6.000	1	0.32	-2.329	-4.657	2.886	6.886	-2.043											
	7	2.000	2	0.33	-4.329	-2.657	-0.114	0.886	-0.043											
		4.000	3	0.34	3.671	1.343	-8.114	0.886	-3.043											
		3.000	4	0.35	0.671	2.343	7.886	-6.114	0.957											
		1.000	5	0.36	6.671	11.343	13.886	-3.114	-11.043											
		5.000	6	0.37	-6.329	7.343	8.886	-1.114	-15.043											
		0.000	7	0.38	1.671	0.343	-4.114	3.886	-18.043											
				0.39	-5.329	7.343	7.886	3.886	-16.043											
e		0.000	1	0.4	2.671	9.343	7.886	2.886	-18.043											
	1	0.000	2	0.41	-9.329	1.343	18.886	1.886	-10.043											
		0.000	3	0.42	2.671	1.343	-0.114	3.886	-3.043											

Figure A-9 This sheet allows waves of similar attenuation to be plotted together. Attenuations are not necessarily identical; since the absolute E_p does not matter in a photoacoustic measurement, there is commonly solution carryover between attenuator solutions, and the actual attenuation may vary considerably. The plot generated by this sheet is thus intended for illustrative purposes only, and should be corrected for Ep for publication-quality results.. The following pages show the expressions for the solvent and one sample wave as representative of all calculations of this type.

Attenuation to Plot: 0

			Time	Solvent
Solvent	=Master!X20	1	='Data Run Solvent'!A1027	=IF(Master!$B$19=0,"",OFFSET('Data Run Solvent'!A1027,0,$A$7,1,1))
=VLOOKUP(J4,B6:C12,2,0)	=Master!Y20	2	='Data Run Solvent'!A1028	=IF(Master!$B$19=0,"",OFFSET('Data Run Solvent'!A1028,0,$A$7,1,1))
	=Master!Z20	3	='Data Run Solvent'!A1029	=IF(Master!$B$19=0,"",OFFSET('Data Run Solvent'!A1029,0,$A$7,1,1))
	=Master!AA20	4	='Data Run Solvent'!A1030	=IF(Master!$B$19=0,"",OFFSET('Data Run Solvent'!A1030,0,$A$7,1,1))
	=Master!AB20	5	='Data Run Solvent'!A1031	=IF(Master!$B$19=0,"",OFFSET('Data Run Solvent'!A1031,0,$A$7,1,1))
	=Master!AC20	6	='Data Run Solvent'!A1032	=IF(Master!$B$19=0,"",OFFSET('Data Run Solvent'!A1032,0,$A$7,1,1))
	=Master!AD20	7	='Data Run Solvent'!A1033	=IF(Master!$B$19=0,"",OFFSET('Data Run Solvent'!A1033,0,$A$7,1,1))
			='Data Run Solvent'!A1034	=IF(Master!$B$19=0,"",OFFSET('Data Run Solvent'!A1034,0,$A$7,1,1))
a	=Master!X21	1	='Data Run Solvent'!A1035	=IF(Master!$B$19=0,"",OFFSET('Data Run Solvent'!A1035,0,$A$7,1,1))
=VLOOKUP(J4,B14:C20,2,0)	=Master!Y21	2	='Data Run Solvent'!A1036	=IF(Master!$B$19=0,"",OFFSET('Data Run Solvent'!A1036,0,$A$7,1,1))
	=Master!Z21	3	='Data Run Solvent'!A1037	=IF(Master!$B$19=0,"",OFFSET('Data Run Solvent'!A1037,0,$A$7,1,1))
	=Master!AA21	4	='Data Run Solvent'!A1038	=IF(Master!$B$19=0,"",OFFSET('Data Run Solvent'!A1038,0,$A$7,1,1))
	=Master!AB21	5	='Data Run Solvent'!A1039	=IF(Master!$B$19=0,"",OFFSET('Data Run Solvent'!A1039,0,$A$7,1,1))
	=Master!AC21	6	='Data Run Solvent'!A1040	=IF(Master!$B$19=0,"",OFFSET('Data Run Solvent'!A1040,0,$A$7,1,1))
	=Master!AD21	7	='Data Run Solvent'!A1041	=IF(Master!$B$19=0,"",OFFSET('Data Run Solvent'!A1041,0,$A$7,1,1))
			='Data Run Solvent'!A1042	=IF(Master!$B$19=0,"",OFFSET('Data Run Solvent'!A1042,0,$A$7,1,1))
b	=Master!X22	1	='Data Run Solvent'!A1043	=IF(Master!$B$19=0,"",OFFSET('Data Run Solvent'!A1043,0,$A$7,1,1))
=VLOOKUP(J4,B22:C28,2,0)	=Master!Y22	2	='Data Run Solvent'!A1044	=IF(Master!$B$19=0,"",OFFSET('Data Run Solvent'!A1044,0,$A$7,1,1))
	=Master!Z22	3	='Data Run Solvent'!A1045	=IF(Master!$B$19=0,"",OFFSET('Data Run Solvent'!A1045,0,$A$7,1,1))
	=Master!AA22	4	='Data Run Solvent'!A1046	=IF(Master!$B$19=0,"",OFFSET('Data Run Solvent'!A1046,0,$A$7,1,1))
	=Master!AB22	5	='Data Run Solvent'!A1047	=IF(Master!$B$19=0,"",OFFSET('Data Run Solvent'!A1047,0,$A$7,1,1))
	=Master!AC22	6	='Data Run Solvent'!A1048	=IF(Master!$B$19=0,"",OFFSET('Data Run Solvent'!A1048,0,$A$7,1,1))
	=Master!AD22	7	='Data Run Solvent'!A1049	=IF(Master!$B$19=0,"",OFFSET('Data Run Solvent'!A1049,0,$A$7,1,1))
			='Data Run Solvent'!A1050	=IF(Master!$B$19=0,"",OFFSET('Data Run Solvent'!A1050,0,$A$7,1,1))
c	=Master!X23	1	='Data Run Solvent'!A1051	=IF(Master!$B$19=0,"",OFFSET('Data Run Solvent'!A1051,0,$A$7,1,1))
=VLOOKUP(J4,B30:C36,2,0)	=Master!Y23	2	='Data Run Solvent'!A1052	=IF(Master!$B$19=0,"",OFFSET('Data Run Solvent'!A1052,0,$A$7,1,1))
	=Master!Z23	3	='Data Run Solvent'!A1053	=IF(Master!$B$19=0,"",OFFSET('Data Run Solvent'!A1053,0,$A$7,1,1))
	=Master!AA23	4	='Data Run Solvent'!A1054	=IF(Master!$B$19=0,"",OFFSET('Data Run Solvent'!A1054,0,$A$7,1,1))
	=Master!AB23	5	='Data Run Solvent'!A1055	=IF(Master!$B$19=0,"",OFFSET('Data Run Solvent'!A1055,0,$A$7,1,1))
	=Master!AC23	6	='Data Run Solvent'!A1056	=IF(Master!$B$19=0,"",OFFSET('Data Run Solvent'!A1056,0,$A$7,1,1))
	=Master!AD23	7	='Data Run Solvent'!A1057	=IF(Master!$B$19=0,"",OFFSET('Data Run Solvent'!A1057,0,$A$7,1,1))
			='Data Run Solvent'!A1058	=IF(Master!$B$19=0,"",OFFSET('Data Run Solvent'!A1058,0,$A$7,1,1))
d	=Master!X24	1	='Data Run Solvent'!A1059	=IF(Master!$B$19=0,"",OFFSET('Data Run Solvent'!A1059,0,$A$7,1,1))
=VLOOKUP(J4,B38:C44,2,0)	=Master!Y24	2	='Data Run Solvent'!A1060	=IF(Master!$B$19=0,"",OFFSET('Data Run Solvent'!A1060,0,$A$7,1,1))
	=Master!Z24	3	='Data Run Solvent'!A1061	=IF(Master!$B$19=0,"",OFFSET('Data Run Solvent'!A1061,0,$A$7,1,1))
	=Master!AA24	4	='Data Run Solvent'!A1062	=IF(Master!$B$19=0,"",OFFSET('Data Run Solvent'!A1062,0,$A$7,1,1))
	=Master!AB24	5	='Data Run Solvent'!A1063	=IF(Master!$B$19=0,"",OFFSET('Data Run Solvent'!A1063,0,$A$7,1,1))
	=Master!AC24	6	='Data Run Solvent'!A1064	=IF(Master!$B$19=0,"",OFFSET('Data Run Solvent'!A1064,0,$A$7,1,1))
	=Master!AD24	7	='Data Run Solvent'!A1065	=IF(Master!$B$19=0,"",OFFSET('Data Run Solvent'!A1065,0,$A$7,1,1))
			='Data Run Solvent'!A1066	=IF(Master!$B$19=0,"",OFFSET('Data Run Solvent'!A1066,0,$A$7,1,1))
e	=Master!X25	1	='Data Run Solvent'!A1067	=IF(Master!$B$19=0,"",OFFSET('Data Run Solvent'!A1067,0,$A$7,1,1))
=VLOOKUP(J4,B46:C52,2,0)	=Master!Y25	2	='Data Run Solvent'!A1068	=IF(Master!$B$19=0,"",OFFSET('Data Run Solvent'!A1068,0,$A$7,1,1))

Continued

Figure A-10 Calculations for Figure A-9

These columns are calculated in like manner to the columns to the left

```
=IF(Master!B20=0,"","0"&TEXT(Master!C3,0)&"a")
=IF(Master!$B$20=0,"",OFFSET('Data Run A'!A1027,0,$A$15,1,1))
=IF(Master!$B$20=0,"",OFFSET('Data Run A'!A1028,0,$A$15,1,1))
=IF(Master!$B$20=0,"",OFFSET('Data Run A'!A1029,0,$A$15,1,1))
=IF(Master!$B$20=0,"",OFFSET('Data Run A'!A1030,0,$A$15,1,1))
=IF(Master!$B$20=0,"",OFFSET('Data Run A'!A1031,0,$A$15,1,1))
=IF(Master!$B$20=0,"",OFFSET('Data Run A'!A1032,0,$A$15,1,1))
=IF(Master!$B$20=0,"",OFFSET('Data Run A'!A1033,0,$A$15,1,1))
=IF(Master!$B$20=0,"",OFFSET('Data Run A'!A1034,0,$A$15,1,1))
=IF(Master!$B$20=0,"",OFFSET('Data Run A'!A1035,0,$A$15,1,1))
=IF(Master!$B$20=0,"",OFFSET('Data Run A'!A1036,0,$A$15,1,1))
=IF(Master!$B$20=0,"",OFFSET('Data Run A'!A1037,0,$A$15,1,1))
=IF(Master!$B$20=0,"",OFFSET('Data Run A'!A1038,0,$A$15,1,1))
=IF(Master!$B$20=0,"",OFFSET('Data Run A'!A1039,0,$A$15,1,1))
=IF(Master!$B$20=0,"",OFFSET('Data Run A'!A1040,0,$A$15,1,1))
=IF(Master!$B$20=0,"",OFFSET('Data Run A'!A1041,0,$A$15,1,1))
=IF(Master!$B$20=0,"",OFFSET('Data Run A'!A1042,0,$A$15,1,1))
=IF(Master!$B$20=0,"",OFFSET('Data Run A'!A1043,0,$A$15,1,1))
=IF(Master!$B$20=0,"",OFFSET('Data Run A'!A1044,0,$A$15,1,1))
=IF(Master!$B$20=0,"",OFFSET('Data Run A'!A1045,0,$A$15,1,1))
=IF(Master!$B$20=0,"",OFFSET('Data Run A'!A1046,0,$A$15,1,1))
=IF(Master!$B$20=0,"",OFFSET('Data Run A'!A1047,0,$A$15,1,1))
=IF(Master!$B$20=0,"",OFFSET('Data Run A'!A1048,0,$A$15,1,1))
=IF(Master!$B$20=0,"",OFFSET('Data Run A'!A1049,0,$A$15,1,1))
=IF(Master!$B$20=0,"",OFFSET('Data Run A'!A1050,0,$A$15,1,1))
=IF(Master!$B$20=0,"",OFFSET('Data Run A'!A1051,0,$A$15,1,1))
=IF(Master!$B$20=0,"",OFFSET('Data Run A'!A1052,0,$A$15,1,1))
=IF(Master!$B$20=0,"",OFFSET('Data Run A'!A1053,0,$A$15,1,1))
=IF(Master!$B$20=0,"",OFFSET('Data Run A'!A1054,0,$A$15,1,1))
=IF(Master!$B$20=0,"",OFFSET('Data Run A'!A1055,0,$A$15,1,1))
=IF(Master!$B$20=0,"",OFFSET('Data Run A'!A1056,0,$A$15,1,1))
=IF(Master!$B$20=0,"",OFFSET('Data Run A'!A1057,0,$A$15,1,1))
=IF(Master!$B$20=0,"",OFFSET('Data Run A'!A1058,0,$A$15,1,1))
=IF(Master!$B$20=0,"",OFFSET('Data Run A'!A1059,0,$A$15,1,1))
=IF(Master!$B$20=0,"",OFFSET('Data Run A'!A1060,0,$A$15,1,1))
=IF(Master!$B$20=0,"",OFFSET('Data Run A'!A1061,0,$A$15,1,1))
=IF(Master!$B$20=0,"",OFFSET('Data Run A'!A1062,0,$A$15,1,1))
=IF(Master!$B$20=0,"",OFFSET('Data Run A'!A1063,0,$A$15,1,1))
=IF(Master!$B$20=0,"",OFFSET('Data Run A'!A1064,0,$A$15,1,1))
=IF(Master!$B$20=0,"",OFFSET('Data Run A'!A1065,0,$A$15,1,1))
=IF(Master!$B$20=0,"",OFFSET('Data Run A'!A1066,0,$A$15,1,1))
=IF(Master!$B$20=0,"",OFFSET('Data Run A'!A1067,0,$A$15,1,1))
=IF(Master!$B$20=0,"",OFFSET('Data Run A'!A1068,0,$A$15,1,1))
=IF(Master!$B$20=0,"",OFFSET('Data Run A'!A1069,0,$A$15,1,1))
=IF(Master!$B$20=0,"",OFFSET('Data Run A'!A1070,0,$A$15,1,1))
=IF(Master!$B$20=0,"",OFFSET('Data Run A'!A1071,0,$A$15,1,1))
=IF(Master!$B$20=0,"",OFFSET('Data Run A'!A1072,0,$A$15,1,1))
```

```
=IF(Master!$B:=IF(Master!$B:=IF(Master!$B:=IF(Master!$B:=IF(Master!$B:
```

	047-029		047-030		047-031		047-032		047-033		047-034
Simple Max Value	3568		2670		2543		2979		3232		2430
Simple Max Channel	348		349		349		348		349		349
Range Rows	321		322		322		321		322		322
	381		382		382		381		382		382
Dbase lookup header:	Value		Value		Value		Value		Value		Value
Max Value	2232.564		1387.371		1217.214		1652.846		1962.025		1083.054
Complex Max	348		349		349		349		349		349
	Channel	Value	Channel	Value	Channel	Value	Channel	Value	Channel	Value	Channel
0	321	1246	322	824	322	717	321	938	322	1158	322
1	322	1317	323	863	323	762	322	984	323	1210	323
2	323	1370	324	886	324	784	323	1020	324	1261	324
3	324	1430	325	931	325	818	324	1062	325	1315	325
4	325	1477	326	945	326	839	325	1090	326	1365	326
5	326	1526	327	977	327	868	326	1138	327	1410	327
6	327	1566	328	995	328	893	327	1179	328	1440	328
7	328	1612	329	1026	329	910	328	1211	329	1481	329
8	329	1652	330	1056	330	926	329	1241	330	1513	330
9	330	1707	331	1076	331	944	330	1277	331	1543	331
10	331	1739	332	1095	332	970	331	1304	332	1577	332
11	332	1778	333	1132	333	984	332	1330	333	1612	333
12	333	1812	334	1147	334	1001	333	1361	334	1636	334
13	334	1848	335	1167	335	1016	334	1388	335	1673	335
14	335	1880	336	1191	336	1045	335	1405	336	1701	336
15	336	1913	337	1223	337	1062	336	1431	337	1731	337
16	337	1947	338	1236	338	1079	337	1461	338	1758	338
17	338	1982	339	1258	339	1100	338	1482	339	1786	339
18	339	2014	340	1270	340	1117	339	1500	340	1814	340
19	340	2046	341	1301	341	1135	340	1523	341	1837	341
20	341	2078	342	1313	342	1148	341	1550	342	1864	342
21	342	2111	343	1337	343	1171	342	1574	343	1885	343
22	343	2137	344	1344	344	1182	343	1592	344	1906	344
23	344	2162	345	1365	345	1198	344	1610	345	1920	345
24	345	2191	346	1364	346	1196	345	1616	346	1933	346
25	346	2212	347	1384	347	1213	346	1642	347	1942	347
26	347	2221	348	1371	348	1210	347	1649	348	1953	348

Figure A-11 This page shows the results from the peak max search algorithm. The =MAX command is used to find the first occurrence of the maximum. The area around this point is then searched for points of equal height, and the channel number of all equivalent maxima are averaged. The next page shows a representative set of expressions for one peak search.

		='Raw Data'!B2
Simple Max Value		=MAX(OFFSET('Raw Data'!B3,Master!$D$9,0,(Master!$E$9-Master!$D$9),1))
Simple Max Channel		=VLOOKUP(C3,OFFSET('Raw Data'!B3,Master!$D$9,0,(Master!$E$9-Master!$D$9),2),2,0)
Range Rows		=C4-30+3
		=C4+30+3
Dbase lookup header:		Value
Max Value		=MAX(D11:D71)
Complex Max		=DAVERAGE(C10:D71,"Channel",C7:C8)
		Channel
	0	=OFFSET('Raw Data'!$B$3,C$5+$B11,1,1,1)
	1	=OFFSET('Raw Data'!$B$3,C$5+$B12,1,1,1)
	2	=OFFSET('Raw Data'!$B$3,C$5+$B13,1,1,1)
	3	=OFFSET('Raw Data'!$B$3,C$5+$B14,1,1,1)
	4	=OFFSET('Raw Data'!$B$3,C$5+$B15,1,1,1)
	5	=OFFSET('Raw Data'!$B$3,C$5+$B16,1,1,1)
	6	=OFFSET('Raw Data'!$B$3,C$5+$B17,1,1,1)
	7	=OFFSET('Raw Data'!$B$3,C$5+$B18,1,1,1)
	8	=OFFSET('Raw Data'!$B$3,C$5+$B19,1,1,1)
	9	=OFFSET('Raw Data'!$B$3,C$5+$B20,1,1,1)
	10	=OFFSET('Raw Data'!$B$3,C$5+$B21,1,1,1)
	11	=OFFSET('Raw Data'!$B$3,C$5+$B22,1,1,1)
	12	=OFFSET('Raw Data'!$B$3,C$5+$B23,1,1,1)
	13	=OFFSET('Raw Data'!$B$3,C$5+$B24,1,1,1)
	14	=OFFSET('Raw Data'!$B$3,C$5+$B25,1,1,1)
	15	=OFFSET('Raw Data'!$B$3,C$5+$B26,1,1,1)
	16	=OFFSET('Raw Data'!$B$3,C$5+$B27,1,1,1)
	17	=OFFSET('Raw Data'!$B$3,C$5+$B28,1,1,1)
	18	=OFFSET('Raw Data'!$B$3,C$5+$B29,1,1,1)
	19	=OFFSET('Raw Data'!$B$3,C$5+$B30,1,1,1)
	20	=OFFSET('Raw Data'!$B$3,C$5+$B31,1,1,1)
	21	=OFFSET('Raw Data'!$B$3,C$5+$B32,1,1,1)
	22	=OFFSET('Raw Data'!$B$3,C$5+$B33,1,1,1)
	23	=OFFSET('Raw Data'!$B$3,C$5+$B34,1,1,1)
	24	=OFFSET('Raw Data'!$B$3,C$5+$B35,1,1,1)
	25	=OFFSET('Raw Data'!$B$3,C$5+$B36,1,1,1)
	26	=OFFSET('Raw Data'!$B$3,C$5+$B37,1,1,1)

Figure A-12 Calculations for Figure A-11

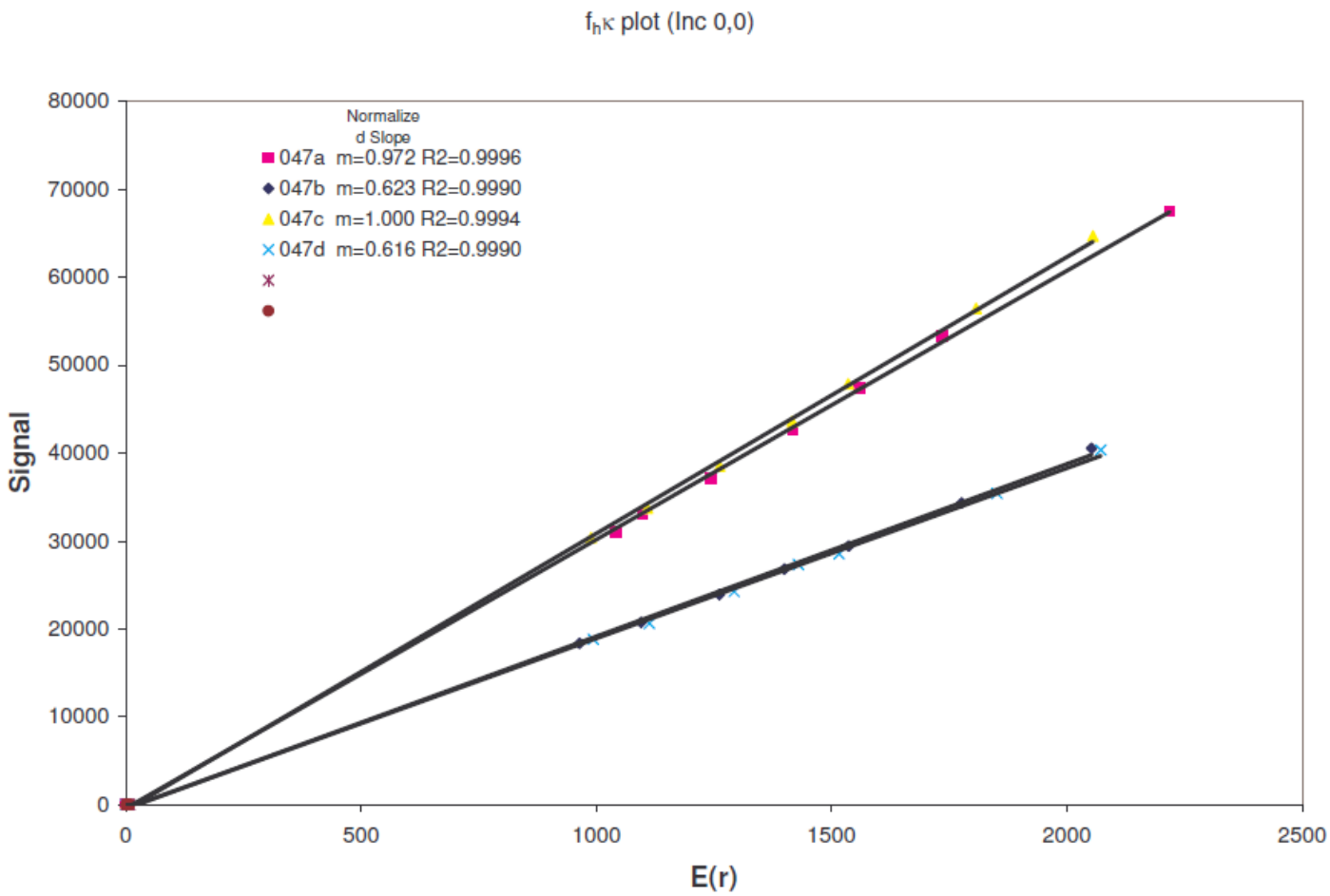

Figure A-13 Up to 6 $f_h^{obs}\kappa$ may be determined in this spreadsheet simultaneously. Normalized slopes are computed and displayed to give an immediate sense of reproducibility. The actual slopes and their errors are pooled separately, allowing f_h^{obs} of the sample to be determined. This plot is typically printed by the user and included in the hardcopy report.

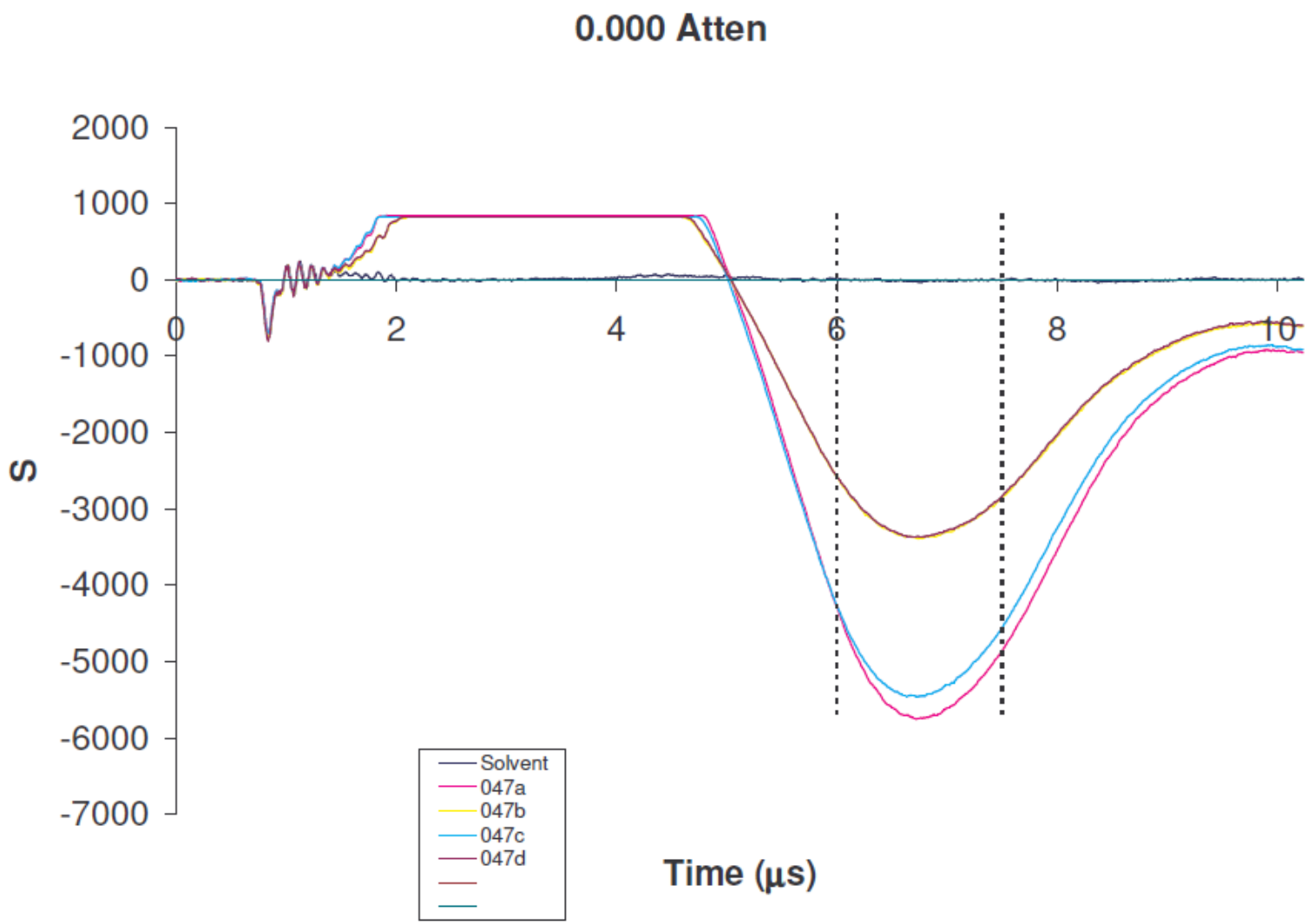

Figure A-14 This plot shows multiple waves acquired at similar attenuation, as discussed above. This plot is typically printed by the user and included in the hardcopy report.

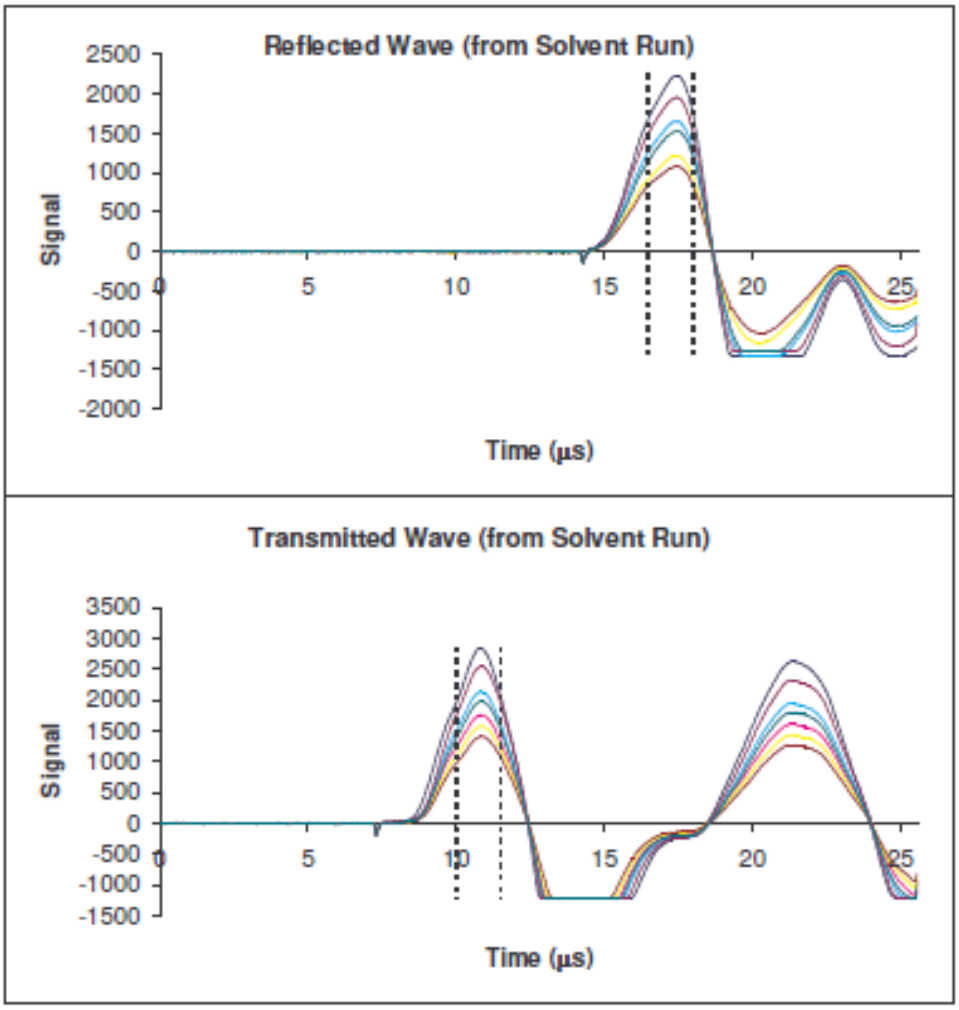

Figure A-15 This portion of the spreadsheet shows a number of reflected and transmitted waves, and is used to verify that these reference waves are of proper quality. This plot is typically printed by the user and included in the hardcopy report.

APPENDIX B

DETAILED PROCEEDURE FOR MEASURING THE VOLUME CHANGE OF A REACTION VIA MOLECULAR DYNAMICS

This section contains a detailed protocol for measuring the solvated volume of a molecule. The References referred to in this procedure are: [125, 126].

KEY: Directions Windows/DOS file format UNIX/Linux file format `commands`

Important info

PHASE 1 – Preparing the structure for structure minimization and electrostatic fitting

1. In the Windows operating system, open GaussView and build your molecule. Save this file in the Gaussian Z-matrix form for ease of editing/interpretation.

Many other file types can be used here (very useful if you're using published structures). See the Amber manual under "Antechamber" for more info.

Structure.gjf

Text Format

2. Copy Structure.gjf to a Linux computer with Amber installed. In the same directory as you have placed Structure.gjf, open a terminal window and enter:

`dos2unix Structure.gjf` *(note the capitalization – it matters in Linux!)*

This file is now in 'UNIX' format. This format is still text, and can be read in Windows with programs like WordPad, but it uses a different computer code to mark the end of a line of text. Many problems in this procedure can be attributed to a failure to convert to Linux format!

Structure.gjf

Text Format

3. Open Structure.gjf in a text editor (e.g. gedit). Make sure the file reads:

```
%chk=InitialStructure
%mem=6MW
%nproc=1
# opt=tight hf/6-31G* geom=connectivity
Initial Structure
```

…and leave everything from the line reading "0 1" down alone (the coordinates). Save the file and close the editor.

Structure.gjf

Text Format

PHASE 1 (con't)

4. Open a new text editing window. In it, type:

```
%chk=InitialStructure
%mem=6MW
%nproc=1
# hf/6-31G* geom=checkpoint SCF=tight Test Pop=MK
iop(6/33=2) iop(6/42=6) guess=read
RESP

0 1
```

…and add a blank line after "0 1" (*Gaussian always expects an extra line at the end.*) Save this file as StructureForRESP.gjf

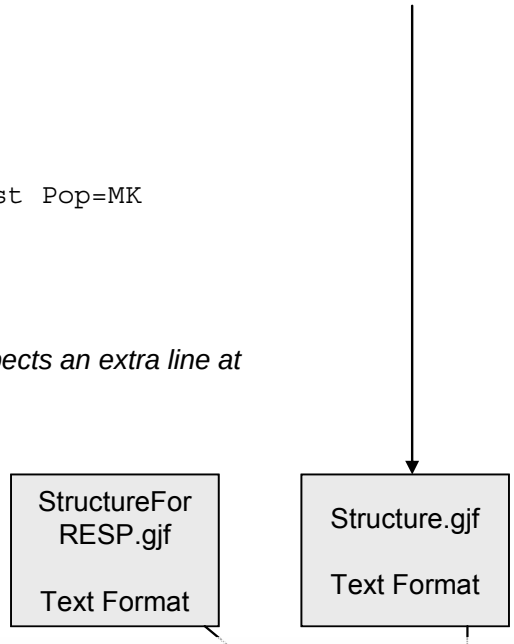

PHASE 2 – Performing structure minimization and electrostatic fitting

4. Open FileZilla, and connect to the cluster:

Host: markov.cmms.pitt.edu
ServerType: SFTP – SSH File Transfer Protocol

Create a directory with the name of your experiment (in this example, "Experiment") and upload both Structure.gjf and StructureForRESP.gjf into it.

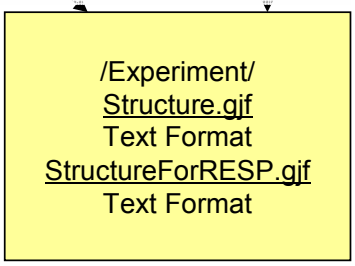

To save space, we will now list filenames/formats rather than using grey icons

5. Open a terminal window. Type:

```
ssh username@markov.cmms.pitt.edu
```

Enter your password, then type:

```
cd Experiment
```

(in Linux, if you start to type a directory or filename, you can hit Tab to autocomplete the word.)

Now, type the following commands:

```
G03pbs Structure.gjf small_io OptimizeStructure

G03pbs StructureForRESP.gjf small_io RESP
```

This will generate two files, OptimizeStructure.pbs and RESP.pbs

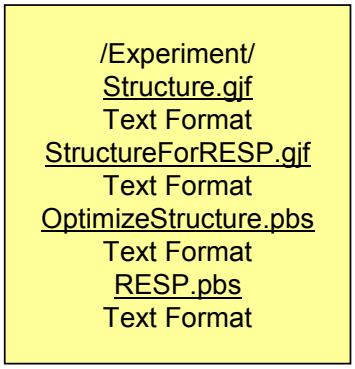

PHASE 2 (con't)

6. Type: `qsub OptimizeStructure.pbs` This will start Gaussian running. To monitor the progress of the calculation, type:

`tail -f OptimizeStructure.log` Once the run is complete, hit `ctrl-z` to return to the command line. Then start the RESP run:

```
qsub RESP.pbs
```

```
tail -f RESP.log
```

Once the RESP run is complete type:

```
/usr/prog/g03/g03/formchk RESP.chk RESP.fchk
```

/Experiment/
New files:
OptimizeStructure.log
g03 output (text format)
RESP.log
g03 output (text format)
RESP.chk
g03 checkpoint (binary format)
RESP.fchk
g03 formatted checkpoint (text format)

7. Use FileZilla to download the entire directory to your Linux computer. Open a terminal window in this directory. (You can also close any other terminal windows that are open.) Type: `vmd` and open RESP.fchk in this program. Check to be sure the structure is reasonable. Close the program.

In the same terminal window, type (as one command):

```
antechamber -fi gout -fo prepi -i RESP.log -o
RESP.prepi -c resp -at gaff -rn mol -pf y
```

Then:

```
parmchk -f prepi -i RESP.prepi -o RESP.frcmod
```

Open the RESP.frcmod file, and make sure the best-guesses for any missing parameters are reasonable. (See http://amber.scripps.edu/formats.html for more info)

These commands will generate many new files, but the two we care about are the .prepi and the .frcmod files. The prepi (prepin) file is Amber's preferred format, and contains coordinates, charges, bond orders, atom types, etc. The frcmod file will tell Amber in the next few steps what forcefield parameters should be overridden, and adds missing parameters to the run.

/Experiment/
New files of interest:
RESP.prepi
Amber Prep file (text format)
RESP.frcmod
Amber forcemod file – checks to see if all force field param.s exist, any missing are in this file with best-guesses

PHASE 3 – Solvating the molecule, and setting up the MD run

8. Type as one command: `$AMBERHOME/exe/xleap -s -f $AMBERHOME/dat/leap/cmd/leaprc.ff99`

Then type the following in the new window: (*make sure number lock of OFF and your mouse is over this window, otherwise weird behavior may occur*).

```
source leaprc.gaff
loadamberprep RESP.prepi
check mol
loadamberparams RESP.frcmod
saveoff mol RESP.lib
molwb = copy mol
```

`solvatebox molwb SPCFWBOX 12` Repeat these last two commands with different numbers in the last command until you are happy with the number of waters added. The number of waters added should be the same for each structure in the reaction.

This number can be fine-tuned by typing

```
edit molwb
```

and carefully deleting an appropriate number of water molecules. When done, close the window with the menu, NOT the close button (*this will close the entire program and you will need to redo this step.*)

If you make a mistake, type the copy, solvatebox, and edit commands again.

Now, we will write out the input coordinates and the topography file for the MD simulation (type as a single command):

```
saveamberparm molwb Structure.prmtop
Structure.inpcrd
```

/Experiment/
New files:
RESP.lib
Amber lib file
saves the current state
(text format)
Structure.prmtop
topography file (text format)
Structure.inpcrd
starting coord.s (text format)

PHASE 3 – con't

9. We must also make a water box without a solute. This step must be completed only once for an studied reaction. In the same window as in Step 8, type:

```
wb = copy molwb
edit molwb
```

A graphic editor will open. Carefully delete each atom of the solute, without deleting any waters. When done, close the window with the menu, NOT the close button.

type: `saveamberparm wb wbox.prmtop wbox.inpcrd`

This window may now be closed.

/Experiment/
New files of interest:
wbox.prmtop
wbox.inpcrd

Move these files to a separate directory (/wbox/) and follow stepsfrom her on in parallel

10. We will now prepare the input files for Amber. These files are all text, and contain a number of flags within them. The examples given here are an excellent starting point, but be sure to consult with the Amber9 Users' Manual to understand what each does. Copy/paste the code below into a text editor, and save the file with the name listed at the top. INCLUDE ALL BLANK LINES AND OMIT COMMENTS IN CAPS!!!

Structure-min1.in .

```
Minimization of solvent
 &cntrl
  imin   = 1,
  maxcyc = 1000,
  ncyc   = 500,
  ntb    = 1,
  ntr    = 1,
  cut    = 9
 /
Solute fixed
500.0
ATOM 1 2          ←CHANGE THE LAST NUMBER TO THE
END                 NUMBER OF ATOMS IN YOUR
END                 MOLECULE!!!!!   REMOVE ANYTHING
                     AFTER " / " FOR WATERBOX FILES
                    AND MAKE ntr = 0
```

/Experiment/
New files:
Structure-min1.in
Holds solute still while minimizing the solvent

PHASE 3 – con't

10. (con't).

/Experiment/
New files:
Structure-min2.in
minimizes the solvent and solute positions
Structure-md1.in
heats solvent from 0 – 300K under constant volume/pressure

Structure-min2.in .

```
Minimization of solvent
 &cntrl
  imin   = 1,
  maxcyc = 2500,
  ncyc   = 1000,
  ntb    = 1,
  ntr    = 0,
  cut    = 9
/
```

Structure-md1.in (20 ps) .

```
MD nPV
 &cntrl
  imin   = 0,
  ntx    = 1,
  irest  = 0,
  ntpr = 50,
  ntwx = 100,
  ntwr = 1000,
  nstlim = 10000,
  dt = 0.002,
  ntt    = 3,
  gamma_ln = 1.0,
  temp0  = 300.0,
  tempi  = 0.0,
  ntc    = 2,
  ntf    = 2,
  ntb    = 1,
  cut    = 9,
  ntr    = 1
 /
Solute fixed - weak restraint
10.0
ATOM 1 2          ←CHANGE THE LAST NUMBER TO THE
END                 NUMBER OF ATOMS IN YOUR
END                 MOLECULE!!!!!   REMOVE ANYTHING
                    AFTER " / " FOR WATERBOX FILES AND
                    MAKE ntr = 0
```

PHASE 3 – con't

10. (con't).

Structure-md2.in (200 ps) .

```
MD nPT
 &cntrl
  imin   = 0,
  ntx    = 7,
  irest  = 1,
  ntpr = 50,
  ntwx = 100,
  ntwr = 1000,
  nstlim = 50000,
  dt = 0.002,
  ntt    = 3,
  gamma_ln = 1.0,
  temp0  = 300.0,
  tempi  = 300.0,
  ntc    = 2,
  ntf    = 2,
  ntb    = 2,
  pres0  = 1.0,
  ntp    = 1,
  taup   = 2.0,
  cut    = 9,
  ntr    = 0
/
```

/Experiment/
New files:
Structure-md2.in
Holds temperature and pressure constant, at beginning compresses system reasonable density, then we begin collecting real volume data

PHASE 3 – con't

11. Now we will prepare the file that submits our job to the cluster's queue system. Create the following file in a text editor:

Structure.pbs .

```
#!/bin/bash

########### JOB NAME ##########################
#PBS -N Structure
########### DECLARE JOB NON-RERUNABLE #########
#PBS -r n
########### PBS OUTPUT FILENAMES ##############
#PBS -e Structure.error
#PBS -o Structure.stdout
########### QUEUE NAME ########################
#PBS -q small_io
########### NUMBER OF NODES, etc ##############
#PBS -l nodes=2:ppn=2
#PBS -l mem=450MB
#PBS -l walltime=120:00:00
#PBS -l cput=120:00:00
#PBS -V
cd /home/other/USER/Experiment/

AMBERHOME=/usr/prog/amber/9.04apr06
#unset LD_LIBRARY_PATH
export
LD_LIBRARY_PATH=/usr/prog/intel/cce/9.1.038/lib:/usr/prog/int
el/fc/9.0/lib

LAMHOME=/usr/prog/LAM_mpi/7.0.6/icc_9.1.038/bin
export PATH=$LAMHOME:$PATH

if [ -e lamhosts ]; then
 rm lamhosts
fi
for m in $( cat "$PBS_NODEFILE" )
do
  echo $m >> lamhosts
done
$LAMHOME/lamboot -v lamhosts
```

/Experiment/
New files:
Structure.pbs
contains all the commands that will be run by the queue. This is set up to use 4 processors

THIS LINE MUST BE EDITED TO TELL THE QUEUE WHAT DIRECTORY ON THE CLUSTER WILL CONTAIN THIS JOB!

THIS FILE CONTINUES ON THE NEXT PAGE – THE LINES IN GREEN ARE REPEATED SO YOU CAN SEE HOW THEY FIT – ONLY INCLUDE THEM ONCE IN THE FILE YOU CREATE

PHASE 3 – con't

11. (Con't)

```
echo $m >> lamhosts
done
$LAMHOME/lamboot -v lamhosts

$LAMHOME/mpirun -v -np 4 $AMBERHOME/exe/sander.MPI \
  -i Structure-min1.in \
  -o Structure-min1.out \
  -p Structure.prmtop \
  -c Structure.inpcrd \
  -r Structure-min1.rst \
  -ref Structure.inpcrd \

$LAMHOME/mpirun -v -np 4 $AMBERHOME/exe/sander.MPI \
  -i Structure-min2.in \
  -o Structure-min2.out \
  -p Structure.prmtop \
  -c Structure-min1.rst \
  -r Structure-min2.rst \

$LAMHOME/mpirun -v -np 4 $AMBERHOME/exe/sander.MPI \
  -i Structure-md1.in \
  -o Structure-md1.out \
  -p Structure.prmtop \
  -c Structure-min2.rst \
  -r Structure-md1.rst \
  -x Structure-md1.mdcrd \
  -ref Structure-min2.rst \

$LAMHOME/mpirun -v -np 4 $AMBERHOME/exe/sander.MPI \
  -i Structure-md2.in \
  -o Structure-md2.out \
  -p Structure.prmtop \
  -c Structure-md1.rst \
  -r Structure-md2.rst \
  -x Structure-md2.mdcrd \

$LAMHOME/lamhalt
$LAMHOME/lamclean

exit 0
```

PHASE 3 – con't

11. (Con't)

```
echo $m >> lamhosts
done
$LAMHOME/lamboot -v lamhosts

$LAMHOME/mpirun -v -np 4 $AMBERHOME/exe/sander.MPI \
  -i Structure-min1.in \
  -o Structure-min1.out \
  -p Structure.prmtop \
  -c Structure.inpcrd \
  -r Structure-min1.rst \
  -ref Structure.inpcrd \

$LAMHOME/mpirun -v -np 4 $AMBERHOME/exe/sander.MPI \
  -i Structure-min2.in \
  -o Structure-min2.out \
  -p Structure.prmtop \
  -c Structure-min1.rst \
  -r Structure-min2.rst \

$LAMHOME/mpirun -v -np 4 $AMBERHOME/exe/sander.MPI \
  -i Structure-md1.in \
  -o Structure-md1.out \
  -p Structure.prmtop \
  -c Structure-min2.rst \
  -r Structure-md1.rst \
  -x Structure-md1.mdcrd \
  -ref Structure-min2.rst \

$LAMHOME/mpirun -v -np 4 $AMBERHOME/exe/sander.MPI \
  -i Structure-md2.in \
  -o Structure-md2.out \
  -p Structure.prmtop \
  -c Structure-md1.rst \
  -r Structure-md2.rst \
  -x Structure-md2.mdcrd \

$LAMHOME/lamhalt
$LAMHOME/lamclean

exit 0
```

PHASE 3 – con't

12. Upload the following files to the directory on the cluster where you want to run the experiment:

Structure.inpcrd

Structure.prmtop

Structure.pbs

Structure-min1.in

Structure-min2.in

Structure-md1.in

Structure-md2.in

/cluster/……./Experiment/
Files uploaded:
Structure.inpcrd
Structure.prmtop
Structure.pbs
Structure-min1.in
Structure-min2.in
Structure-md1.in
Structure-md2.in

13. Connect to the cluster as in Step 5. Type the following:

```
cd Experiment
qsub Structure.pbs
pbstop
u
me
```

This will start the job running on the cluster. The command pbstop brings up a graphic display of what's running on the cluster, and the commands "u" and "me" tells the program to show your jobs. Leave this window open so you can see when your job is done. You may then close the window.

PHASE 3 – con't

14. Amber will generate a lot of new files. This page tells what these files contain and how they are used. For this page only, use the following key: *input for that step* **output for that step**

min1.in – run settings
min.inpcrd – starting coords
min.prmtop – molecule properties
min1.out – results of MD
min1.rst – final vector info for all atoms

min2.in – run settings
min1.rst – starting coords
min.prmtop – molecule properties
min2.out – results of MD
min2.rst – final vector info for all atoms

md1.in – run settings
min2.rst – starting coords
min.prmtop – molecule properties
md1.out – results of MD
md1.rst – final vector info for all atoms
md1.mdcrd – file containing info for every saved step in the simulation

md2.in – run settings
md1.rst – starting coords
min.prmtop – molecule properties
md2.out – results of MD
md2.rst – final vector info for all atoms
md2.mdcrd – file containing info for every saved step in the simulation

/cluster/……./Experiment/
Files created:
Structure-min1.out
Structure-min1.rst
Structure-min2.out
Structure-min2.rst
Structure-md1.out
Structure-md1.mdcrd
Structure-md1.rst
Structure-md2.out
Structure-md2.mdcrd
Structure-md2.rst

PHASE 4 – Interpreting the Data

15. Use FileZilla to download all files in the "Experiment" directory on the cluster to your Linux computer in the directory "Experiment".

Open a terminal window in this directory, and type the following commands:

```
ambpdb -p Structure.prmtop <  Structure.inpcrd
> Structure-startmin.pdb
```

```
ambpdb -p Structure.prmtop <  Structure-
min2.rst  > Structure-startmin.pdb
```

```
vmd -m Structure-startmin.pdb -m Structure-
endmin.pdb
```
In this window, verify that the structures before and after minimization are reasonable

```
mkdir analysis
```

```
cd analysis
```

```
process_mdout.perl ../Structure-md1.out
../Structure-md2.out
```

```
gedit summary.VOLUME
```

```
gedit summary.DENSITY
```

Delete all data before 20 ps in both files that open (during the nVT portion of the simulation, neither volume nor density info is written out.) save both files and close the editor.

16. type:

```
xmgr summary.EPTOT summary.EKTOT summary.ETOT
```

```
xmgr summary.TEMP
```

```
xmgr summary.PRES
```

```
xmgr summary.VOLUME
```

```
xmgr summary.DENSITY
```

Examine each graph that pops up to ensure that after ~60-80 ps the property has stabilized.

/Experiment/
Files created:
Structure-startmin.pdb
structure of your molecule before Amber minimization
Structure-endmin.pdb
structure of your molecule after Amber minimization
an entire directory of summary files in "analysis"
individual text files of various over time

PHASE 4 – (Con't)

17. In the directory "Experiment", create a new text file:

Structure-reimaged.ptraj .

```
trajin Structure-md1.mdcrd
trajin Structure-md2.mdcrd
trajout Structure-reimaged.mdcrd
center @1-2    ← FIX THIS
image center triclinic
```

In the terminal window from steps 15 and 16, type:

```
cd ..
```

```
ptraj Structure.prmtop < Structure-reimaged.ptraj
```

```
vmd -f -parm7 Structure.prmtop -crdbox Structure-reimaged.mdcrd
```

Verify the structures look ok throughout simulation. In VMD, if you choose /Graphics/Representations, and type "all not water" into the box labeled "Selected atoms", you can omit the water from the display.

/Experiment/
Files created:
Structure-reimaged.ptraj
used to combine md1 and md2 into single file, 'wraps' around waters that diffused into neighboring boxes
Structure-reimaged.mdcrd
combined file of md1 and md2, 'wraps' around waters that diffused into neighboring boxes

PHASE 5 – Determining the Correlation Time

18. The averages of the modeled properties are fine, but we cannot yet determine the standard deviation (the points must be statistically independent, but we sampled too frequently at this stage, meaning the points are not statistically independent.)

Copy the file /Experiment/analysis/summary.volume to a Windows desktop.

Open the Excel spreadsheet "Correlation Times.xls", and open summary.volume in Excel as a separate file (when the import wizard prompts you, choose: Delimited; Tab, Space, Treat Consecutive Delimiters as One; finish). Copy/paste these two data columns into the Correlation Time spreadsheet under "All Pts".

This sheet expects that the first 80 ps were used to equilibrate the system. Select all points from 80 ps onward, and paste these in the column marked Equilibrated Data.

Look at the two plots in this file. The first plots a term s vs. τ_b (the time between samples). Identify the τ_b for which this plot plateaus. For the second plot (s vs. 1/ τ_b), identify the y-intercept most centered in the trend. The average of the values from both plots identifies the amount of time needed between samples (e.g. τ_b = 38, time between sample should be 3.8 ps.)

Save a copy of this spreadsheet to include with the data archive.

Note that this description of the correlation time is highly contextualized for this procedure AS WRITTEN! Read and understand Section 6.4.1 in Allen and Tildesley's book "Computer Simulations of Liquids", or Friedberg and Cameron's paper in vol. 52 #12, J. Chem. Phys., 1970, p. 6049 for background.

in Windows
Files created:
Correlation Time.xls
Determines how far apart samples must be to be statistically independent

PHASE 6 – Setting up Production MD Run

18. A new MD simulation must now be prepared with a longer run time, and wider spacing between samples. This process will be nearly identical to steps 10 – 17.

In Windows, open the Excel spreadsheet named "Amber Input File Time Step Calculator.xls" this will help choose Amber settings for the new MD simulation.

dt: amount of time between MD steps – this should be kept between 0.001 and 0.002 ps

nstlim: number of MD steps to be performed. dt * nstlim = total run time of that portion of the calculation. Can be any number, but I recommend shooting for a runtime of ~ 2 ns

ntpr: steps between updates to the md#.out file. Choose a number of steps that gives a time step close to the correlation time you previously determined

ntwx: steps between updates to the md#.mdcrd file. Select as for ntpr

ntwr: steps between updates to the md#.rst file. Select as for ntpr

Write down the values you selected, as well as the "Cycles necessary" (i.e. how many calculation portions you will need to build in order to get the targeted simulation length.)

19. On the Linux computer, copy all files from "Experiment" into a new directory called "ProductionRun". Structure-min1, -min2, and -md1 do not need to be rerun. Delete any files not listed to the right.

/ProductionRun/
Files kept:
Structure.prmtop
Structure.inpcrd
Structure.pbs
Structure-reimaged.ptraj
Structure-min1.in
Structure-min1.out
Structure-min1.rst
Structure-min2.in
Structure-min2.out
Structure-min2.rst
Structure-md1.in
Structure-md1.out
Structure-md1.mdcrd
Structure-md1.rst
Structure-md2.in

PHASE 6 – (Con't)

20. Edit the file Structure-md2.in – replace dt, nstlim, ntpr, ntwx, and ntwr with the values you selected. Save this file.

Copy this file, and rename if Structure-md3.in. Repeat until the number reaches a few numbers higher than the "Cycles Necessary" you determined earlier.

/ProductionRun/
New Files:
Structure-md2.in
Structure-md3.in
Structure-md4.in
…
Structure-md##.in

21. Edit the file Structure.pbs – delete the blocks for min1, min2, and md1.

Copy and paste the block for md2, and increase each number by 1. Repeat this until you have a section for every md##.in file you created.

At the top of the file, change the directory this job will run in to:
cd /home/other/USER/ProductionRun/

The purpose of this (time-consuming) setup is to ensure that if a portion of the calculation crashes, you can simply open Structure.pbs and delete all the blocks related to the jobs which already ran. (e.g. if md24 crashes, delete the blocks before md25 and restart the job on the cluster). This ensures that a crash can only slow you down, rather than forcing you to start from scratch. After all, this job may take ~ 2 weeks to run!

/ProductionRun/
Modified Files:
Structure.pbs

PHASE 8 – Interpreting the Final Data

/ProductionRun/
ALL FILES:

24. Once the entire simulation is completed, download the entire directory to a Linux computer.

Repeat steps 15 – 17, with the following modifications (to account for the bigger number of files…)

```
process_mdout.perl ../Structure-md1.out
../Structure-md2.out ../Structure-md3.out
... ../Structure-md##.out
```

Modify Structure-reimaged.ptraj to have a "trajin" line for every file you created (i.e. … `trajin Structure-md##.mdcrd`)

Windows
summary.volume into Excel

24. Copy summary.volume to a Windows computer, open the file in Excel, and determine the Average and Standard Deviation for the volume. If the error is too high, you can restart the simulation and run for longer.

APPENDIX C

GAFF PARAMETERS FOR MODELING DPCP, DPA, CIS-AZOBENZENE, AND TRANS-AZOBENZENE WITH AMBER 9

C.1 CIS-AZOBENZENE.FRCMOD

```
remark goes here
MASS
ca 12.01         0.360               Sp2 C in pure aromatic systems
ha 1.008         0.135               H bonded to aromatic carbon
ne 14.01         0.530               Inner Sp2 N in conjugated systems
nf 14.01         0.530               Inner Sp2 N in conjugated systems, identical to ne

BOND
ca-ca  478.4    1.387        SOURCE1  6228    0.0096    0.0147
ca-ha  344.3    1.087        SOURCE3  1496    0.0024    0.0045
ca-ne  361.8    1.431        SOURCE1    52    0.0000    0.0000
ca-nf  361.8    1.431        SOURCE1    52    0.0000    0.0000
ne-nf  738.6    1.257        SOURCE3     1    0.0000    0.0000

ANGLE
ca-ca-ca    67.2      119.97    SOURCE3 1969   0.1024   0.3480
ca-ca-ha    48.5      120.01    SOURCE3 2980   0.1509   0.2511
ca-ca-ne    67.7      119.88    SOURCE3   24   0.2867   0.3637
ca-ca-nf    67.7      119.88    SOURCE3   24   0.2867   0.3637
ca-ne-nf    69.9      114.72    SOURCE3    2   0.0000   0.0000
ca-nf-ne    69.9      114.72    SOURCE3    2   0.0000   0.0000

DIHE
ca-ca-ca-ha   1    3.625       180.000           2.000      intrpol.bsd.on C6H6
ca-ca-ca-ca   1    3.625       180.000           2.000      intrpol.bsd.on C6H6
ca-ca-ne-nf   1    0.000       180.000           3.000
ca-ca-nf-ne   1    0.000       180.000           3.000
ha-ca-ca-ha   1    3.625       180.000           2.000      intrpol.bsd.on C6H6
ha-ca-ca-ne   1    3.625       180.000           2.000      intrpol.bsd.on C6H6
ha-ca-ca-nf   1    3.625       180.000           2.000      intrpol.bsd.on C6H6
ca-ca-ca-ne   1    3.625       180.000           2.000      intrpol.bsd.on C6H6
ca-ca-ca-nf   1    3.625       180.000           2.000      intrpol.bsd.on C6H6
X -ne-nf-X    1    3.000       180.000          -2.000      double bond
X -ne-nf-X    1    2.800       180.000           1.000      double bond

IMPROPER
ca-ca-ca-ha         1.1          180.0         2.0          General improper torsional
ca-ca-ca-ne         1.1          180.0         2.0          Using default value
ca-ca-ca-nf         1.1          180.0         2.0          Using default value

NONBON
  ha          1.4590  0.0150             Spellmeyer
  ca          1.9080  0.0860             OPLS
```

```
  ne          1.8240  0.1700             OPLS
  nf          1.8240  0.1700             OPLS



r
```

C.2 TRANS-AZOBENZENE.FRCMOD

```
remark goes here
MASS
ca 12.01         0.360               Sp2 C in pure aromatic systems
ha 1.008         0.135               H bonded to aromatic carbon
ne 14.01         0.530               Inner Sp2 N in conjugated systems
nf 14.01         0.530               Inner Sp2 N in conjugated systems, identical to ne

BOND
ca-ca  478.4    1.387        SOURCE1  6228    0.0096    0.0147
ca-ha  344.3    1.087        SOURCE3  1496    0.0024    0.0045
ca-ne  361.8    1.431        SOURCE1    52    0.0000    0.0000
ca-nf  361.8    1.431        SOURCE1    52    0.0000    0.0000
ne-nf  738.6    1.257        SOURCE3     1    0.0000    0.0000

ANGLE
ca-ca-ca    67.2      119.97    SOURCE3 1969   0.1024   0.3480
ca-ca-ha    48.5      120.01    SOURCE3 2980   0.1509   0.2511
ca-ca-ne    67.7      119.88    SOURCE3   24   0.2867   0.3637
ca-ca-nf    67.7      119.88    SOURCE3   24   0.2867   0.3637
ca-ne-nf    69.9      114.72    SOURCE3    2   0.0000   0.0000
ca-nf-ne    69.9      114.72    SOURCE3    2   0.0000   0.0000

DIHE
ca-ca-ca-ha   1    3.625       180.000           2.000      intrpol.bsd.on C6H6
ca-ca-ca-ca   1    3.625       180.000           2.000      intrpol.bsd.on C6H6
ca-ca-ne-nf   1    0.000       180.000           3.000
ca-ca-nf-ne   1    0.000       180.000           3.000
ha-ca-ca-ha   1    3.625       180.000           2.000      intrpol.bsd.on C6H6
ha-ca-ca-ne   1    3.625       180.000           2.000      intrpol.bsd.on C6H6
ha-ca-ca-nf   1    3.625       180.000           2.000      intrpol.bsd.on C6H6
ca-ca-ca-ne   1    3.625       180.000           2.000      intrpol.bsd.on C6H6
ca-ca-ca-nf   1    3.625       180.000           2.000      intrpol.bsd.on C6H6
X -ne-nf-X    1    3.000       180.000          -2.000      double bond
X -ne-nf-X    1    2.800         0.000           1.000      double bond

IMPROPER
ca-ca-ca-ha         1.1          180.0         2.0          General improper torsional
ca-ca-ca-ne         1.1          180.0         2.0          Using default value
ca-ca-ca-nf         1.1          180.0         2.0          Using default value

NONBON
  ha          1.4590  0.0150             Spellmeyer
  ca          1.9080  0.0860             OPLS
  ne          1.8240  0.1700             OPLS
  nf          1.8240  0.1700             OPLS
```

C.3 DPA.FRCMOD

```
remark goes here
MASS

BOND

ANGLE
ca-cg-ch   56.400     180.000   same as c1-cg-ca
cg-ch-ca   56.400     180.000   same as c1-ch-ca

DIHE
ca-ca-cg-ch   1    0.000       180.000           2.000      same as X -c1-ca-X
cg-ch-ca-ca   1    0.000       180.000           2.000      same as X -c1-ca-X

IMPROPER
ca-ca-ca-ha         1.1          180.0         2.0          General improper torsional angle (2
general atom types)
ca-ca-ca-cg         1.1          180.0         2.0          Using default value
ca-ca-ca-ch         1.1          180.0         2.0          Using default value

NONBON
```

C.4 DPCP.FRCMOD

```
remark goes here
MASS
ca 12.01         0.360               Sp2 C in pure aromatic systems
ha 1.008         0.135               H bonded to aromatic carbon
cu 12.01         0.360
c  12.01         0.360
o  16.00         0.434

BOND
ca-ha  344.3    1.087        SOURCE3  1496    0.0024    0.0045
ca-ca  478.4    1.387        SOURCE1  6228    0.0096    0.0147
cu-cu  653.7    1.346        SOURCE1    10    0.0000    0.0000    using DPCP bond length
c -cu  441.4    1.406        SOURCE2     1    0.0000    0.0000    using DPCP bond length
c -o   648.0    1.200        SOURCE1  3682    0.0134    0.0165     using DPCP bond length
ca-cu  386.7    1.456                                             interpolated from all ca-sp2C's

ANGLE
ca-ca-ha    48.5      120.01    SOURCE3 2980   0.1509   0.2511
ca-ca-ca    67.2      119.97    SOURCE3 1969   0.1024   0.3480
ca-ca-cu    67.2      119.97    SOURCE3 1969   0.1024   0.3480    (from ca-ca-ca)
ca-cu-cu    46.1      150.64    SOURCE2    3   1.8889   2.0950    (from cu-cu-ha) using DPCP bond
angle
c -cu-cu    95.0       57.18    SOURCE2    1   0.0000   0.0000     using DPCP bond angle
o -c -cu    95.0      151.41                                     DPCP angle, force from c-cu-cu
c -cu-ca    46.1      147.95                                     DPCP angle, force from cu-cu-ha
cu-c -cu    91.5       57.18                                     DPCP angle, force from cu-cx-cu

DIHE
c -cu-ca-ca    4   14.500       180.000           2.000      intrpol.bsd.on C6H6 (from X -ca-ca-X
)
c -cu-cu-ca    4   14.500       180.000           2.000      intrpol.bsd.on C6H6 (from X -ca-ca-X
)
cu-cu-ca-ha    4   14.500       180.000           2.000      intrpol.bsd.on C6H6 (from X -ca-ca-X
)
cu-ca-ca-ca    4   14.500       180.000           2.000      intrpol.bsd.on C6H6 (from X -ca-ca-X
)
ca-ca-ca-ca    4   14.500       180.000           2.000      intrpol.bsd.on C6H6 (from X -ca-ca-X
)
```

```
ha-ca-ca-ca    4   14.500       180.000           2.000      intrpol.bsd.on C6H6 (from X -ca-ca-X
)
ha-ca-ca-ha    4   14.500       180.000           2.000      intrpol.bsd.on C6H6 (from X -ca-ca-X
)
cu-cu-ca-ca    4   14.500       180.000           2.000      intrpol.bsd.on C6H6 (from X -ca-ca-X
)
ca-cu-cu-ca    4   14.500       180.000           2.000      intrpol.bsd.on C6H6 (from X -ca-ca-X
)

IMPROPER
cu-cu-c -o         10.5         180.              2.         JCC,7,(1986),230 (from X -X -c -o)
ca-cu-cu-c          8.700       180.000           2.000      intrpol.bsd.on C6H6 (from X -c -cu-X
)
ca-ca-ca-cu        14.500       180.000           2.000      intrpol.bsd.on C6H6 (from X -ca-ca-X
)

NONBON
  ca          1.9080  0.0860             OPLS
  cu          1.9080  0.0860             OPLS
  c           1.9080  0.0860             OPLS
  o           1.6612  0.2100             OPLS
```

APPENDIX D

TECHNOLOGY IN SCIENCE EDUCATION: MY EXPERIENCES

During my entire Ph.D. research, I have been fortunate enough to receive funding related to educational activities: as a teaching assistant in the Department's Instrumental Analysis lab; working on case studies for the Virtual Mass Spectrometry Laboratory website (NSF DUE-9950867); working in the Pittsburgh Public School System as an NSF-GK-12 fellow (Grant # 0338135); developing content-development workshops for statewide deployment with ASSET Inc.; and teaching a syllabus I designed for the School of Education in their "Technology in Science Education" Course. Here, I briefly lay out my current thinking about the place of technology in science education based on these experiences.

D.1 ASKING THE RIGHT QUESTION THE RIGHT WAY

In every discussion I have had with an educator (no matter the educational level they serve) I have heard strong agreement that technology should never be used just for the sake of using a technology. However, I commonly hear these same groups of educators trying to determine how they can use more technology to improve their teaching. By beginning with the premise that

they need a new technology, and that technology can add to their instructional capacities, it is all too likely that the educator will find some technology that adds some new, but minor, benefit in their classroom, that is rarely commiserate with the resources spent (time, money, and other scarce resources). If a chosen technology fails to add some specific benefit, then even if the teaching is not diminished the result is a net loss due to the investment of more time and resources (and often an expensive loss at that!)

This is certainly no condemnation of our educators – I too have fallen into the trap of being so in love with a technological idea that I missed an opportunity to ask the right question: what will this technology add to my teaching that merits the costs involved (time, money, etc.)? Will I have a return on my investment?

To this end, I have identified three broad categories where technology adds something new to the process of teaching. It is left to the educator to determine is the net cost outweighs the net gain. It is my hope that these categories will provide a starting point for the identification and critical evaluation of useful educational technologies. These categories are:

- 'Superpowers': the ability to do or perceive something that cannot be done by a normal person without some aid
- Data representation/aggregation: the ability to pull together information and display it in more intuitive to understand forms
- Scaffolding understanding: the use of technology to help guide the construction of a new thinking model in the student

These broad categories are based directly on my experiences communicating science to learners running the gamut of age brackets (kindergarten through established and practicing teachers). To be certain, there is carryover between these categories, and many others may exist.

This topic could (and has!) filled entire books; this chapter is intended to serve as a brief distillation of my experiences, and as a starting point for the reader to utilize these three categories to help inform their evaluation of educational technologies. Various topics are mentioned in-line with the explanations of these categories.

D.2 SUPERPOWERS – THE ABILITY TO PERSONALLY DO SOMETHING NEW

This is probably the most broad of the categories I have identified, and is best explained by a variety of subcategories.

D.2.1 Perception of Scales Large and Small

As a chemist, I commonly use instrumentation to perceive objects and phenomena at scales too small to be seen with the naked eye. Sometimes, these take the form of a direct measurement or observation (*e.g.* the use of a microscope to see small features), but oftentimes these may be representations of something too small to be seen (in chemistry, 3D models of molecular orbitals, or in biology, representations of the shapes of biomolecules and how they interact). The microscale is the more obvious application of these perceptive technologies, but the macroscale is often just as hard to understand without a technology. Physical representations can often communicate the broad strokes of these ideas (e.g. moving a globe around a darkened classroom with a lamp at the center), while digital forms provide the ability to see the entire system while still zooming into the finer details, and maintaining the rigorous rules of the model.

Technology is typically thought of today as involving computers, but it is important to think about both high- and low-tech approaches to our teaching. Low tech approaches (a traditional microscope) should be weighed carefully against high-tech approaches (digital camera microscopes with real-time video feeds) to see what gain is actually desired. If the intent is to give the students direct control over the observation, a low-tech approach may be more financially tractable. However, if the ability to compare and contrast the development of a cell culture over time is desired, the high-tech approach may be better suited by providing the ability to look back-and-forth in time (hence, the whimsical name of this category, superpowers!) In a biology class, a balance between the two is certainly desirable, and the lesson plans and 'shopping lists' should reflect this.

Likewise, the perception of large scales can be aided by a number of commercial and freeware packages. The free software packages (e.g. Celestia, Google Earth, Stellarium), rather than the cost of the microscopes being a limiting factor, the time required to 'learn the tool' becomes the true impediment, both for the educator and the student.[127] While these free packages are often quite high-quality, the breadth of features often results in a tool which is 'unready to hand'.

When animations are used to explain a topic, Richard Mayer of UCSB has identified five characteristics of effective animations and presentations: [128]

Prune extraneous words and pictures.

Include on-screen organizational cues or signals to help direct learners attention.

Synchronize narration so that students hear and see words simultaneously.

Use spoken narration in a conversational, rather than formal, style.

Place text levels close to the image they are intended to describe.

D.2.2 Separation of the (Humanly) Imperceptible

Many times in science, it is useful to separate physical phenomena from one another in a way that is impossible for most (or all) people. Some examples would be the rigorous determination of what a color is and how bright/dark the color is, separation of two or more frequencies from a sound, observation of a change in a vector over time, and the ability to separate small time slices to better observe and measure velocities and accelerations.

Oftentimes, technologies that fall in this category serve as measurement tools, such as a spectrometer (measuring the intensity of different colors), microphones and frequency analyzers, tools like radar guns that allow us to observe a phenomenon while 'overlaying' numerical data in real-time, and video capture and frame analysis hardware/software.

Though these sorts of measurement devices have been available for some time now, analogs of expensive scientific tools are now available with a combination of free software and consumer electronics in ways (and prices) which have never been seen before. For example, consider motion capture and analysis. The popular line of PowerShot point-and-shoot digital cameras are available for approximately $150 USD (in November of 2008). Various programmers have contributed to an effort that has resulted in software that can be loaded on these cameras (in a temporary and non-destructive fashion) that allows many PowerShot models to acquire stop-motion photographs at shutter speeds of 1/10,000" and flash-sync speeds of 1/64,000 second. The technical knowledge required to utilize this software is not trivial, but certainly not out of the skill set for most interested parties.[129] Motion analysis (for example, the determination of gravitational acceleration from a video file) can also be performed by freely available software, without the purchase of new hardware (for example, the PhysMo program).[130]

D.3 DATA REPRESENTATION AND AGGREGATION

The visualization of complex data sets is an actively developing topic that is of interest to every field. The ability to recognize trends in data has become a true cornerstone of modern science, and even before students understand the numerical methods involved, many have used visualization tools to represent data (e.g. the least-squares trendline in Microsoft Excel). Technology provides opportunities to include better data representations more often in our teaching.

By preparing a graphing template in a spreadsheet program (and again, many free software suites exist in this domain) I have had students as young as 2nd graders communicate their measurements to me during in-class laboratories, and they have been able to observe their data graphically and make predictions about the next test they will conduct based on this graph. Real-time graphic views of data may strongly reinforce in students the cyclic nature of the scientific method, as they start from a hypothesis, conduct a test to yield data, and revise their hypothesis based on the data they collect, without the sometimes considerable time delay between collection and visualization (especially when visualization is done via pen, paper, and graph paper).[131]

More subtle and connective visualizations are certainly possible, and while they can be transformational in the way a topic is viewed, these may involve considerable creation time, and oftentimes these visualizations may only match the time involved when they are pre-made by an expert and displayed by the educator. A chemical example of this is the shape of atomic, hybridized, and molecular orbitals; it is the rare educator who has the time or inclination to implement these equations in order to show them in 3D. Thanks to the internet, it takes only one of these rare individuals to save other educators from creating the technology, requiring instead

only that they can identify and implement them. Many excellent websites include a number of views of orbitals (the Orbitron is among my favorites [132]).

These technologies truly shine when aggregating and displaying multivariate data in a new and explanatory fashion. An excellent example is evident in a talk given by Hans Rosling of the Karolinska Institutet to the Technology, Entertainment, and Design Conference in 2006 (viewable at [133]); the software used in this talk is named GapMinder (available online at [134]). This software shows highly-multivariate data (e.g. country population, gross national product, infant mortality, region of the world, and time simultaneously via animation).

D.4 SCAFFOLDING UNDERSTANDING

Technology can be used to help scaffold a topic for a learner. This can be important both in the planning and communication of a lesson. One of the great difficulties in teaching is to develop an interconnected view of a topic, and identify what topics should be included and when, so that the student can build a similarly interconnected view of the subject. A low-tech approach to this has been utilized to good effect in my work with ASSET Inc. during our content deepening workshops for practicing teachers. Here, we have had the teachers distill the entire unit to the largest and most powerful learning goals (including "Big Ideas", which can briefly be thought of as concepts which are portable between the individual disciplines of science; for a more nuanced and powerful view, refer to the work of Jen Cartier, of the University of Pittsburgh School of Education). These Big Ideas and learning goals were placed on adhesive papers, and moved around until a sort concept map had developed. A more high-tech version of this approach can be performed via mind-mapping software (my preferred freeware implementation

is FreeMind [135]). While a low-tech implementation is certainly sufficient, there is little barrier-to-entry in learning the concept-mapping software, and this illustrates another advantage of technology that applies to the other discussed examples; digital files are easy to store, edit, and share, and are far more compact and maintainable that many hardcopy-approaches. These concept maps can also be useful in showing a student how to better study and integrate topics. I have recently used a FreeMind example to demonstrate to a student what connections between topics are important to identify on their own, and the student has indicated that they will try a similar approach to move beyond a purely flash-card based studying approach (and the typically discretized view of the topic that it commonly leads to.)

D.5 SUMMARY

If a technology provides more educational advantage than the resources it demands, it may be worth implementing in the classroom (or in the office while planning for the classroom.) A technology has a stronger likelihood of being useful if it gives a new observational ability, if it helps pull together and communicate a wide range of data, and if if can help guide the lesson and learner into a more holistic view of a topic. When identifying technologies to accomplish these goals, it is important to consider both high- and low-tech approaches; when a high-tech version is useful, we can best manage our limited resources keeping in mind the myriad free options becoming available, and by developing partnerships with those who might be aware of emerging technologies (e.g. camera firmware that provides high-end features on cameras one is likely to own/be willing to purchase).

BIBLIOGRAPHY

[1] T. J. Burkey, J. Am. Chem. Soc., 112 (1990) 8329-8333.
[2] T. Ni, R. A. Caldwell and L. A. Melton, J. Am. Chem. Soc., 111 (1989) 457-464.
[3] M. S. Herman and J. L. Goodman, J. Am. Chem. Soc., 111 (1989) 9105-9107.
[4] M. Bernstein, J. D. Simon and K. S. Peters, Chem. Phys. Lett., 100 (1983) 241-244.
[5] J. J. Grabowski, J. D. Simon and K. S. Peters, J. Am. Chem. Soc., 106 (1984) 4615-4616.
[6] J. C. Scaiano, C. Chen and P. F. McGarry, J. Photochem. Photobiol., A, 62 (1991) 75-81.
[7] R. W. Larsen, Inorg. Chim. Acta, 288 (1999) 74-81.
[8] K. B. Clark, D. D. M. Wayner, S. H. Demirdji and T. H. Koch, J. Am. Chem. Soc., 115 (1993) 2447-2453.
[9] L. J. Rothberg, J. D. Simon, M. Bernstein and K. S. Peters, J. Am. Chem. Soc., 105 (1983) 3464-3468.
[10] L. G. Arnaut, R. A. Caldwell, J. E. Elbert and L. A. Melton, Rev. Sci. Instrum., 63 (1992) 5381-5389.
[11] R. R. Hung and J. J. Grabowski, J. Am. Chem. Soc., 121 (1999) 1359-1364.
[12] S. Nonell, P. F. Aramendia, K. Heihoff, R. M. Negri and S. E. Braslavsky, J. Phys. Chem., 94 (1990) 5879-5883.
[13] R. P. Herbrich and R. Schmidt, J. Photochem. Photobiol., A, 133 (2000) 149-158.
[14] J. E. Rudzki, J. L. Goodman and K. S. Peters, J. Am. Chem. Soc., 107 (1985) 7849-7854.
[15] R. R. Hung and J. J. Grabowski, J. Phys. Chem., 95 (1991) 6073-6075.
[16] R. Dunsbach and R. Schmidt, J. Photochem. Photobiol., A, 83 (1994) 7-13.
[17] K. S. Peters, T. Watson and T. Logan, J. Am. Chem. Soc., 114 (1992) 4276-4278.
[18] J. A. Westrick, J. L. Goodman and K. S. Peters, Biochemistry, 26 (1987) 8313-8318.
[19] W. P. Leung, K. C. Cho, S. K. Chau and C. L. Choy, Chem. Phys. Lett., 141 (1987) 220-224.
[20] K. Marr and K. S. Peters, Biochemistry, 30 (1991) 1254-1258.
[21] J. A. Daffron, G. J. Farrell and T. J. Burkey, Rev. Sci. Instrum., 71 (2000) 3882-3885.
[22] R. R. Hung and J. J. Grabowski, J. Am. Chem. Soc., 114 (1992) 351-353.
[23] J. Morais, Ma, Jangseok, and Zimmt, Matthew B., J. Phys. Chem., 95 (1991) 3885-3888.
[24] C. K. N. Tam and A. C. Patel, Rev. Mod. Phys., 53 (1981) 517-553.
[25] R. R. Hung, Ph.D. Thesis, Harvard University, Cambridge, Mass., (1993)
[26] J. A. Cabeza, I. da Silva, I. del Rio, L. Martinez-Mendez, D. Miguel and V. Riera, Angew. Chem., Int. Ed., 43 (2004) 3464-3467.
[27] I. L. Franklin, A. M. Beale and G. Sankar, Catal. Today, 81 (2003) 623-629.
[28] B. L. Tjelta and P. B. Armentrout, J. Am. Chem. Soc., 118 (1996) 9652-9660.
[29] M. D. Cavanaugh, B. T. Gregg and A. R. Cutler, Organometallics, 15 (1996) 2764-2769.
[30] F. A. Cotton, Inorg. Chem., 41 (2002) 643-658.

[31] R. H. Crabtree, J. Organomet. Chem., 689 (2004) 4083-4091.
[32] K. G. Caulton, Coord. Chem. Rev., 38 (1981) 1-43.
[33] S. Hu, G. J. Farrell, C. Cook, R. Johnston and T. J. Burkey, Organometallics, 13 (1994) 4127-4128.
[34] P. F. Yang and G. K. Yang, J. Am. Chem. Soc., 114 (1992) 6937-6938.
[35] D. M. Hester, J. Sun, A. W. Harper and G. K. Yang, J. Am. Chem. Soc., 114 (1992) 5234-5240.
[36] A. A. Sorensen and G. K. Yang, J. Am. Chem. Soc., 113 (1991) 7061-7063.
[37] J. K. Klassen, Selke, Matthais, Sorensen, Amy A., Yang, Gilbert K., J. Am. Chem. Soc., 112 (1990) 1267-1268.
[38] G. I. Childs, D. C. Grills, X. Z. Sun and M. W. George, Pure Appl. Chem., 73 (2001) 443-447.
[39] P. J. Giordano, Wrighton, Mark S., Inorg. Chem., 16 (1977) 160-166.
[40] J. Full, C. Daniel and L. Gonzalez, Phys. Chem. Chem. Phys., 5 (2003) 87-96.
[41] P. T. Snee, C. K. Payne, K. T. Kotz, H. Yang and C. B. Harris, J. Am. Chem. Soc., 123 (2001) 2255-2264.
[42] T. Jiao, Z. Pang, T. J. Burkey, R. F. Johnston, T. A. Heimer, V. D. Kleiman and E. J. Heilweil, J. Am. Chem. Soc., 121 (1999) 4618-4624.
[43] J. A. Lavilla and J. L. Goodman, Chem. Phys. Lett., 141 (1987) 149-153.
[44] J. K. Klassen and G. K. Yang, Organometallics, 9 (1990) 874-876.
[45] B. Fletcher and J. J. Grabowski, J. Chem. Educ., 77 (2000) 640-645.
[46] G. L. Geoffroy and M. S. Wrighton, Organometallic Photochemistry, Academic, New York, (1979).
[47] S. E. Braslavsky and G. E. Heibel, Chem. Rev. (Washington, DC, U. S.), 92 (1992) 1381-1410.
[48] W. J. Leigh and D. R. Arnold, Can. J. Chem., 59 (1981) 3061-3075.
[49] C. G. Hatchard, Parker, C. A., Proc. Roy. Soc., A235 (1956) 518-536.
[50] A. D. Kirk and C. Namasivayam, Anal. Chem., 55 (1983) 2428-2429.
[51] H. J. Kuhn, S. E. Braslavsky and R. Schmidt, Pure Appl. Chem., 76 (2004) 2105-2146.
[52] K. S. Peters, Pure Appl. Chem., 58 (1986) 1263-1266.
[53] T. J. Burkey, Majewski, M., Griller, D., J. Am. Chem. Soc., 108 (1986) 2218-2221.
[54] K. S. Peters, Snyder, G. J., Science, 241 (1988) 1053-1057.
[55] J. M. Kanabus-Kaminska, B. C. Gilbert and D. Griller, J. Am. Chem. Soc., 111 (1989) 3311-3314.
[56] J. M. Morse, Jr., G. H. Parker and T. J. Burkey, Organometallics, 8 (1989) 2471-2474.
[57] T. J. Burkey, Polyhedron, 8 (1989) 2681-2687.
[58] M. S. Herman and J. L. Goodman, J. Am. Chem. Soc., 110 (1988) 2681-2683.
[59] M. S. Herman and J. L. Goodman, J. Am. Chem. Soc., 111 (1989) 1849-1854.
[60] D. Griller, J. A. Martinho Simoes, P. Mulder, B. A. Sim and D. D. M. Wayner, J. Am. Chem. Soc., 111 (1989) 7872-7876.
[61] Z. Pang, T. J. Burkey and R. F. Johnston, Organometallics, 16 (1997) 120-123.
[62] T. A. Moore, D. Benin and R. Tom, J. Am. Chem. Soc., 104 (1982) 7356-7357.
[63] J. A. B. Riddick, W. B.; Sakano, T. K., Organic Solvents: Physical Properties and Methods of Purification, 4th Ed., Wiley and Sons, New York, (1986).
[64] W. Brostrow, Phys. And Chem. Of Liquids, 3 (1972) 91-113.

[65] TRC Thermochemical Tables, Vol. I, II., Thermodynamics Research Center, College Station, TX, (1986).
[66] C. E. Brown, Y. Ishikawa, P. A. Hackett and D. M. Rayner, J. Am. Chem. Soc., 112 (1990) 2530-2536.
[67] J. R. Chipperfield, J. C. R. Sneyd and D. E. Webster, J. Organomet. Chem., 178 (1979) 177-189.
[68] Y. Li, B. Sztaray and T. Baer, J. Am. Chem. Soc., 123 (2001) 9388-9396.
[69] H.-J. Fan and M. B. Hall, Organometallics, 20 (2001) 5724-5730.
[70] L. S. Sunderlin and R. R. Squires, Int. J. Mass Spectrom., 182/183 (1999) 149-161.
[71] G. Pajaro, F. Calderazzo and R. Ercoli, Gazz. Chim. Ital., 90 (1960) 1486-1494.
[72] K. E. Lewis, D. M. Golden and G. P. Smith, J. Am. Chem. Soc., 106 (1984) 3905-3912.
[73] T. R. Fletcher and R. N. Rosenfeld, J. Am. Chem. Soc., 110 (1988) 2097-2101.
[74] Y. J. Chen, C. L. Liao and C. Y. Ng, J. Chem. Phys., 107 (1997) 4527-4536.
[75] P. R. Das, T. Nishimura and G. G. Meisels, J. Phys. Chem., 89 (1985) 2808-2812.
[76] S. Gittermann, T. Jiao and T. J. Burkey, Photochem. Photobiol. Sci., 2 (2003) 817-820.
[77] G. J. Farrell and T. J. Burkey, J. Photochem. Photobiol., A, 137 (2000) 135-139.
[78] T. Jiao, G.-L. Leu, G. J. Farrell and T. J. Burkey, J. Am. Chem. Soc., 123 (2001) 4960-4965.
[79] J. Berkowitz, G. B. Ellison and D. Gutman, J. Phys. Chem., 98 (1994) 2744-2765.
[80] K. S. Peters, T. Watson and K. Marr, Annual Review of Biophysics and Biophysical Chemistry, 20 (1991) 343-362.
[81] S. E. Braslavsky, R. M. Ellul, R. G. Weiss, H. Al-Ekabi and K. Schaffner, Tetrahedron, 39 (1983) 1909-1913.
[82] T. Gensch and S. E. Braslavsky, J. Phys. Chem. B, 101 (1997) 101-108.
[83] W. Fuss, S. A. Trushin and W. E. Schmid, Res. Chem. Intermed., 27 (2001) 447-457.
[84] G. K. Yang, K. S. Peters and V. Vaida, Chem. Phys. Lett., 125 (1986) 566-568.
[85] S.-Y. Hou, I. Hetherington, W. M., G. M. Korenowski and K. B. Eisenthal, Chem. Phys. Lett., 68 (1979) 282-284.
[86] D. Griller, Wayner, D. M., Pure Appl. Chem., 61 (1989) 717-724.
[87] J. Nasielski and A. Colas, Inorg. Chem., 17 (1978) 237-240.
[88] J. K. Kochi, Free radicals, Wiley, New York, (1973).
[89] D. Booth and R. M. Noyes, J. Am. Chem. Soc., 82 (1960) 1868-1872.
[90] S. Wieland and R. Van Eldik, J. Phys. Chem., 94 (1990) 5865-5870.
[91] S. Wieland and R. Van Eldik, Coord. Chem. Rev., 97 (1990) 155-165.
[92] S. K. Nayak and T. J. Burkey, Organometallics, 10 (1991) 3745-3750.
[93] J. Nasielski and A. Colas, J. Organomet. Chem., 101 (1975) 215-219.
[94] H. R. Kiefer and T. G. Traylor, J. Am. Chem. Soc., 89 (1967) 6667-6671.
[95] D. D. M. Wayner, E. Lusztyk, D. Page, K. U. Ingold, P. Mulder, L. J. J. Laarhoven and H. S. Aldrich, J. Am. Chem. Soc., 117 (1995) 8737-8744.
[96] G. Wypych, Knovel solvents: a properties database, ChemTec Pub., Toronto ;; New York, (2000).
[97] TRC Thermodynamic Tables; Vol. I, II, Thermodynamics Research Center: College Station, TX, (1986)
[98] K. W. Davies, D. Maivald and J. J. Grabowski, J. Photochem. Photobiol., A, 197 (2008) 335-341.

[99] J. A. M. Simões, NIST Chemistry WebBook, NIST Standard Reference Database Number 69, (2005)
[100] E. F. Walsh, V. K. Popov, M. W. George and M. Poliakoff, J. Phys. Chem., 99 (1995) 12016-12020.
[101] F. A. Cotton and A. G. Stanislowski, J. Am. Chem. Soc., 96 (1974) 5074-5082.
[102] R. D. Closson, J. Kozikowski and T. H. Coffield, J. Org. Chem., 22 (1957) 598.
[103] S. M. Massick, V. Mertens, J. Marhenke and P. C. Ford, Inorg. Chem., 41 (2002) 3553-3559.
[104] A. Derecskei-Kovacs and D. S. Marynick, J. Am. Chem. Soc., 122 (2000) 2078-2086.
[105] W. Boese, K. McFarlane, B. Lee, J. Rabor and P. C. Ford, Coord. Chem. Rev., 159 (1997) 135-151.
[106] W. T. Boese and P. C. Ford, J. Am. Chem. Soc., 117 (1995) 8381-8391.
[107] W. T. Boese and P. C. Ford, Organometallics, 13 (1994) 3525-3531.
[108] W. T. Boese, B. Lee, D. W. Ryba, S. T. Belt and P. C. Ford, Organometallics, 12 (1993) 4739-4741.
[109] M. Akita, O. Mitani, M. Sayama and Y. Morooka, Organometallics, 10 (1991) 1394-1399.
[110] P. L. Motz, D. J. Sheeran and M. Orchin, J. Organomet. Chem., 383 (1990) 201-212.
[111] D. J. Sheeran, J. D. Arenivar and M. Orchin, J. Organomet. Chem., 316 (1986) 139-146.
[112] P. DeShong and G. A. Slough, Organometallics, 3 (1984) 636-638.
[113] S. B. Butts, S. H. Strauss, E. M. Holt, R. E. Stimson, N. W. Alcock and D. F. Shriver, J. Am. Chem. Soc., 102 (1980) 5093-5100.
[114] J. A. Gladysz, G. M. Williams, W. Tam, D. L. Johnson, D. W. Parker and J. C. Selover, Inorg. Chem., 18 (1979) 553-558.
[115] B. E. Douglas, Inorganic syntheses. Volume 18, McGraw Hill, New York, (1978).
[116] C. Ridley, A. C. Stern, T. Green, R. DeVane, B. Space, J. Miksosvska and R. W. Larsen, Chem. Phys. Lett., 418 (2006) 137-141.
[117] K. Takeshita, N. Hirota and M. Terazima, J. Photochem. Photobiol., A, 134 (2000) 103-109.
[118] M. Terazima, T. Hara and N. Hirota, Chem. Phys. Lett., 246 (1995) 577-582.
[119] R. Schmidt and M. Schuetz, Chem. Phys. Lett., 263 (1996) 795-802.
[120] R. DeVane, C. Ridley, R. W. Larsen, B. Space, P. B. Moore and S. I. Chan, Biophys. J., 85 (2003) 2801-2807.
[121] P. C. Chen and Y. C. Chieh, J. Mol. Struct.-Theochem, 624 (2003) 191-200.
[122] A. Poloukhtine and V. V. Popik, J. Phys. Chem. A, 110 (2006) 1749-1757.
[123] M. J. Frisch, G. W. Trucks, H. B. Schlegel, G. E. Scuseria, M. A. Robb, J. R. Cheeseman, J. J. A. Montgomery, T. Vreven, K. N. Kudin, J. C. Burant, J. M. Millam, S. S. Iyengar, J. Tomasi, V. Barone, B. Mennucci, M. Cossi, G. Scalmani, N. Rega, G. A. Petersson, H. Nakatsuji, M. Hada, M. Ehara, K. Toyota, R. Fukuda, J. Hasegawa, M. Ishida, T. Nakajima, Y. Honda, O. Kitao, H. Nakai, M. Klene, X. Li, J. E. Knox, H. P. Hratchian, J. B. Cross, C. Adamo, J. Jaramillo, R. Gomperts, R. E. Stratmann, O. Yazyev, A. J. Austin, R. Cammi, C. Pomelli, J. W. Ochterski, P. Y. Ayala, K. Morokuma, G. A. Voth, P. Salvador, J. J. Dannenberg, V. G. Zakrzewski, S. Dapprich, A. D. Daniels, M. C. Strain, O. Farkas, D. K. Malick, A. D. Rabuck, K. Raghavachari, J. B. Foresman, J. V. Ortiz, Q. Cui, A. G. Baboul, S. Clifford, J. Cioslowski, B. B. Stefanov, G. Liu, A. Liashenko, P. Piskorz, I. Komaromi, R. L. Martin, D. J. Fox, T. Keith, M. A. Al-Laham, C. Y. Peng, A.

Nanayakkara, M. Challacombe, P. M. W. Gill, B. Johnson, W. Chen, M. W. Wong, C. Gonzalez and J. A. Pople, Gaussian 03, Revision B.05, Gaussian, Inc., Pittsburgh, PA, (2003).
[124] D. A. Case, T. A. Darden, I. T.E. Cheatham, C. L. Simmerling, J. Wang, R. E. Duke, R. Luo, K. M. Merz, D. A. Pearlman, M. Crowley, R. C. Walker, W. Zhang, B. Wang, S. Hayik, A. Roitberg, G. Seabra, K. F. Wong, F. Paesani, X. Wu, S. Brozell, V. Tsui, H. Gohlke, L. Yang, C. Tan, J. Mongan, V. Hornak, G. Cui, P. Beroza, D. H. Mathews, C. Schafmeister, W. S. Ross and P. A. Kollman, AMBER 9, University of California, San Francisco, (2006).
[125] R. Friedberg and J. E. Cameron, J. Chem. Phys., 52 (1970) 6049-6058.
[126] M. P. Allen and D. J. Tildesley, Computer Simulation of Liquids, Clarendon Press, Oxford, (1987).
[127] C. W. G. S. Wolff-Michael Roth, Journal of Research in Science Teaching, 33 (1996) 995-1017.
[128] D. Viadero, Education Weekly, 12-13.
[129] The CHDK Wiki, http://chdk.wikia.com/wiki/CHDK, also archived at http://web.archive.org/web/*/http://chdk.wikia.com/wiki/CHDK, November 16, 2008
[130] PhysMo - Video Motion Analysis, http://physmo.sourceforge.net/, November 16, 2008
[131] M. Murin, GIREP Conference, (2006)
[132] M. Winter, The Oribtron: A Gallery of Atomic and Molecular Orbitals on the WWW, http://winter.group.shef.ac.uk/orbitron/, November 16, 2008
[133] H. Rosling, http://www.ted.com/index.php/talks/hans_rosling_shows_the_best_stats_you_ve_ever_seen.html, November 16, 2008
[134] Gapminder, http://www.gapminder.org/, November 16, 2008
[135] FreeMind, http://freemind.sourceforge.net/, November 16, 2008